

A High-Performance Magnesium Lattice Clock: Stability and Accuracy Analysis

Von der Fakultät für Mathematik und Physik der
Gottfried Wilhelm Leibniz Universität Hannover

zur Erlangung des Grades

Doktor der Naturwissenschaften
- Dr. rer. nat. -

genehmigte Dissertation von

Nandan Jha, M.Sc.

2022

Referent:

Prof. Dr. Ernst M. Rasel
Leibniz Universität Hannover
Institut für Quantenoptik

Korreferent:

Prof. Dr. Wolfgang Ertmer
Leibniz Universität Hannover
Institut für Quantenoptik

Korreferent:

Prof. Dr. Kurt Gibble
Penn State University
Department of Physics

Vorsitzender der Prüfungskommission:

Prof. Dr. Klemens Hammerer
Leibniz Universität Hannover
Institut für Theoretische Physik

Tag der Disputation: 10. Februar 2022

Abstract

Optical lattice clocks have reached uncertainties in 10^{-18} regime, well surpassing the primary microwave frequency standard. Such performance levels have allowed for applications from geodesy to fundamental physics. The performance of state of the art optical lattice clocks are strongly influenced by black body radiation (BBR) induced frequency shifts. Magnesium is one of the optical lattice clock candidate elements with very low sensitivity to BBR, which makes it an interesting candidate as an optical frequency reference.

Optical lattice clocks rely on high-Q optical transitions, where Doppler and recoil shifts are suppressed by trapping the atoms in Lamb-Dicke regime. For Magnesium, due to its low atomic mass, the tunneling induced line-broadening is significantly large. This has been a bottleneck in reducing the instability of Magnesium lattice clock. However the large tunneling rate for Magnesium atoms in the optical lattice also allows us to study these lattice effects using optical spectroscopy.

Lattice AC Stark shift is one of the important contributions to the uncertainty budget for an optical lattice clock. To achieve clock uncertainties in 10^{-18} regime, even the contributions from multipolar polarizabilities and hyperpolarizability becomes significant. Therefore, operational magic frequencies have been identified in Strontium and Ytterbium lattice clocks, where the light shift dependence on intensity is zero to the lowest order.

In this thesis, an extensive model has been developed to understand the influence of tunneling in a one dimensional optical lattice on the clock transition lineshape. This model is used to simulate the spectroscopy results previously observed in our experiment, which show strong lineshape asymmetry as lattice wavelength is detuned from the magic condition. The strong influence of transverse states in generating these asymmetries was highlighted by numerical simulations.

To improve the performance of our Magnesium lattice clock from the last frequency measurements, lattice system upgrades were carried out within the scope of this thesis. This allowed to suppress the tunneling induced line-broadening to sub-Hz regime for the first time for magnesium, and to resolve the $^1S_0 - ^3P_0$ clock transition with a linewidth of 7(3) Hz. The high line-Q thus obtained of $9(3) \times 10^{13}$ helped reduce the clock instability in self-comparison measurement to $7.2_{-1.8}^{+7.7} \times 10^{-17}$ in 3000 seconds of averaging time.

The improved clock instability also helped estimate various systematic shifts with much improved uncertainties. The probe AC Stark shift and Zeeman shift uncertainties were reduced to the mid- 10^{-17} regime, while cold collision shift was characterized with uncertainty of 1.4×10^{-16} . With an aim to similarly reduce lattice AC Stark shift uncertainty, influence of higher order shifts was characterized for Magnesium for the first time. The hyperpolarizability coefficient was estimated to be $197(53) \mu\text{Hz}/(\text{kWcm}^{-2})^2$. These measurements show that the lattice shift can be characterized with an uncertainty of 6.5×10^{-16} , paving way for a future frequency measurement with more than an order of magnitude lower uncertainty.

Keywords: Optical frequency standard, precision spectroscopy, lattice clock

CONTENTS

1	Introduction	3
1.1	A brief history of Optical clocks	4
1.2	Motivation for a magnesium lattice clock	9
2	A Magnesium lattice clock	13
2.1	Atomic structure of Magnesium	13
2.2	Doppler- and recoil-free spectroscopy	15
2.3	What about the lattice AC Stark shift?	24
2.4	Spectroscopy of a forbidden transition	26
2.5	A laser to probe the clock transition	28
2.6	Measuring optical frequencies	35
2.7	Optical trapping and manipulation of ^{24}Mg	36
2.7.1	Laser systems used for trapping the atoms	38
2.7.2	Vacuum chamber and Magnetic fields setup	41
3	Characterizing line-broadening in an optical lattice	45
3.1	Not so deep in the Lamb-Dicke regime	45
3.2	Line-broadening mechanisms in a deep optical lattice	55
4	Magnesium lattice clock instability in 10^{-17} regime	59
4.1	Spectroscopy in Hz regime	60
4.1.1	Lattice power upgrade	60
4.1.2	Suppression of probe laser inhomogeneity	63
4.2	Frequency instability characterization	68
5	Systematic shifts affecting the clock	73
5.1	Probe AC Stark shift	74
5.2	Quadratic Zeeman shift	76
5.3	Collision shift	78
5.4	Lattice AC Stark shift	79
5.5	Summary	85

6 Outlook	87
6.1 Cooling on the intercombination transition	87
6.2 Suppressing tunneling induced broadening	90
6.3 Enhancing the clock duty cycle	94
Bibliography	119
List of Figures	123
List of Tables	125
List of Publications	128
Acknowledgments	131

Introduction

Accurate timekeeping has progressively become more important for human civilization, and while celestial bodies were used to define SI second till 1967, development of atomic clocks led to a re-definition of SI second based on a hyperfine atomic transition of Cesium-133. There were many steps in between these extremes of technologies. Egyptian Sun dials, Greek water clocks, Chinese candle clocks, medieval mechanical clocks and modern quartz clocks are all by themselves fascinating stories of rich science and history. However, with atomic clocks, for the first time absolute frequency references could be realized in laboratories around the world leading to tremendous advancements in accurate timekeeping and the applications dependent on them. Precise atomic clocks have since become extremely important in applications such as Global Navigation Satellite Systems (GNSS) and Very Long Baseline Interferometry (VLBI). Atomic clocks have also developed over the years from microwave atomic clocks to optical atomic clocks, which forms the topic of this thesis. As shown in Fig. 1.1, in the general scheme of an optical clock, a stable oscillator is referenced to an atomic transition using high precision spectroscopy techniques. However, the ultrahigh line-Q of optical clock transitions necessitates pre-stabilization of the probe laser (oscillator) to a macroscopic frequency reference. Optical spectroscopy of these atomic transitions is then used to generate the error signal with which the probe laser is steered to the resonance. The accurate timing signal is then generated from the stabilized laser using an optical frequency comb. Before going into the technical details of these systems, in the next section, it is worthwhile to look at the interesting history of the field to see how each of the individual subsystems in Fig. 1.1 developed to allow the optical clock performances to reach the 10^{-18} regime.

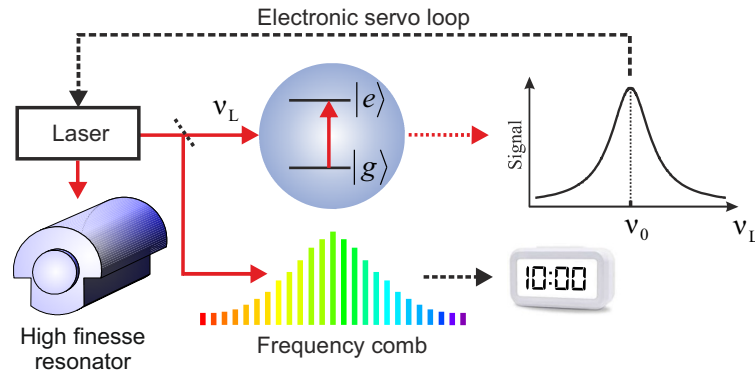


Figure 1.1: Schematic of optical atomic clocks.

1.1 A brief history of Optical clocks

After decades of sustained development, atomic clocks were realized for the first time in 1955 [1]. This first atomic clock developed by Louis Essen was based on spectroscopy of the hyperfine transition of ^{133}Cs , which was eventually chosen as the SI definition for second in 1967 [2]. It is indeed very interesting to note the dramatic improvement in accuracy of atomic clocks since their first realization. During this time, atomic clocks have already contributed to numerous every day applications as well as advancement of fundamental science [3]. By the end of last century, researchers had started to push towards the next big upgrade in the clock technology: moving from microwave atomic frequency standards to optical standards. The first optical frequency measurement was performed using a complex microwave-optical frequency chain [4]. About the same time, ideas for an octave spanning frequency comb were coming together as well, leading eventually to the first measurements of the carrier-envelope-offset (CEO) frequency of mode-locked lasers by the f - $2f$ interference measurements [5, 6]. This was a milestone moment for optical clocks, since it bridged the gap between microwave clocks and optical clocks with a table top apparatus. Very soon this discovery earned Theodor Hänsch and John Hall the Nobel Prize in 2005. The remarkable history behind the frequency comb development is very well detailed in the Nobel lectures of John Hall and Theodor Hänsch [7, 8]. As can be seen in the Fig. 1.2 depicting clock uncertainties over the time, there has been a remarkable improvement in the optical clock performance since the first demonstrations of femtosecond laser frequency comb mediated frequency comparisons.

Optical clocks offer clear advantages over microwave clocks owing to their many orders of magnitude higher frequency, which leads to orders of magnitude larger

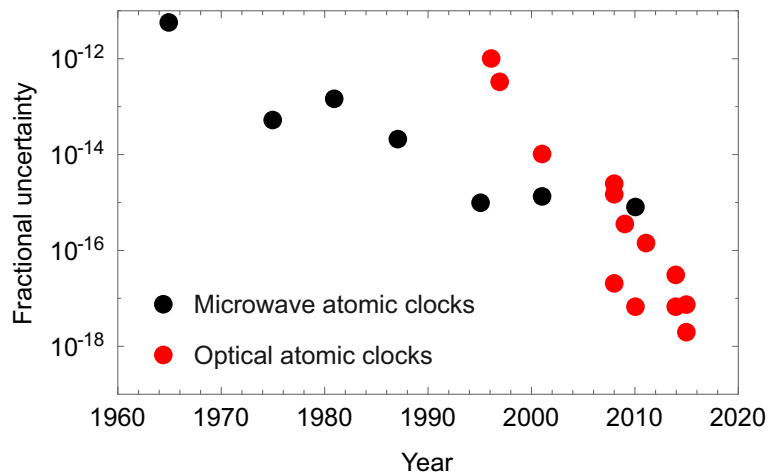


Figure 1.2: Uncertainty of microwave and optical atomic clocks over the years is shown here. A rapid improvement in the performance of optical clocks over last two decades can be seen.

line-Q. The instability of an atomic frequency standard is given as

$$\sigma_{\frac{\delta\nu}{\nu_0}}(\tau) \sim \frac{\Delta\nu}{\nu_0} \frac{1}{S/N} \sqrt{\frac{T_c}{\tau}}, \quad (1.1)$$

where ν_0 is the atomic transition frequency, $\Delta\nu$ is the spectroscopy linewidth, T_c is the clock cycle time, and S/N is the signal to noise ratio of the spectroscopy measurement. Therefore, a larger clock frequency ν_0 dramatically improves the clock precision and makes it possible to reduce clock instabilities down to the 10^{-18} regime. However, one big hurdle in reaching these performances was the Doppler and recoil shift associated with optical spectroscopy of cold atomic samples. Sub-Doppler spectroscopy techniques [9, 10] were limited in both precision and accuracy to about 10^{-14} levels. However developments in the field of ion trapping and ultracold atom trapping made it possible to perform Doppler and recoil free spectroscopy in the Lamb-Dicke regime [11]. Ions trapped in electromagnetic traps were the natural first choice for development of optical clocks due to their clean unperturbed environments and technological readiness. Already in the first decade of this century, ion clocks had demonstrated accuracy in the 10^{-17} regime [12], and seemed well positioned for reaching many more milestones in the years to come.

While ion clocks were being developed all over the world, performance of neutral atom optical clocks were limited due to the large frequency shifts associated with trapping light fields. The great interest in neutral atom clocks was essentially motivated by the possibility of using a large number of atoms for clock spectroscopy. Even though there has been significant work on multi-ion clocks since the initial days [13, 14], there are still considerable obstacles in scaling the number of trapped ions in an ion-clock. Limited for now to single ion operation, ion clocks suffer from

quantum projection noise (QPN) [15], which significantly limits their stability. Neutral atoms with much weaker long range interactions have a major advantage over ion clocks since the instability would scale as $1/\sqrt{N}$, where N is the total atom number in the trap. However the best possible way of confining neutral atoms in Lamb-Dicke regime would involve trapping them in an optical lattice, which by design necessitates large AC Stark shifts. This was for a long time a major obstacle in development of optical lattice clocks. However, following the proposal of “magic wavelength” from Hidetoshi Katori and coworkers [16], the scenario changed dramatically and a tremendous growth has been observed in the development of lattice clocks all over the world. The idea of tuning the lattice wavelength to a value where the light shift for both the clock states becomes equal, removed the inhomogeneous frequency shifts coming from the optical lattice. Over last decade, lattice clock performances have improved significantly faster compared to ion clocks, already reaching the accuracy levels of ion clocks. A big reason for this dramatic improvement has been the much better clock stability that can be achieved with neutral atom clocks, which allows to characterize the systematic shifts with much higher precision.

While discussing the improvements in optical clock performances, the outstanding efforts in developing ultrastable lasers cannot be ignored. To make full use of narrow optical atomic transitions with mHz or lower linewidths, light sources with at least sub-Hz linewidths are necessary. Such lasers are therefore stabilized to ultrastable resonators made from e.g. ultra-low expansion glass (ULE) glass or crystalline silicon, placed in an environment with incredible control of the temperature and vibration [17]. About a decade ago, such state of the art systems were limited in performance to about 1×10^{-15} fractional instability. Over the years, the remarkable technical improvements in ultrastable lasers in all aspects, such as resonator materials, mirror coatings [18] and control over residual amplitude modulation (RAM) effects [19] have brought us to a stage where these ultrastable lasers can in principle be seen as optical equivalents of Hydrogen Masers with instabilities already in the range of 10^{-17} fractional frequency fluctuations for a few 100 seconds of averaging time [20, 21]. Such ultrastable lasers are making it possible to perform spectroscopy with many seconds of probe time [22], thus inching closer to reach the limits of atomic transition linewidths 1.3.

Over these years of developments, advances have been made in not only better measurement and control of systematic shifts, but also in finding new sources of measurement errors such as nonlinear AC Stark shifts, or shifts coming from the amplified spontaneous emission (ASE) of lattice lasers. To combat the nonlinear AC Stark shifts, there was again a proposal from Katori and coworkers [23] to utilize not only the lattice wavelength, but also the lattice intensity and polarization to operate at the so called “operational magic condition” where the frequency

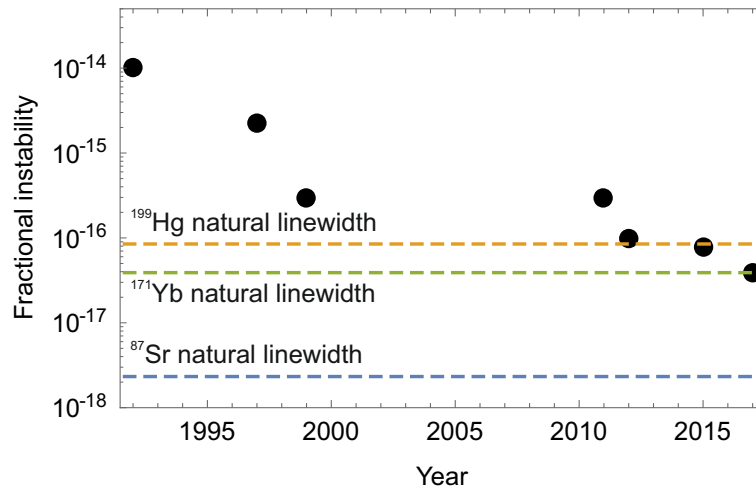


Figure 1.3: Instability of ultrastable lasers over last 30 years

shifts are constant or maybe even zero in first order with respect to small changes in lattice laser intensity. Recently there have been measurements in different groups identifying these operational magic conditions.

One major source of the uncertainty for optical clocks has been the Black body radiation (BBR) induced frequency shift. Technical advances in precise measurement [24] and novel system designs [25] have allowed these shifts to be brought down to the 10^{-18} regime for clocks operated at room temperature. However, such techniques have limitations and could potentially halt progress in improving clock accuracies. Therefore, while the idea of optical clock in cryogenic environment [26] has been explored, the search for new atomic elements such as magnesium, cadmium and mercury with low BBR sensitivity is an important field of research.

These dramatic improvements in optical clocks have already led to their performance surpassing microwave clocks. This not only leads to the possibility of a future re-definition of SI-second, but also for perhaps first time utilizing frequency measurements as very precise tools in diverse fields such as relativistic geodesy [27], spin-orbit coupling physics [28], search for variation of fundamental constants [29, 30], dark matter search [31] and even proposals for gravitational wave detection [32]. Recently, there have also been considerable innovations in developing novel protocols for optical trapping and spectroscopy. To reduce the effect of probe field induced shifts in clocks, different versions of hyper Ramsey spectroscopy protocols [33–39] have been studied. To reduce the atomic interaction induced frequency shifts, a Fermi degenerate 3D lattice clock has been developed [40] where atom numbers can be increased by orders of magnitude compared to current state of the art 1D lattice clocks. In such a setup, an in-situ instability in the 10^{-19} regime was recently demonstrated [41], and very interesting further developments are an-

anticipated. In many groups around the world, there has also been a push to develop an active optical clock [42–45] which could be a game changing technology. An active optical clock not only holds the promise of generating an atomic reference without the need for an external ultrastable oscillator, but such a system would have an instability averaging down as $1/\tau$, which would significantly reduce the required measurement times, opening up possibilities for numerous applications. There was first demonstration of super-radiant pulses in such an active laser system [44], as well as the first measurement of the frequency instability in the 10^{-16} regime [45]. Very recently, there have been a number of reports on development of optical clock experiments based on micro-trap arrays [46–49], which though not superior at the moment compared to lattice clock protocols, offers more control on individual atoms and could offer an interesting playground for using optical clocks as tools to study fundamental physics.

As optical clocks precision and accuracy have been steadily improving, there has been a debate about possible redefinition of SI-second. Recent results with clock uncertainties in 10^{-19} regime mean that these debates are no more about if, but rather about when such a redefinition would take place. Since Cs clocks have orders of magnitude higher uncertainties compared to optical clocks, the only way these optical clocks can validate their performances is by performing frequency ratio measurements. At this point, the remarkable developments in transfer of stability over fiber links has to be pointed out. Without these advancements, comparing clocks in different labs would not have been possible. The very early long distance frequency comparisons over fiber links were performed between PTB and LUH about a decade ago [50]. Since then, the technology of Erbium doped fiber amplifiers (EDFA) and fiber Brillouin amplifiers (FBA) [51–53] helped researchers build extensive international fiber links between different metrology labs [54, 55]. These fiber links running more than 1000 kms have already been shown to be capable of comparing frequency references with fiber induced shifts as low as 10^{-19} [54].

Development in all aspects of optical clocks and related fields has motivated CIPM to already include many of the optical frequency references as secondary representation of SI-second [56]. Following the consistent improvement in performance seen over last decade, a road-map has already been established at BIPM, detailing the necessary performances required to be demonstrated to initiate the SI-second re-definition process.

1.2 Motivation for a magnesium lattice clock

To establish optical clocks as the future time reference, the role of frequency comparisons between different labs is very important. To reliably measure frequency ratios, different atomic elements need to be used. This motivates development of optical clocks based on different atomic species. Furthermore, the research community gets to learn from the unique properties of each species leading to further enrichment of the knowledge.

	Sr	Yb	Hg	Yb+	Sr+	Al+	Hg+
PTB	1.5×10^{-17} [57]	-	-	2.7×10^{-18} [57]	-	-	-
INRIM	-	2.8×10^{-17} [58]	-	-	-	-	-
SYRTE	4.1×10^{-17} [54]	-	1.7×10^{-16} [59]	-	-	-	-
NPL	1.0×10^{-17} [60]	-	-	5×10^{-17} [61]	5×10^{-17} [62]	-	-
NIST	-	1.4×10^{-18} [63]	-	-	-	9.4×10^{-19} [64]	1.6×10^{-17} [12]
JILA	2×10^{-18} [24]	-	-	-	-	-	-
NMIJ	-	3.6×10^{-16} [65]	-	-	-	-	-
RIKEN	5.8×10^{-18} [66]	3.5×10^{-17} [66]	7.2×10^{-17} [67]	-	-	-	-
NRC	-	-	-	-	1.5×10^{-17} [68]	-	-

Table 1.1: List of major optical clock performances in various metrology labs around the world.

A summary of the current status of optical clock uncertainties in major metrology labs around the world is given in Table 1.1, where most optical clocks in major metrology institutes already operate at 10^{-17} level. The BBR induced frequency shift is one of the biggest uncertainty contributions for most of these optical lattice clocks. Therefore the research on new elements such as magnesium, cadmium [69] and mercury [70] with low BBR sensitivities becomes further important. While there has already been considerable research on development of Hg lattice clock, cadmium and magnesium have not been sufficiently explored for the development of optical lattice clocks in any of the major metrology institutes. In our lab, we have been working towards the development of a Mg lattice clock, building on our previous metrology research with magnesium in a free beam setup [71] and with cold atomic samples [72]. The low BBR sensitivity of magnesium [73, 74] (almost an order of magnitude smaller than strontium [75]) makes it a promising candidate that can push beyond the technical limit imposed by BBR shift in other room temperature clocks.

It is also noteworthy that magnesium is the lightest element out of all optical clock candidates. This has two important implications. First, having fewer core electrons means that atomic calculations become much easier. This therefore opens the possibility to even use theoretical calculations to predict hard to measure frequency shifts such as the BBR shift and quadrupole & magnetic dipole associated lattice frequency shifts. Understanding the differences between experimental measurements and theoretical predictions for simple systems, such as Mg and more complicated atomic systems can be useful in optimizing different atomic physics models.

Another advantage of developing a clock on an element with smaller atomic number is the small dependence of atomic energy levels on fine structure constant α . The atomic clock frequencies for an element with atomic number Z has relativistic corrections that vary approximately as $(\alpha Z)^2$ [76]. Therefore optical clocks with large difference in atomic number would be ideal for detecting any variations in fine structure constant [12]. Therefore magnesium is well suited as a reference clock in such a frequency comparison measurement.

The system development of the magnesium lattice clock and first frequency measurement in the 10^{-15} regime have been detailed in the PhD thesis from André Kulosa [77], Klaus Zipfel [78] and Dominika Fim [79]. Due to the requirement of relatively large optical power, line broadening induced by tunneling between lattice sites limited the clock performance to 10^{-15} regime. The work performed to further improve the performance of the Mg lattice clock is the main focus of this thesis. We aim to push the performance of our experimental setup to the 10^{-17} regime and therefore some upgrades to the setup were necessary. These upgrades as well as the resulting measurements form the main results of the thesis. In addition, a better understanding of spectroscopy in the shallow lattice regime for non-degenerate Bloch bands has been explored as well. To reach the desired performance levels, higher order lattice light shift needs to be characterized as well. In this work, first experimental studies of these higher order shifts have also been performed.

Outline of Thesis

In **chapter 2**, a brief introduction to the magnesium lattice clock will be given. The essential aim here is to give details on the relevant physics behind an optical lattice clock while using Magnesium as the principle example. The most important concepts and formalism necessary to quantify clock performance will also be introduced here. Furthermore, our experimental setup will be summarized briefly as well, with particular focus on some of the unique features.

Chapter 3 contains the first results of this thesis where the spectroscopy in deep optical lattice will be compared to shallow lattice regime. The gradual transition of lineshape from one regime to the other will be studied here at magic wavelength as well as for non-magic condition and the experimental results will be compared to an extensive theoretical model. Other line-broadening effects associated with lattice will be discussed in this chapter as well.

Chapter 4 deals with the details of experimental system upgrades and their effect on the stability of lattice clock. The reduction in linewidth of the clock tran-

sition forms the major part of this chapter. Furthermore, the improvement in self-comparison instability measurements due to lower transition linewidth is analyzed in this chapter.

Chapter 5 details the improved systematic shift measurements building on the results from chapter 4. Besides the probe AC Stark shift, Zeeman shift and density shift, the lattice AC Stark shift is studied in detail. Particular focus has been on measuring the influence of higher order lattice AC Stark shifts.

In **chapter 6**, an outlook on future development of Magnesium clock is presented. Details on current limitations of the measurements as well as pathways to mitigate these limitations are given.

A Magnesium lattice clock

In this chapter, technical details of a lattice clock setup will be discussed with help of magnesium as an example. This would allow for an introduction to the physics of lattice clocks as well as a deeper look into the unique features of our magnesium lattice clock experiment. Afterwards, experimental details such as laser systems, magnetic field system etc required for the experiment will be discussed.

2.1 Atomic structure of Magnesium

Optical lattice clocks are based on Alkaline earth (-like) elements with two outer shell electrons, which facilitates the presence of a high-Q atomic transition [80]. Following Hund's law, these electrons can either pair in a symmetric state with total spin $S = 1$ (Triplet states), or in an anti-symmetric configuration with total spin $S = 0$ (Singlet states). Transitions between electronic states of these singlet- and triplet-manifolds are forbidden if spin-orbit interaction is negligible. Though these intercombination transitions become weakly allowed once spin-orbit interaction is included (which is larger for heavier elements), the transition between the lowest singlet and triplet states ($^1S_0 - ^3P_0$) still remains strongly forbidden due to total angular momentum conservation. The presence of nuclear spin for fermionic isotopes makes this transition weakly allowed with sub-Hz linewidths. This transition is therefore of interest for optical lattice clock development. Since the clock states have zero total angular momentum, the first order Zeeman shift is also zero, though that changes once nuclear spin is included in the discussion.

The level scheme relevant for magnesium optical clock is shown in Fig. 2.1. As stated above, the clock states are the lowest energy states of singlet (1S_0) and triplet manifolds (3P_0). Magnesium has three isotopes: ^{24}Mg (79% abundance), ^{25}Mg (10%) and ^{26}Mg (11%). Being the fermionic isotope, ^{25}Mg would be the first choice for lattice clock development. But to be used as a lattice clock, atoms need to be sufficiently cooled to be trapped in the optical lattice. The first obvious step to cooling is based on the 285 nm $^1S_0 - ^1P_1$ transition. Due to a large linewidth of 78 MHz, the atoms can at best be cooled down to the Doppler limit of around 3 mK. Therefore a second stage of cooling is necessary to achieve lower temperatures. Typically, for alkaline earth elements, the $^1S_0 - ^3P_1$ transition has a linewidth in the order of a few tens of kHz, which is ideal for cooling the atoms down to μK regime. However, this is not possible for magnesium since this transition is extremely narrow at 36 Hz. Therefore, a second stage cooling can only be based on $^3P_2 - ^3D_3$ transition with additional re-pumpers from 3P_1 and 3P_0 states as shown in Fig. 2.1. This cooling scheme immediately highlights the difficulty of cooling fermionic magnesium due to additional complexity arising from hyperfine splitting of a few hundred MHz. Therefore, the magnesium clock development work in our lab has been focused on the bosonic ^{24}Mg .

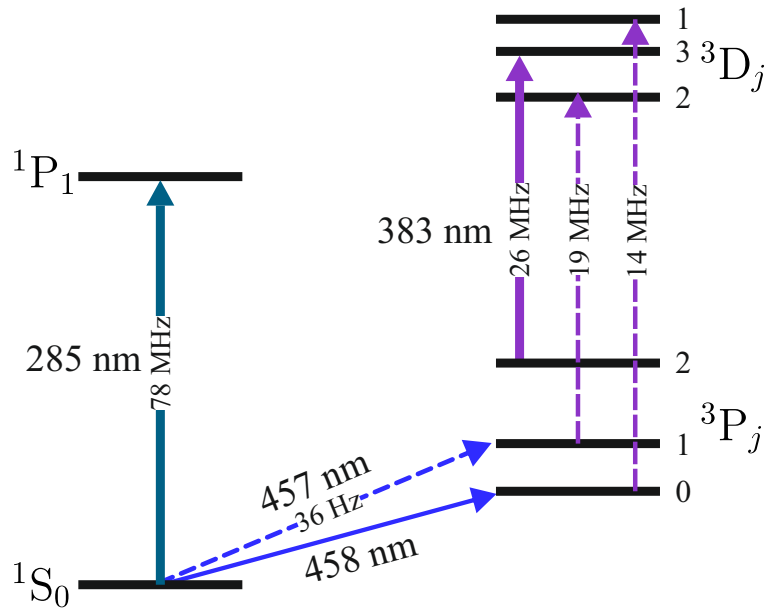


Figure 2.1: Energy level scheme for ^{24}Mg , where all relevant transitions for clock operation are shown.

Before developing the lattice clock in our lab, an optical frequency measurements of $^1S_0 - ^3P_1$ transition in a Ramsey Borde experiment had already been performed [71]. While this narrow 36 Hz intercombination transition does not allow for efficient Doppler cooling, it was suited for a first frequency measurement in 10^{-14} regime.

For a frequency reference, the influence of external fields has to be minimized and characterized with great precision. In addition, the dominant line-broadening mechanism that can reduce the line-Q have to be controlled as well as an efficient spectroscopy of such narrow (for bosons, forbidden) transitions needs to be ensured. Next sections deal with these challenges in development of an optical lattice clock.

2.2 Doppler- and recoil-free spectroscopy

Free atoms always move with a non-zero velocity. Performing spectroscopy of such atoms would lead to optical Doppler shift much like the Doppler shift for acoustics. Depending on the temperature of atomic cloud, the atomic velocities will be distributed around the mean velocity. This therefore gives rise to a distribution of frequency shifts around a mean value. For typical temperatures in cold atomic samples, this can be as high as a few kHz. In addition, absorption of a photon by a free atom has an associated photon recoil shift. Therefore these two effects do not allow for optimum use of the narrow clock transitions. To suppress recoil and Doppler shift in optical clocks, it is necessary to perform spectroscopy in the Lamb-Dicke regime [11] where the atomic transition takes place without changing the motional state. In neutral atom optical clocks, the ideal way to reach this regime is by trapping atoms in optical lattices [81]. In late 1990's, optical lattices were predominantly studied for their utilization in Raman sideband cooling of the atomic clouds [82–84] trapped in the Lamb-Dicke regime. But in optical clocks, this sub-wavelength trapping allows suppression of the recoil and Doppler shifts.

There are many ways in which the Lamb-Dicke regime can be understood. One such approach is to consider a free particle as a limit condition of a particle trapped in a box potential as the size of the box becomes infinite. For the case of particle in a box (this was also the case considered in original paper by R. H. Dicke [11]), the energies are quantized as

$$E_n = \frac{n^2\pi^2\hbar^2}{2mL^2} \quad (2.1)$$

where n is the quantization index, and L is the length of the box. The wavefunctions are also defined completely by n and L

$$\psi_n(x) = \begin{cases} \sqrt{\frac{2}{L}} \sin\left(\frac{n\pi}{L}\left(x + \frac{L}{2}\right)\right) & -\frac{L}{2} < x < \frac{L}{2} \\ 0 & \text{otherwise} \end{cases} . \quad (2.2)$$

Assuming an atom in one of these eigenstates to be interacting with an electromagnetic field with wavevector k , the excitation probability from state n to n' can

be calculated:

$$\begin{aligned}
 P_{n \rightarrow n'} &\sim \int_{-\frac{L}{2}}^{\frac{L}{2}} \psi_{n'}^*(x) \exp(ikx) \psi_n(x) dx \\
 &= \frac{4ie^{-\frac{1}{2}ikL} \left((-1)^{n_1+n_2+1} + \exp(ikL) \right) kLn_1n_2\pi^2}{k^4L^4 + (n_1^2 - n_2^2)^2\pi^4 + 4n_1n_2k^2L^2\pi^2} \quad .
 \end{aligned} \tag{2.3}$$

Now Eq. 2.3 can be used to look at the change in the transition probability between different states as the strength of confinement is varied from strong confinement ($L \lesssim 1/k$) to the free particle regime ($L \gg 1/k$). As can be seen in Fig. 2.2, for strong confinement where the length of the box is of the same order as the wavelength of excitation laser, the probability to change motional state is negligible. On the contrary, for a weakly confined particle where the length of the box is much larger than the wavelength of laser, the excitation process has a very strong probability to change the motional energy of the particle, leading to a significant frequency shift due to the excitation process. This is precisely the source of recoil and Doppler shift.

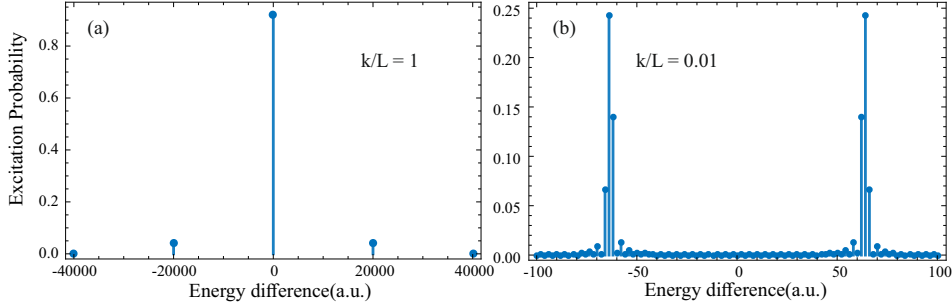


Figure 2.2: Excitation probabilities for different degrees of confinement: (a) For strong confinement, excitation/de-excitation process has a very small probability to change the motional state, and therefore the associated Doppler shift/broadening is small whereas for the case of weak confinement(b), it is in fact more probable to change the motional state during excitation or de-excitation process and hence the associated Doppler shift/broadening is very large.

Further using Eq. 2.3, it can be shown that the probability for staying in the same motional state is

$$P_{n \rightarrow n} = \frac{\sin\left(\frac{kL}{2}\right)^2}{\left(\frac{kL}{2}\right)^2} \tag{2.4}$$

This is plotted in Fig. 2.3, where one can clearly see that as the length of box becomes larger than probe laser wavelength, the probability of preserving the motional state in an excitation process becomes much smaller than 1. This therefore sets a cut-off regime where optical clocks can operate to suppress Doppler and recoil shifts. This is precisely the condition for *Lamb-Dicke regime*:

$$L \ll \lambda \tag{2.5}$$

The condition in Eq. 2.5 can also be re-written in terms of energy by converting both length scales to their respective energy counterparts. The length of the box scales the quantized energy values for the stationary states given by Eq. 2.1, and the wavevector k (or wavelength λ) of the spectroscopy light can be converted to the recoil energy $E_{\text{recoil}} = \frac{\hbar^2 k^2}{2m}$ associated with the photon absorption by an atom of mass m in free space. The *Lamb-Dicke regime* can therefore be expressed as

$$E_{\text{recoil}} \ll E_{\text{trap}} \quad (2.6)$$

where E_{trap} is the energy separation between quantized states which provides the energy scale of the confinement of atoms in a trap.

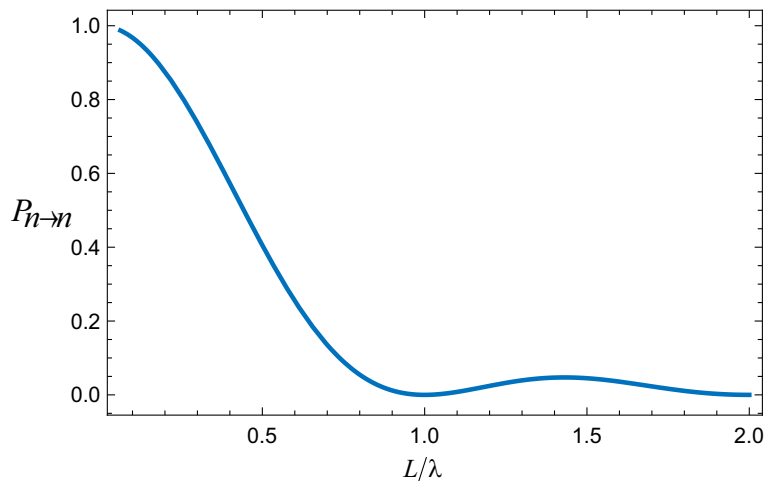


Figure 2.3: Probability of preserving the motional state during excitation process is shown here as a function of length of the box potential.

For neutral atom traps, strong confinement can be achieved by using a far detuned optical lattice. The intensity pattern obtained from interference of a monochromatic laser beam with a back-reflected copy of itself generates the spatially modulated potential with periodicity of half the laser wavelength. If the depth of potential is high enough, atoms can be confined to individual wells of the lattice where they would satisfy the Lamb-Dicke criterion. In the literature, there are plenty of resources available where spectroscopy in a harmonic oscillator trap potential is discussed in detail. Since the individual lattice sites can be reasonably well approximated by harmonic oscillator potential, these analyses apply quite well to spectroscopy in optical lattices as well. However, since in this thesis the details of shallow as well as deep optical lattice depth regime will be looked into, an analysis of Lamb-Dicke spectroscopy from the point of view of periodic lattice potentials will be discussed here. Whenever necessary, the approximation to harmonic potential will also be utilized to highlight the transition into deep lattice regime.

Spectroscopy in optical lattice

To perform Doppler and recoil free optical spectroscopy, the atoms need to be confined to sub-wavelength regions. Optical lattices provide the necessary trapping potentials to achieve such strong confinement. Typically optical lattice is generated by back reflecting a single mode laser beam such that it interferes with itself. For our magnesium lattice clock, an optical lattice is created inside an enhancement cavity where significantly higher intra-cavity intensity leads to much deeper trap depth. Such an interference pattern can be written as

$$I(r, z) = \frac{2}{\eta} \left[\left(\frac{\epsilon_0 w_0}{w(z)} \right)^2 \exp(-2r^2/w(z)^2) \sin^2(k_L z) \right], \quad (2.7)$$

where η is the impedance of the medium in which wave is traveling, ϵ_0 is the permittivity of free space, w_0 is the beam waist, k_L is the wave vector, $w(z) = w_0 \sqrt{1 + (z/z_R)^2}$ is the beam radius at position z and $z_R = \frac{k_L w_0^2}{2}$ is the Rayleigh range for the Gaussian beam. This can be re-written in terms of incident laser power P_0 as

$$I(r, z) = \frac{8P_0}{\pi w(z)^2} \exp(-2r^2/w(z)^2) \sin^2(k_L z). \quad (2.8)$$

And if the AC polarizability of the atom is α , the potential experienced by the atom would be

$$U(r, z) = \frac{8P_0 \alpha}{\pi c \epsilon_0 w(z)^2} \exp(-2r^2/w(z)^2) \sin^2(k_L z). \quad (2.9)$$

This equation can be rewritten as

$$U(r, z) = \frac{U_0}{1 + (z/z_R)^2} \exp(-2r^2/w(z)^2) \sin^2(k_L z), \quad (2.10)$$

where $U_0 = \frac{8P_0 \alpha}{\pi c \epsilon_0 w_0^2}$. Assuming the region of interest to be well within the Rayleigh range $w(z) \approx w_0$, this complete potential can be re-written to separate terms of different order in r and z .

$$U(r, z) = U_0 \sin^2(k_L z) - \frac{U_0}{w_0^2} r^2 + \frac{U_0}{2} \left(\frac{2r^2}{w_0^2} - 1 + \exp\left(\frac{-2r^2}{w_0^2}\right) \right) - \frac{U_0}{2} \left(\exp\left(\frac{-2r^2}{w_0^2}\right) - 1 \right) \cos(2k_L z), \quad (2.11)$$

In the Eq. 2.11, the third term is all the non-harmonic corrections to the Hamiltonian in the radial axis, whereas the fourth term gives the contribution coming from coupling of the radial and axial Hamiltonian terms. Analysis of this complete potential will be the subject matter for next chapter. However, for now to

understand spectroscopy in the Lamb-Dicke regime in an optical lattice, a deep optical lattice potential with depth much larger than the atomic temperature, and Rayleigh range much larger than the atomic cloud size is considered. In such a case, the higher order transverse contributions can be neglected and the potential takes the simplified form

$$U(r, z) = U_0 \sin^2(k_L z) - \frac{U_0}{w_0^2} r^2. \quad (2.12)$$

This potential captures the most important aspects of lattice physics. The first term is the more important periodic potential that gives the strong confinement necessary for achieving the Lamb-Dicke regime. This term originates from the interference of the laser beam with itself. The second term on the other hand is the direct result of Gaussian beam profile and therefore the associated dipole potential can be approximated in the vicinity of the trap center by a harmonic potential. Therefore in the transverse axes, the eigenstates are simply harmonic oscillator states quantized by the transverse quantum numbers n_x and n_y . This leads to an important observation for spectroscopy in 1D optical lattice. Since the atoms in transverse axes will always be weakly confined ($w_0 \gg \lambda$), it is important to suppress the excitation process that couples the transverse states. This can most easily be achieved by aligning the spectroscopy laser beam with the lattice axis, which ensures that the excitation field with wavevector k_{clock} has no component along the transverse axes. Therefore the coupling between two transverse states $|n_x\rangle$ and $|n'_x\rangle$ will be

$$P_{n_x \rightarrow n'_x} \sim \langle n'_x | \exp(ik_{\text{clock}}z) | n_x \rangle = \delta_{n_x n'_x}. \quad (2.13)$$

First most obvious approximation right now could be to further expand the periodic potential in the neighborhood of a minimum and only keep the terms up to second order. Such a harmonic approximation allows for a similar analysis as in the last section. The only qualitative difference is in the energy spacing, which unlike a box potential is constant for all states in a harmonic oscillator potential. However, for completeness, as well as anticipating the requirements of the next chapter, the complete, periodic potential will be considered here, and the transition from strong trapping to a free particle can then straightforwardly be varied by varying the parameter U_0 .

The Hamiltonian for the motion along z -axis can be written as

$$H_z = \frac{\hat{p}^2}{2m} + \frac{U_0}{2} (1 - \cos(2k_L \hat{z})) \quad (2.14)$$

Since the potential considered here is periodic along z -axis, the Bloch theorem states that a set of eigenstates can be written as

$$\psi_{n,q}(z) \sim \exp(iqz)u_n(z), \quad (2.15)$$

where $u_n(z + \pi/k_L) = u_n(z)$ is also a periodic function with same periodicity as the lattice potential. Looking at the ansatz in Eq. 2.15, free particle wave functions would be the ideal choice for numerically solving for the eigenstates. Therefore the Hamiltonian can be re-written in harmonic wave basis

$$H_{k'k} = \left(\frac{\hbar^2 k_L^2}{2m} + \frac{U_0}{2} \right) \delta(k - k') - \frac{U_0}{4} (\delta(k' - (k + 2k_L)) + \delta(k' - (k - 2k_L))) \quad (2.16)$$

Such a representation of the Hamiltonian immediately makes it clear that the Hamiltonian is periodic in reciprocal space with a period of $2k_L$. Therefore the energy spectrum can also be understood completely within the first Brillouin zone (restricted zone scheme) $q \in]-k_L, k_L]$. To numerically calculate the energy spectrum, the Hamiltonian in Eq. 2.16 can be diagonalized

$$\begin{aligned} H |n, q\rangle &= E_{n,q} |n, q\rangle \\ |n, q\rangle &= \sum_{i=-\infty}^{\infty} C_{n,\kappa_{i,q}} |\kappa_{i,q}\rangle \end{aligned} \quad (2.17)$$

where $\kappa_{i,q} = q + 2ik_L$. At any given value of q , there will be infinite discrete energy levels indexed by n . Due to its similarity with the wavevector of a free particle, q is referred to as the quasimomentum. At this point, it is important to highlight this similarity as well as the differences between the two. For a free particle, the wavefunction is simply given by its wavevector k_f

$$\psi_f \sim \exp(ik_f z) \quad (2.18)$$

This wavevector is directly related to momentum of the particle $p = \hbar k_f$. Now the similarity of k_f with q lies in the Eq. 2.15 where the phase modulation of the wavefunction is also determined by q . Further similarities between the two show up in the energy spectrum, which will be discussed later in the section. The major difference between momentum and quasi-momentum lies in the symmetry breaking of the system. While momentum is a conserved quantity for a free particle in free space, quasi-momentum is conserved only within the Brillouin zone.

The energy spectrum obtained by diagonalizing the Eq. 2.17 is plotted in Fig. 2.4(a) for $U_0 = 0$, and $U_0 = 5E_R$ (Fig. 2.4(b)). The spectrum in Fig. 2.4(a) is nothing but the folded parabolic dispersion of a free particle. Now the similarity between quasimomentum q and momentum of a free particle k_f becomes clearer where one can see that a smooth transition from quasimomentum to momentum is possible as the trap depth is lowered to $U_0 = 0$.

Using this formalism, one can again understand the origin of Doppler and recoil shifts. For the parabolic dispersion relation for a free particle, the motional energy $E = (\hbar^2 k_f^2)/2m$ depends only on the velocity v or the corresponding wavevector k_f .

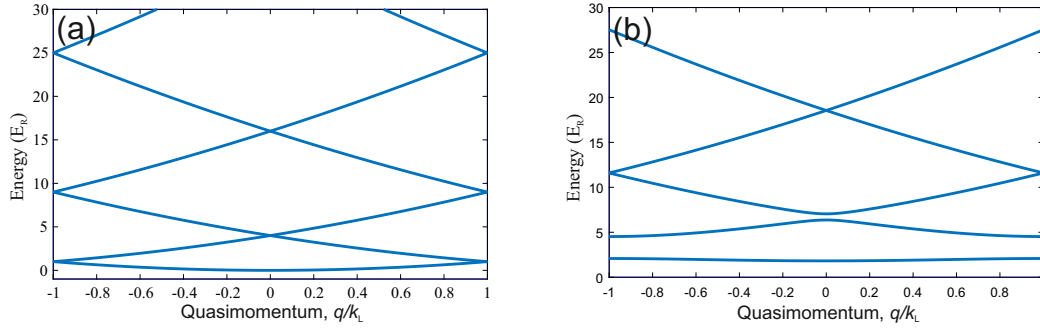


Figure 2.4: (a) Energy spectrum in restricted zone scheme for $U_0 = 0$ and (b) for $U_0 = 5E_R$

In such a case, the momentum conservation implies that the final momentum of the particle is direct sum of initial momentum and the recoil momentum imparted by the photon:

$$k_2 - k_1 = k_{\text{clock}} \quad (2.19)$$

where k_1 , k_2 and k_{clock} are the initial, final and photon wavevectors respectively. The energy dispersion relation gives the change in energy from absorbing the photon

$$\begin{aligned} \Delta E &= \frac{\hbar^2}{2m} (k_2^2 - k_1^2) \\ &= \frac{\hbar^2}{2m} (k_2 + k_1) k_{\text{clock}} \\ &= \frac{\hbar^2}{2m} (2k_1 + k_{\text{clock}}) k_{\text{clock}} \\ &= \frac{\hbar^2}{2m} 2k_1 k_{\text{clock}} + \frac{\hbar^2 k_{\text{clock}}^2}{2m} \end{aligned} \quad (2.20)$$

The second term in Eq. 2.20 is nothing but the definition for photon recoil energy E_R . The first term is the Doppler energy shift which can be re-written in usual formalism as

$$\Delta\nu_D = \nu_0 \frac{v}{c} \quad (2.21)$$

where ν_0 is the unperturbed frequency of the incident photon. Establishing these relations are important to highlight that both the recoil as well as Doppler shift can be fully understood from the energy dispersion relations, where the sum of both shifts is nothing but the result of change in energy corresponding to a change in momentum from absorbing a photon.

Now the effect of periodic potential can be qualitatively understood. First, rather straightforward observation is the flattening of the dispersion relation in the lowest band. This therefore means that the energy shift associated with equivalent change in quasimomentum will be smaller. The width of these Bloch bands therefore dictate the change in energy from absorbing photon momentum. And since the width of the band decreases as the trap depth U_0 is increased, as can be seen in Fig. 2.5, the energy shift associated with photon absorption also decreases as the trap depth is increased.

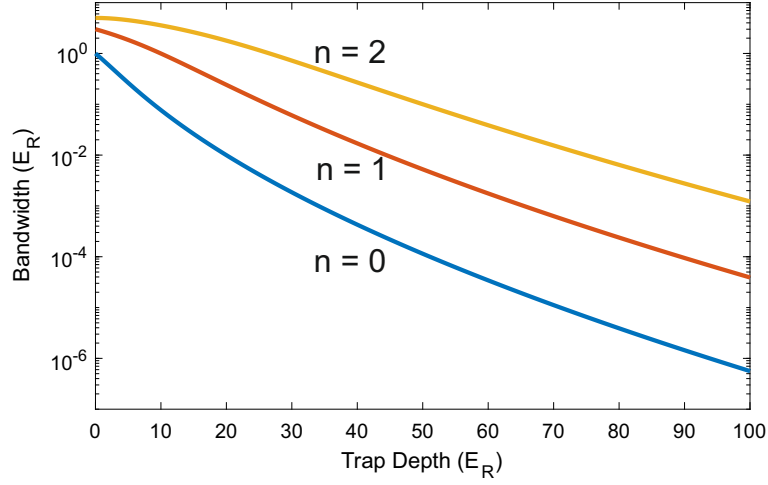


Figure 2.5: Energy bandwidth for three lowest Bloch bands as a function of trap depth.

A natural question arises with introduction of periodicity in energy spectrum. After absorbing a photon, an atom can make a transition to any of the bands within the Brillouin zone. This seems counter-intuitive as we transition to the case of a free particle, where as we saw in Eq. 2.20, there is only one transition possible on the parabolic energy spectrum. This can be resolved by looking at the probability of excitation to each of the neighboring bands as the trap depth U_0 is varied. A comparison between transitions starting from both edges of the Brillouin zone is particularly interesting.

$$P_1 \sim |\langle n = 0, q = -k_L/2 | \exp(ik_{\text{clock}}z) | n' = 0, q' = -k_L/2 + k_{\text{clock}} \rangle|^2 \quad (2.22)$$

$$P_2 \sim |\langle n = 0, q = -k_L/2 | \exp(ik_{\text{clock}}z) | n' = 1, q' = -k_L/2 + k_{\text{clock}} \rangle|^2 \quad (2.23)$$

$$P_3 \sim |\langle n = 0, q = k_L/2 | \exp(ik_{\text{clock}}z) | n' = 0, q' = k_L/2 + k_{\text{clock}} \rangle|^2 \quad (2.24)$$

$$P_4 \sim |\langle n = 0, q = k_L/2 | \exp(ik_{\text{clock}}z) | n' = 1, q' = k_L/2 + k_{\text{clock}} \rangle|^2 \quad (2.25)$$

where k_{clock} is the wavevector of the probe laser, which is approximately equal to k_L . These relative probabilities are plotted in Fig. 2.6.

At lower trap depths, it is interesting to see that P_1 is much larger than P_3 , which appears to be strange since there is no obvious reasons for differentiating between transitions starting from different quasimomenta. It is important here to note that in case of P_1 and P_2 , both the initial as well as the final quasimomenta lie in the first Brillouin zone (BZ), whereas in case of P_3 and P_4 , initial quasimomentum lies in the first BZ, while the final quasimomentum lies in the second BZ. As the trap depth approaches zero, it is expected that the probability $P_3 \rightarrow 0$ since P_4 would be the only allowed transition on the parabolic energy spectrum of a free particle. For very large trap depths, the intra-band transition probabilities become independent of q and also much larger than inter-band transitions. This, along with

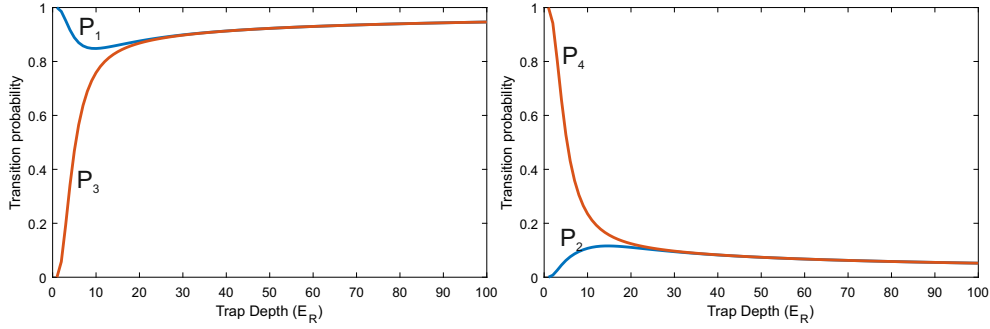


Figure 2.6: Relative probability of transition from lowest band to lowest band (left) and the first excited band (right)

the reduction in band-width with trap depth, leads to a suppression of Doppler and recoil shift.

As the trap depth U_0 increases, the interband transitions corresponding to motional sidebands become smaller, while at the same time, the sideband frequency separation becomes large, which helps resolve the inter-band transition. To add to these, the bands become flatter as well, which leads to much smaller frequency shifts associated with a change in quasi-momentum within an intra-band transition. All these features can be seen in the Fig. 2.7.

Fig. 2.7 is calculated assuming a uniformly filled distribution in the two lowest bands. As the trap depth increases, the Doppler broadened line splits into the “carrier” line corresponding to the transitions maintaining the motional quantum number n , and the blue- and red- “sidebands” on either side that correspond to a change in n by ± 1 . The sidebands are additionally modified due to contributions from the radial states. These effects will be discussed elsewhere. Additionally the curvature of the band influences the carrier lineshape as can be seen at lower trap depths. As the trap depth becomes large enough such that the bandwidth becomes smaller than the Rabi frequency, these deformations cannot be resolved. These features in the carrier lineshape at low trap depths will be a topic for the next chapter and will be discussed in detail there. But, most importantly, at large lattice depths, the Doppler broadening can be reduced to mHz regime. This helps improve the line-Q for the clock spectroscopy.

From the analysis above, one can see the transition from spectroscopy in free particle regime to spectroscopy in deep optical lattice such that the effects of atomic motion and photon recoil are suppressed. This is again quantifiable using the Lamb-Dicke parameter

$$\eta = \sqrt{\frac{E_R}{E_{\text{trap}}}} \quad (2.26)$$

where E_{trap} is the trap frequency which corresponds to the energy separation be-

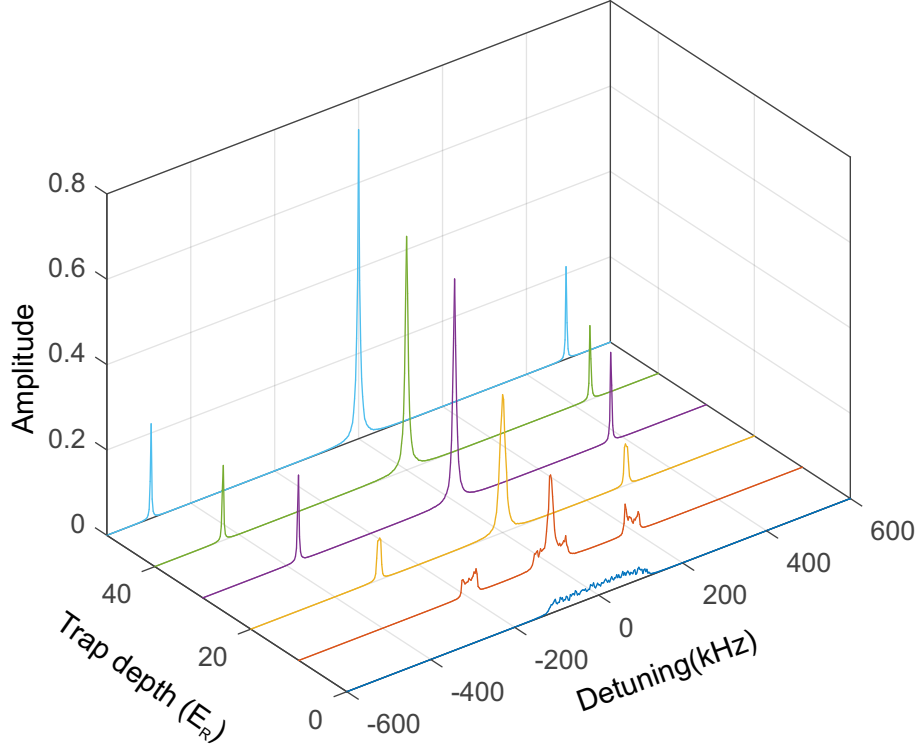


Figure 2.7: Spectrum calculated for the Hamiltonian in Eq. 2.16 for different values of U_0 , where the bands are assumed to be uniformly populated.

tween neighboring bands. As the trap depth is increased, the Bloch bands become flatter along with increase in E_{trap} leading to suppression of Doppler and recoil shifts in the Lamb-Dicke regime $\eta \ll 1$.

2.3 What about the lattice AC Stark shift?

To suppress the Doppler and recoils shifts, optical lattices or such similar traps are necessary for neutral atoms. But, in presence of such strong light fields, there are strong lattice light induced frequency shifts. In fact these energy shifts are responsible for generating trapping force and to enter the Lamb-Dicke regime, large energy shifts are necessary. Typically these energy shifts are vastly different for different atomic states and that is the case with the clock states as well, leading to large differential AC Stark shift of the clock transition.

To overcome these influences of light shifts on atomic transitions, the idea of a magic wavelength lattice was introduced, first for efficient cooling in optical traps [16], and then to perform Doppler and recoil free spectroscopy in optical lattices

[85]. The frequency shift of the clock transition in presence of the lattice with intensity I_L is

$$\Delta\nu_{AC}(\lambda_L) = -\frac{\Delta\alpha(\lambda_L)}{2\epsilon_0 ch} I_L + \mathcal{O}(I_L^2) \quad (2.27)$$

where λ_L is the wavelength of lattice laser and $\Delta\alpha(\lambda_L)$ is the AC polarizability difference between the two states. Now if we adjust the polarizabilities of the two states by varying the lattice wavelength such that $\Delta\alpha(\lambda_m) = 0$, then to first order in intensity, the lattice AC Stark shift can be tuned to zero as well. This lattice wavelength λ_m where light induced frequency shifts for the clock transition disappear is called the “magic wavelength”. There are higher order frequency shifts, but, they are much smaller.

The dynamic polarizability α_i for an atomic state i in presence of a light field of angular frequency $\omega_L = \frac{2\pi c}{\lambda_L}$ can be calculated using the dipole matrix elements $|\langle\phi_j|\mathcal{D}|\phi_i\rangle|^2$ between all states j to state i ,

$$\alpha_i(\lambda_L) = 2e^2 \sum_j \frac{\hbar\omega_{ij} |\langle\phi_j|\mathcal{D}|\phi_i\rangle|^2}{\hbar^2(\omega_{ij}^2 - \omega_L^2)} \quad (2.28)$$

where ω_{ij} is the angular frequency corresponding to the transition from state i to state j . Eq. 2.28 can be re-written in terms of transition rates A_{ij}

$$\alpha_i(\lambda_L) = 6\pi\epsilon_0 c^3 \sum_j \frac{A_{ij}}{\omega_{ij}^2(\omega_{ij}^2 - \omega_L^2)} \quad (2.29)$$

Further modification to this relation coming from the fine structure is avoided in case of optical lattice clocks since both states have total angular momentum $J = 0$.

The calculated polarizability for the states 1S_0 and 3P_0 is shown in Fig. 2.8. As can be seen here, the two curves cross each other around 468 nm. This is the magic wavelength for the magnesium clock transition. More detailed theoretical models can provide a much more precise value for the magic wavelength. Such a calculation by M. Safronova and colleagues provided a value of 468.45(23) nm [74], in remarkable agreement with the experimentally measured value of 468.4106(2) [79].

With suppression of lattice induced AC Stark shifts, high precision spectroscopy can be performed where full potential of the narrow optical transition can be utilized.

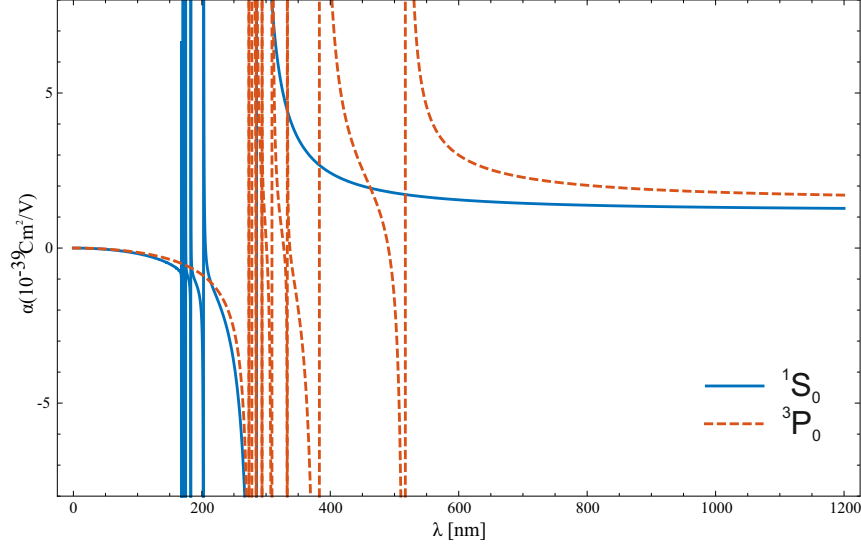


Figure 2.8: Dynamic polarizability of magnesium clock states 1S_0 and 3P_0 . The lattice wavelengths where the two curves intersect represent the magic wavelength condition.

2.4 Spectroscopy of a forbidden transition

As mentioned already, the clock transition for optical lattice clocks is the dipole forbidden $^1S_0 - ^3P_0$ transition. Therefore the question arises: how to perform spectroscopy of such forbidden transitions? To understand this, a bit more detailed look into the atomic structure is necessary. Magnesium, like all alkaline earth (-like) elements has two valence electrons. The total spin-orbit interaction energy is

$$H_{s-o} = \beta_1 \mathbf{s}_1 \cdot \mathbf{l}_1 + \beta_2 \mathbf{s}_2 \cdot \mathbf{l}_2 \quad (2.30)$$

where \mathbf{s}_i and \mathbf{l}_i are the spin and orbital angular momentum, while β_i is the spin-orbit interaction strength of the two individual outer shell electrons i . Since the spin-orbit interaction is weak for lighter elements, it only acts as a perturbation on the state $|\mathbf{L}, \mathbf{M}_L, \mathbf{S}, \mathbf{M}_S\rangle$, where $\mathbf{L} = \mathbf{l}_1 + \mathbf{l}_2$ and $\mathbf{S} = \mathbf{s}_1 + \mathbf{s}_2$. The details on this LS coupling scheme can be found in much more detail elsewhere[86]. But since the total spin, \mathbf{S} and total orbital angular momentum \mathbf{L} are assumed to be conserved, H_{s-o} can be re-written as

$$H_{s-o} = \beta_{LS} \mathbf{L} \cdot \mathbf{S} \quad (2.31)$$

Since the total angular momentum J in LS coupling is given as $\mathbf{J} = \mathbf{L} + \mathbf{S}$, the spin-orbit interaction can be re-written as

$$H_{s-o} = \beta_{LS} \frac{\mathbf{J} \cdot \mathbf{J} - \mathbf{L} \cdot \mathbf{L} - \mathbf{S} \cdot \mathbf{S}}{2}. \quad (2.32)$$

Therefore the spin-orbit interaction leads to lifting of the degeneracy of states with different total angular momentum J ,

$$E_{s-o} = \frac{\beta_{LS}}{2} (J(J+1) + L(L+1) - S(S+1)) \quad (2.33)$$

and the term ^{2S+1}L therefore splits into its $^{2S+1}L_J$ components. This representation of atomic states is named Term symbols.

The electric dipole operator responsible for electronic excitation has no spin dependent term. Therefore as long as LS coupling approximation is satisfied, there can be no electronic transitions between singlet and triplet states. Therefore, being the lowest energy state in triplet manifold, 3P_0 has essentially an infinite lifetime and the $^1S_0 - ^3P_0$ transition has vanishing linewidth. However, the same spin-orbit interaction responsible for splitting the $^{2S+1}L_J$ states also mixes some 1P_1 wavefunction into the 3P_1 wavefunction, which results in a non-zero transition probability to 1S_0 state. In case of ^{24}Mg , this $^1S_0 - ^3P_1$ transition linewidth is only 36 Hz, and it generally becomes larger for heavier atoms due to growing departure from the pure LS coupling model.

Up to this point, the clock transition is still forbidden and does not allow for a dipole excitation. The situation changes once the nuclear spin is included in the discussion. For isotopes with nuclear spin, $I \neq 0$, the hyperfine interaction produces a mixing of the 3P_0 state with 3P_1 , 3P_2 and 1P_1 states. This therefore opens the possibility of atoms decaying from the 3P_0 state to the ground state with lifetime ranging from few seconds to thousands of second for different elements. This is one of the reasons why most advanced optical lattice clock experiments are based on fermionic isotopes.

Though hyperfine interaction makes the clock transition weakly allowed for fermionic isotopes, bestowing them with just the perfect conditions for their application as optical lattice clocks, the clock transition in bosons still remain strongly forbidden. This is where the idea of using external coupling field played a pivotal role [87]. An external homogeneous magnetic field B can be used to introduce a small coupling between the 3P_1 and 3P_0 states, giving rise to a small admixture of 3P_1 state with the clock state 3P_0 . This state mixing, which can be quantified by the magnetic field dependent Rabi frequency $\Omega_B = \langle ^3P_0 | \mu \cdot \mathbf{B} | ^3P_1 \rangle / \hbar$ produces the modified state

$$|^3P'_0\rangle = |^3P_0\rangle + \frac{\Omega_B}{\Delta_P} |^3P_1\rangle \quad (2.34)$$

where Δ_P is the energy difference between states 3P_1 and 3P_0 . The effective Rabi frequency thus generated for exciting the clock transition is

$$\Omega_{\text{clock}} = \frac{\Omega_L \Omega_B}{\Delta_P} \quad (2.35)$$

where Ω_L is the Rabi frequency coupling between the ground state 1S_0 with the 3P_1 state. The effective linewidth of the clock transition is therefore also modified due to the state mixing

$$\gamma_{\text{eff}} = \gamma \frac{\Omega_L^2/4 + \Omega_B^2}{\Delta_P^2} \quad (2.36)$$

where γ is the $^1S_0 - ^3P_1$ transition linewidth. Since Ω_L and Ω_B depend directly on the probe laser intensity I and the homogeneous magnetic field B , Eq. 2.35 can be written as

$$\Omega_{\text{clock}} = \alpha\sqrt{I} |B| \cos \theta \quad (2.37)$$

where α gives the dependence of Rabi frequency on the probe fields and θ is the angle between the homogeneous magnetic field and the polarization of the probe laser light. Since quadratic Zeeman shift is $\Delta_B = \beta B^2$ and AC Stark shift due to probe light field is $\Delta_L = \kappa I$, the effective Rabi frequency can also be written as

$$\Omega_{\text{clock}} = \xi \sqrt{|\Delta_L \Delta_B|} \cos \theta \quad (2.38)$$

where $\xi = \alpha/\sqrt{\beta\kappa}$. Theoretically calculated values of these parameters for Mg are [87]

$$\alpha = 98 \text{ Hz}/(\text{T}\sqrt{\text{mW}/\text{cm}^2}), \quad \beta = -217 \text{ MHz}/\text{T}^2, \text{ and } \kappa = -0.5 \text{ mHz}/(\text{mW}/\text{cm}^2). \quad (2.39)$$

This method therefore allows to generate Rabi frequency up to 100 Hz using laser intensities of up to 100 mW/cm², and homogeneous magnetic field of 100 G. Of course a trade-off between the strength of both the fields is necessary due to the associated frequency shifts.

This technique of magnetic field induced spectroscopy opens the field of optical lattice clocks to all the bosonic isotopes of the alkaline earth (-like) elements. The disadvantage of this method is the large quadratic Zeeman shift associated with the homogeneous field B , but yet the bosons allow for a much lower complexity in atomic structure as well as the associated linear Zeeman shift. The magnetic field induced spectroscopy has been used in almost all realizations of bosonic optical lattice clocks [22, 74, 88–91] and this is also the method used for ^{24}Mg clock in this thesis.

2.5 A laser to probe the clock transition

In an ideal situation, the laser field used to probe the atomic transition should have a longer coherence time compared to the lifetime of excited state. The requirement on the probe laser eases a bit due to various decoherence mechanism

that act on the atomic transition. Nevertheless, atomic states can maintain their coherence for up to few seconds, which therefore means that lasers with sub-Hz linewidth are needed to efficiently probe these narrow atomic transitions. Since free running diode lasers typically have linewidths of the order of a few kHz at best, they need to be stabilized to another reference with an intermediate quality factor. This reference in most cases is a high finesse resonator, which is isolated from environmental perturbations. There can be other references such as narrow spectral hole burnt into absorption spectrum of materials [92] or fiber based resonators[93] as well. This section will be devoted to the ultrastable laser system used for the measurements in this thesis and this will be used as a basis for explaining various details and techniques which are ubiquitous in almost all ultrastable laser systems.

Before any details on the experimental setup, a discussion on characterizing clock instability is needed. All frequency standards estimate the unperturbed frequency of the reference system (which may be a quartz crystal, an atomic transition or any other frequency reference) ν_0 by the measured value ν . Since the reference system is always influenced by its environment, this leads to systematic frequency shifts ν_{syst} of the measured frequency from the true unperturbed frequency. Additionally, since the measurement process itself will at best of times introduce some noise, this adds a statistical frequency shift ν_{stat} to the measured frequency ν . Therefore the measured frequency value will be

$$\nu = \nu_0 + \nu_{\text{syst}} + \nu_{\text{stat}}. \quad (2.40)$$

The uncertainties associated with ν_{syst} form the error budget of an atomic clock system. Now to compare the performances of different frequency references, it is not convenient to directly compare the $\Delta\nu = \nu - \nu_0$ for different systems, but instead to look at the relative frequency error, $y = \Delta\nu/\nu_0$. Systematic error is typically estimated by measuring the dependence of ν on the perturbing parameter (such as magnetic field, laser intensity, or environment temperature). This is then used to estimate the total frequency shift at the operating value of that parameter. The associated measurement uncertainty contributes to the error budget for the frequency measurement. Assuming that each of the systematic shift contributions are independent from each other, the total systematic uncertainty therefore is given as

$$\sigma_{\text{syst}} = \sqrt{\sum_{n=1}^N \sigma_n^2} \quad (2.41)$$

where σ_n is the uncertainty contribution coming from each individual parameter n .

However the final measurement of the reference frequency (and measurements of all of the systematic shifts) are affected by the statistical measurement error, ν_{stat} ,

which typically (depending on the type of statistical noise) decreases as more measurements are averaged. Understanding how to mathematically describe statistical error is important for evaluating the final clock performance and for studying various noise processes affecting frequency standards. These methods are also relevant for evaluating the performance of ultrastable lasers and their suitability in optical clocks.

The fractional frequency deviation $y(t)$ for any frequency standard is a continuous process in time, but the measurement of this continuous function in practice gives a consecutive series of discrete values y_i

$$y_i = \frac{1}{\tau} \int_{t_i}^{t_i+\tau} y(t) dt \quad (2.42)$$

If these frequency fluctuations come from a stationary statistical process, the probability distribution for $p(y_i)$ follows a Gaussian distribution, fully characterized by the mean value and the standard deviation of this distribution. However, for non-stationary noise processes with correlations, just the mean and standard deviation of a data series fail in providing a complete picture. Therefore a better way of describing such processes is necessary, and one such quantity is Allan Variance, or the two-sample variance

$$\sigma_y^2(\tau) = \frac{1}{2} \langle (y_{i+1} - y_i)^2 \rangle. \quad (2.43)$$

The power spectral density $S_y(f)$ is another way of characterizing the noise in Fourier frequency domain

$$S_y(f) = \frac{1}{\nu_0^2} \mathcal{F}^* \left(\lim_{T \rightarrow \infty} \frac{1}{2T} \int_{-T}^T \Delta\nu(t + \tau) \Delta\nu(t) dt \right), \quad (2.44)$$

where \mathcal{F}^* is the inverse Fourier transform. Power spectral density (PSD) is a more comprehensive way of describing the noise processes compared to the Allan variance, and in fact Allan variance can be directly calculated from the power spectral density

$$\sigma_y^2(\tau) = 2 \int_{-\infty}^{\infty} S_y(f) \frac{\sin^4(\pi\tau f)}{(\pi\tau f)^2} df, \quad (2.45)$$

but a direct transformation in the opposite direction is not possible. Since Allan variance provides a more intuitive picture of the noise process in time domain, it is usually the preferred choice for characterizing frequency fluctuations. Most frequency standards can be modeled very well by a rather simple superposition of noise terms following power law behavior[94]

$$S_y(f) \approx \sum_{\alpha=-2}^2 h_\alpha f^\alpha, \quad (2.46)$$

α	Noise type	Allan variance
-2	Random walk of frequency noise	$\sim \tau^{+1}$
-1	Flicker frequency noise	$\sim \tau^0$
0	White frequency noise	$\sim \tau^{-1}$
+1	Flicker phase noise	$\sim \tau^{-2}$
+2	White phase noise	$\sim \tau^{-2}$

Table 2.1: Different noise components in Eq. 2.46, and their corresponding Allan deviation behavior.

and therefore these five noise terms provide the easiest way of understanding the behavior of frequency fluctuations. In Table 2.1, the time dependence of Allan Variance is given for all these five noise processes.

At low Fourier frequencies, typically random walk of frequency noise dominates the other noise contributions, whereas at very high Fourier frequencies, the white phase noise becomes the dominant term. For the Fourier frequencies in between these extremes, the other three terms dominate depending on their strength h_α and the Fourier frequency. And as can be seen from the Table 2.1, the Allan variance typically decreases for smaller averaging times as $1/\tau^2$ or $1/\tau$, whereas for longer time scales, there is typically a rise in Allan variance as τ .

Different noise terms also typically indicate contribution of different noise sources. For example, random walk of frequency noise typically arises due to environmental perturbations such as temperature and vibration, whereas the flicker frequency noise could be due to Brownian noise in resonator cavities.

For a diode laser, the PSD typically is flicker frequency noise upto a certain cutoff frequency, beyond which it follows the white frequency noise behavior. Depending on the PSD at the cutoff frequency, the spectral lineshape follows a Gaussian or a Lorentzian profile[95] with linewidth in the range of 10 kHz to few hundreds of kHz (depending on measurement duration). To enable clock spectroscopy, such a diode laser is typically locked to a Fabry-Perot resonator. Since a Fabry-Perot cavity only allows certain frequency modes $\nu_q = qc/2L$ depending on the length L of the cavity, the laser frequency is in effect locked to the length of cavity such that the frequency fluctuation depend on the length fluctuation of the resonator

$$\frac{\Delta\nu}{\nu} = -\frac{\Delta L}{L} \quad (2.47)$$

The laser frequency is stabilized to the resonator using Pound-Drever-Hall technique [96], where the error signal is inversely proportional to the full width at half

maximum (FWHM) of the resonance linewidth, $\Delta_{1/2}$ of the Fabry Perot cavity:

$$\epsilon(\Delta f) \sim -\frac{\Delta f}{\Delta_{1/2}}. \quad (2.48)$$

This immediately shows that a small $\Delta_{1/2}$ leads to a steep error signal slope. Since $\Delta_{1/2}$ depends on the finesse \mathcal{F} of the cavity as

$$\Delta_{1/2} = \frac{c}{2L\mathcal{F}}, \quad (2.49)$$

one needs to make optical cavities with very high finesse to achieve large error signal slope. For our ultrastable laser system, the resonator has a finesse of 600,000 for light at 916 nm and length of 10 cm, which gives a cavity resonance with $\Delta_{1/2} = 2.5$ kHz linewidth. With such a narrow resonance feature, it is possible to stabilize the laser frequency to sub-Hz linewidth. However, as can be understood from Eq. 2.47, the frequency stability depends directly on the length stability of the resonator. To suppress thermally induced length changes, the resonator is made out of an ultra low expansion (ULE) glass as can be seen in Fig. 2.9. This kind of glass is known for its low thermal expansion coefficient (± 30 ppb/ $^{\circ}\text{C}$). To further reduce the length fluctuations, temperature fluctuations affecting the

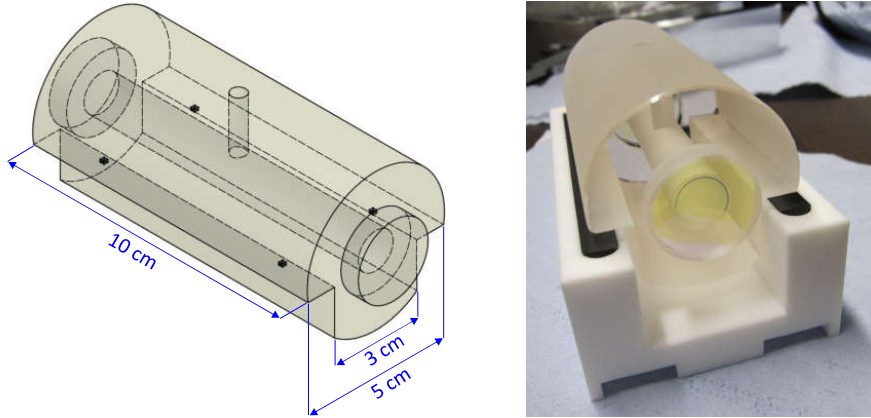


Figure 2.9: Schematic (Left) and picture (Right) of the ultrastable resonator system used in the magnesium lattice clock experiment[97]

resonator is decreased by surrounding it with a layer of passive thermal shield. This shielding is made of gold plated polished Aluminum, which acts as a low pass filter to any temperature variations in the outside environment. This whole system is then placed inside a vacuum chamber, whose temperature is actively stabilized to further reduce the temperature fluctuations acting on the resonator. Besides suppressing the influence of refractive index changes, the vacuum chamber is needed to reduce the convective thermal contact between the resonator system and the outer environment. The thermal shields are chosen to have high thermal conduction, which helps to maintain a uniform temperature distribution over the shields.

The other big challenge for maintaining length stability of this resonator at such remarkable levels is vibrations. To mount the resonator, it needs to be in contact with the base plate or the optical table at more than one support point. Therefore, vibrations can exert a differential force on the resonator through these support points, modifying the optical length of the cavity. To avoid this, the resonator is placed on four symmetric support points using viton balls to dampen the vibration coupling. There are more advanced mounting strategies that can further reduce the vibration sensitivity of the resonator length [98]. In case of our resonator setup, frequency sensitivity to acceleration was measured to be (27.3, 9.7, 4.9) kHz/(m/s²). To further attenuate the vibrations acting on the system, the setup is placed on top of an active vibration isolation stage, which is placed on another passive isolation table.

Having taken care for these technical noise sources acting on the resonator, one encounters the more fundamental noise that limits the length stability of the resonator: Brownian noise. At non-zero temperature, there will always be microscopic fluctuation in any material, which is called Brownian motion. This motion in the ULE spacer, mirror substrate as well as mirror coating leads to length fluctuations that depend solely on the material properties and the temperature of the system. This kind of noise appears as flicker frequency noise and therefore in the Allan deviation plot gives rise to a constant noise floor which cannot be surpassed regardless of averaging time. The biggest contributors to the Brownian noise are the mirror coating and the mirror substrate. Fused silica substrates have much lower Brownian noise compared to ULE glass substrates. Therefore, in our resonator setup, fused silica substrates were used even though this negatively influences the thermal expansion coefficient of the resonator. For the resonator system used in our experiments, this thermal noise floor arising from the Brownian noise is 3×10^{-16} in Allan deviation of fractional frequency fluctuations. This noise term can be further reduced by changing the mirror coating from the amorphous material layers used in our experiment to crystalline coatings [18].

In addition to these dominant noise terms, there are additional noise contributions such as residual amplitude modulation (RAM), intensity fluctuation noise, and noise coming from vacuum pressure fluctuations. More details on all these noise contributions can be found in the PhD thesis from Andre Papé [97] and Steffen Rühmann [99]. These laser systems reach frequency instabilities of such low levels that they are sensitive to even the path length fluctuations due to the air's refractive index fluctuations. Since there are not many frequency standards that have such incredible frequency stability, the best way of characterizing them is by comparing them with another identical system. Therefore two identical resonator systems were constructed, which were compared against each other to estimate their performance by assuming equal noise contribution from each ultrastable laser

system. In our case, the instability at 1 second was 4×10^{-16} , while the performance at longer time scales was limited by frequency drift of the order of few Hz/s due to residual temperature fluctuations affecting the system [99]. This frequency drift influenced the spectroscopy measurements as will be seen in the later chapters. Nevertheless, the instability at 1 second of 4×10^{-16} translates to sub-Hz linewidth, which therefore can be used to effectively probe optical clock transition.

Now that all the tools needed for performing spectroscopy of the atomic clock transition have been discussed, the locking of the spectroscopy laser to the clock transition can be discussed. Assuming a symmetric spectroscopy feature $f(\nu)$, the error signal can be obtained by taking the derivative of this spectroscopy feature

$$\mathcal{L}(\nu) \sim \frac{f(\nu + \Delta\nu) - f(\nu - \Delta\nu)}{2\Delta\nu}, \quad (2.50)$$

from measurements at frequency ν and $\nu + \Delta\nu$, which gives an anti-symmetric signal around the resonance condition. Using this approach, assuming a Gaussian spectroscopy lineshape, one can calculate the error signal $\mathcal{L}(\nu)$, which is shown in Fig. 2.10 (a). As can be seen here, the slope of the error signal becomes larger as the step frequency $\Delta\nu$ is lowered. This can be quantitatively seen in Fig. 2.10 (b) as well, where a saturation in the slope is also visible below a certain step frequency. Therefore, one would expect the ideal step frequency to be as small as possible to have a large error signal slope.

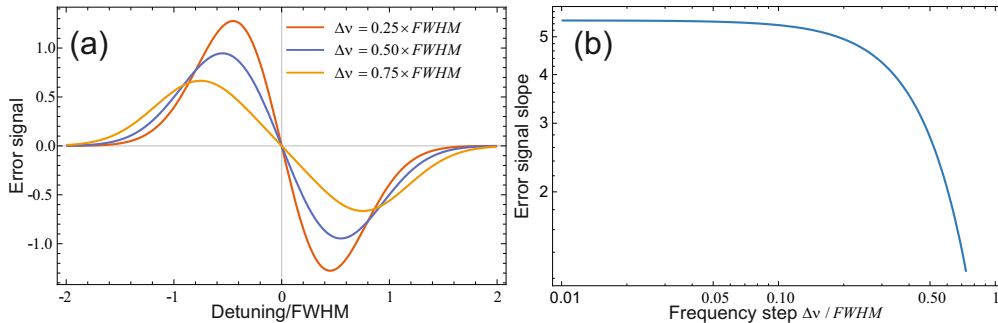


Figure 2.10: (a) The error signal for different values of step frequencies $\Delta\nu$, (b) Slope of the error signal near the resonance condition plotted as a function of the step frequency $\Delta\nu$

However, in a real world scenario, there is always additional noise on top of the measured spectroscopic signal, which could be due to the quantum projection noise, noise of the spectroscopy laser or the detection noise. This therefore distorts the generated error signal as well, as can be seen in Fig. 2.11 (a). It is also clearly visible that the error signal is more affected by the noise for smaller step frequencies, as shown in Fig. 2.11 (b). Therefore, a balancing act between high error signal slope and low sensitivity to noise is required. Typically for clock experiments, the step frequency is chosen to be $\Delta\nu = \Delta_{1/2}/2$, which gives a large error signal slope with a small sensitivity to noise in error signal.

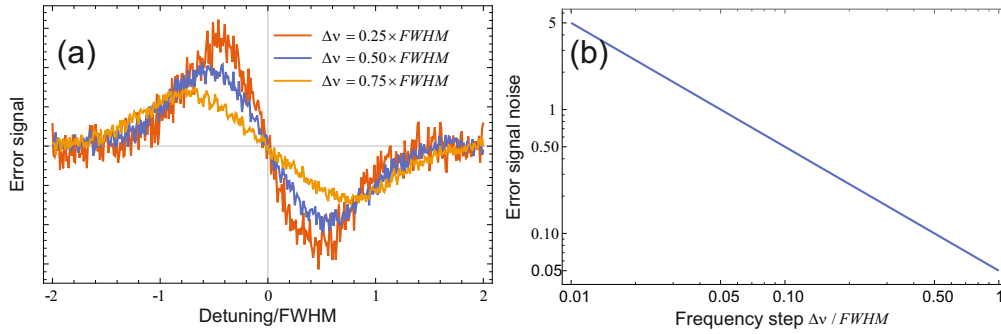


Figure 2.11: (a) The error signal for different values of step frequency $\Delta\nu$, where an additional random noise with $\sigma = 0.05$ has been added to the Gaussian spectrum. (b) The standard deviation of the noise seen on the error signal as a function of step frequency.

Therefore, by probing the clock transition on either side of the resonance, a reliable error signal is generated, which is used to steer the laser frequency to stay in resonance with the clock transition frequency. This laser light, which is locked to the atomic transition frequency can then be used as an optical frequency standard.

2.6 Measuring optical frequencies

Once the clock laser is locked to the atomic transition, the laser frequency can be used to generate a time standard with incredibly low instability and uncertainty achieved by using an optical atomic transition. But how can one do that, since there are no direct methods to count optical frequencies? On the other hand, radio frequency (RF) and microwave frequencies can be easily counted by electronic counters with the same precision and uncertainty as their reference clock frequency. Just to be clear here, the idea of measuring or counting a frequency is always a relative one: a frequency can only be measured in reference to another frequency. This is because as soon as a statement is made that the frequency of some standard is ν Hz, one assumes a meaning of what 1 Hz means in reference to another standard. So far, that reference frequency standard is the ground state hyperfine transition frequency of ^{133}Cs . Therefore any other frequency standard needs to be measured with respect to this frequency. Therefore the same needs to be done for measuring optical frequencies, or in case an optical frequency needs to act as a frequency standard, the counters need to be referenced to the optical frequency standard. This is where frequency combs play a crucial role. An introduction to the frequency comb has already been given in the last chapter, therefore the aim here will be to look more into the technical details. The main objective of a frequency comb is to bridge the gap between RF frequency and the optical frequency standards, and between different optical frequency standards as well.

The simplest frequency comb is based on a mode locked laser, where as is well known for such lasers, a pulse train with a nearly constant repetition rate f_{rep} is generated [100]. The spectrum of such a pulse train is also a sum of discrete frequency modes f_n which form the teeth of a frequency comb:

$$f_n = f_{\text{CEO}} + n f_{\text{rep}} \quad (2.51)$$

The repetition rate f_{rep} can be easily measured using a fast photodiode and it depends on the length of the laser resonator. Therefore it can be tuned using piezo actuators. On the other hand, the carrier envelope offset (CEO) frequency f_{CEO} which results from a mismatch of the phase and group velocity is not so easy to determine. However, if somehow the spectrum of the frequency comb can be stretched beyond one octave, then a heterodyne beat can be generated between frequencies f_{2n} and the second harmonic of f_n

$$\begin{aligned} f_b &= 2f_n - f_{2n} \\ &= 2f_{\text{CEO}} + 2n f_{\text{rep}} - (f_{\text{CEO}} + 2n f_{\text{rep}}) \\ &= f_{\text{CEO}} \end{aligned} \quad (2.52)$$

This was the big breakthrough in practical application of optical frequency combs. Once CEO frequency can be measured, it is possible to stabilize it by acting on the intracavity power by one of several possible methods [101]. For stretching the frequency spectrum to beyond an octave, super-continuum generation in photonic crystal fibers (PCF) is the most commonly used method [5, 6, 102].

Once f_{rep} and f_{CEO} have been stabilized to a microwave frequency standard, all the comb lines are referenced to the same microwave standard. Now heterodyne beat-note between one of these comb lines and the optical frequency standard of interest can measure the optical frequency in reference to the microwave frequency. Importantly, the whole process can be reversed as well, where the frequency comb can be referenced to an optical frequency standard, and the f_{rep} also acts as a frequency reference with same instability and accuracy as the optical reference [103, 104]. This allows to use optical frequency standard as a clock.

2.7 Optical trapping and manipulation of ^{24}Mg

Thus far, every step required to develop an optical lattice clock has been discussed with Magnesium as an example. In this section, the cooling and trapping scheme for Magnesium will be discussed, which in some parts is very typical of most lattice clock elements and in some parts is rather unique to Magnesium.

A cold Magnesium sample is required to be able to load enough atoms into the optical lattice. The most straightforward way to cool and trap magnesium is in

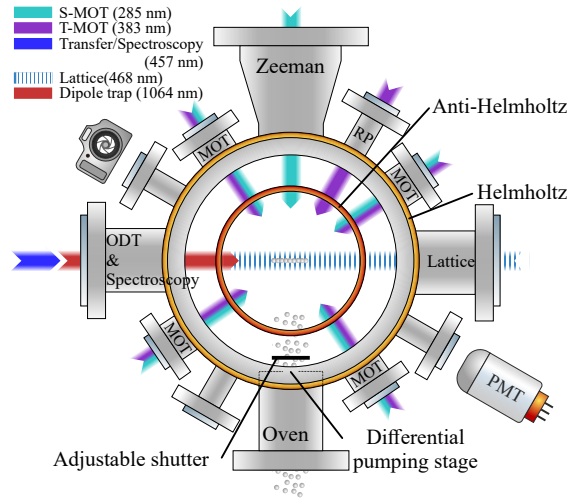


Figure 2.12: The schematic of magnesium lattice clock experimental setup[78].

a magneto optical trap (MOT) on the $^1\text{S}_0 - ^1\text{P}_1$ transition. As can be seen in Fig. 2.12, thermal atoms emanating from an oven where magnesium shards are heated to 450°C are first slowed using a Zeeman slower and trapped in the Singlet-MOT using 285 nm light. Due to a rather large linewidth of this transition, the Doppler temperature is limited to 3 mK, which is too large to obtain sufficient transfer to the lattice. This is typical of optical lattice clock elements, where the first stage Singlet-MOT is operated on this broad transition. However, unlike other lattice clock elements where a second stage cooling can be realized on the narrow intercombination transition $^1\text{S}_0 - ^3\text{P}_1$, such an approach is not possible in Magnesium due to incredibly small linewidth of only 36 Hz for this transition. Therefore, for Magnesium a second stage MOT can only be realized on either $^3\text{P}_2 - ^3\text{D}_3$, or $^3\text{P}_0 - ^3\text{S}_1$ transition. Both these transitions require additional re-pumpers due to optical decay to other states. For our experiment, the $^3\text{P}_2 - ^3\text{D}_3$ transition is used as the second stage Triplet-MOT. The Doppler temperature for this state is about 1 mK. Ideally, atoms would be transferred from this second stage MOT to the optical lattice. However, the optical lattice at 468 nm was observed to ionize atoms in ^3D state. Therefore, a far off resonance optical dipole trap is used as an intermediate step to transfer atoms from the two-stage MOT to the optical lattice. It was further observed that the atom collection efficiency in the dipole trap was much higher in the so called continuous loading scheme, compared to a step-wise approach [105]. In this continuous loading scheme, both the Singlet-MOT and the Triplet-MOT are simultaneously running, while the 1064 nm dipole trap is overlapped with the Triplet-MOT atomic cloud. To open a loss channel from the Triplet-MOT to the dipole trap, the re-pump laser acting on the $^3\text{P}_0 - ^3\text{D}_1$ transition is off. Therefore, the atoms decaying down to $^3\text{P}_0$ are captured by the dipole trap, provided they have cooled down sufficiently. In a 50 W dipole

trap with waist of about 45 μm , typically about 10^5 atoms are trapped at 100 μK . These atoms are optically pumped to $^1\text{S}_0$ state by excitation to $^3\text{D}_1$ state, from which atoms can decay to $^3\text{P}_1$, followed by spontaneous decay to the ground state. These atoms are then transferred to the optical lattice, which is spatially overlapped with the 1064 nm optical dipole trap, where they are probed using the spectroscopy laser, which is also overlapped with the optical lattice. After the spectroscopy pulse excites a fraction of the atoms to the excited state, all the atoms including the remaining atoms in ground state are transferred back to the 1064 nm dipole trap. Then the fluorescence from the T-MOT is used to detect the number of excited state atoms. Afterwards, the remaining ground state atoms are excited to the $^3\text{P}_1$ state by a resonant optical excitation, and they are also detected in the T-MOT to determine the ground state atom numbers. This allows for the determination of excitation fraction, which improves the signal to noise ratio by correcting for the atom number fluctuations.

2.7.1 Laser systems used for trapping the atoms

To be able to cool, trap and probe magnesium atoms, lasers with wavelengths ranging from 285 nm to 1064 nm, powers ranging from few mW to few tens of Watts and laser linewidths from few MHz down to sub-Hz regime are used. Here we sequentially detail all the laser systems needed for the experiment.

S-MOT laser at 285 nm

For the first stage MOT, laser light of 285 nm wavelength is required. This is generated by second harmonic generation (SHG) from light at 570 nm. This light field is generated by a commercial system consisting of a diode laser at 1140 nm, which is then amplified by a Raman fiber amplifier to up to 3 W. This is then frequency doubled in a bow-tie SHG cavity to 570 nm giving up to 1 W optical power. To generate UV light from this field, a bow-tie resonant cavity is used, where the nonlinear conversion occurs in a Beta-Barium-Borate (BBO) crystal. To reduce the power degradation from UV light, a small constant flow of Oxygen is maintained through the SHG setup. Up to 200 mW of 285 nm light can be generated, though typical operation is maintained at around 100 mW to slow the degradation of SHG power.

To maintain correct frequency with respect to the atomic transition, the laser frequency is stabilized to the R115(20-1) iodine transition. A fraction of the 570 nm light is used to perform Doppler free frequency modulation spectroscopy, where the dispersive error signal is generated using lock-in technique.

T-MOT lasers at 383 nm

Though the triplet MOT transition $^3\text{P}_2 - ^3\text{D}_3$ for magnesium is a closed transition, non-resonant excitation to the $^3\text{D}_1$ state still occurs due to large linewidth of the transition. Therefore additional re-pumper lasers are required besides the MOT laser. This increases the overall complexity of this laser system. Three independent identical laser systems are used to excite the MOT and the re-pumper transitions ($^3\text{P}_0 - ^3\text{D}_1$ and $^3\text{P}_1 - ^3\text{D}_2$). All the lasers are frequency doubled master oscillator power amplifier (MOPA) laser systems, where light from a diode laser at 767 nm is amplified using a tapered amplifier to 1.5 W, which is then frequency doubled in bow-tie design resonant enhancement cavities using Lithium Triborate (LBO) crystals as the nonlinear medium.

Frequency stabilization for these lasers follows a slightly more complicated mechanism. The fundamental laser wavelength of 767 nm makes Potassium spectroscopy an ideal candidate for frequency stabilization. To achieve this for all three MOT lasers, another laser is used, which is first stabilized to a transfer cavity, and then used for performing Doppler free saturation spectroscopy where the feedback acts on the piezo attached to one end mirror of this transfer cavity. This ensures that the transfer cavity length has the long term stability of the Potassium atomic spectroscopy. Afterwards, all the three MOT and re-pumper lasers are locked to the transfer cavity, whereby locking these lasers to the ^{39}K atomic reference.

Transfer laser at 457 nm

To effectively transfer atoms from ground state to the triplet manifold, excitation on the $^1\text{S}_0 - ^3\text{P}_1$ transition at 457 nm is utilized. Since this is a very narrow transition with natural linewidth of only 36 Hz, the transfer laser also requires high spectral purity. The laser system consists of a 914 nm diode laser, which is amplified in a tapered amplifier and then frequency doubled in a bow-tie SHG enhancement cavity. A fraction of this 457 nm light is sent to a 10 cm long ULE glass resonator, where it is stabilized to one of the TEM00 resonance modes. This ULE glass resonator is placed inside a vacuum chamber, which is suspended from the ceiling to suppress high frequency vibrations. This laser stabilization achieves linewidth of around 100 Hz. Most of the light coming out of the SHG is delivered to the spectroscopy setup after frequency shifting using an acousto-optic modulator (AOM). This light is then superposed with the optical lattice axis to have a high efficiency of excitation in the lattice.

Dipole laser at 1064 nm

Since spectral properties are not so important for a far off resonance optical dipole trap, we use a 1064 nm Yb-fiber laser system, which can deliver up to 50 W of light power with a spectral linewidth of about 0.2 nm. This laser beam is focused to a waist of about 45 microns at the MOT position in the middle of the vacuum chamber. This provides a trap depth of about $150\mu\text{K}$, which filters out the hottest atoms from the trap and retains atomic sample with effective temperature of about $100\mu\text{K}$. The dipole trap is also aligned along the optical lattice beam for maximum transfer efficiency to the lattice.

Optical lattice at 468 nm

This is perhaps the most critical laser system of all, requiring large optical powers at the position of atoms, at a wavelength that is not most conducive for such high power generation. Therefore, an enhancement cavity is needed to significantly increase the lattice light intensity. The first step is a titanium sapphire (Ti:Sa) laser operating at 936 nm, which is in turn pumped by a 18 W Optically Pumped Semiconductor Laser (OPSL) at 532 nm. The output from the Ti:Sa is approximately 1.5 W, which is then frequency doubled in a commercial SHG setup using Periodically Poled Potassium Titanyl Phosphate (PPKTP) crystal, which has good efficiency at this wavelength. About 550 mW output at 468 nm is achieved from this setup. This light is then passed through an AOM in zeroth order to stabilize lattice intensity, and transferred via a large mode field area fiber to the enhancement cavity setup. The enhancement cavity is built in a folded design that goes around the vacuum chamber where the vacuum windows are coated for low losses at the design wavelength. The mirror radius of curvatures are chosen such that the cavity is in a concentric cavity regime and the waist of the cavity mode (typically around $50 - 80 \mu\text{m}$) falls at the center of the chamber. There are additional intracavity elements to couple the 1064 nm dipole laser light and 458 nm clock laser light. All the optics is coated for maximum transmission possible at 468 nm. The light power at the input of the cavity is around 350 mW, which in the cavity, this is amplified to as high as 10 W circulating power. More details on the lattice setup will be discussed in the later chapters. To stabilize the lattice frequency during the measurements, a transfer cavity is used where the transfer cavity length is stabilized to the clock laser frequency while the TiSa laser frequency is then stabilized to the transfer cavity using feedback on the TiSa cavity resonator length [106]. The lattice frequency is monitored using a wavemeter with an accuracy of 30 MHz.

Clock laser at 458 nm

Most details on stabilizing the clock laser to ultrastable resonator has already been discussed in Section 2.5. Here the discussion therefore will only briefly focus on the optical setup. The laser system itself consists of a 916 nm diode laser amplified using a tapered amplifier. This laser is stabilized to an ultrastable resonator as detailed in Section 2.5. The stabilized laser is transferred to the spectroscopy lab using a 30 m long fiber, where the fiber noise is actively compensated. This light is then amplified with another tapered amplifier and frequency doubled in a resonant cavity giving typically about 100 mW light power at 458 nm. This is then transferred to the spectroscopy setup after passing through an AOM, using another short optical fiber. The clock laser is then aligned to the optical lattice using small alignment apertures on either side of the vacuum chamber. Typical misalignment is below 1 mrad. A small fraction of the clock laser is reflected back from one of the end mirrors of the lattice cavity and is returned through the optical fiber to create a heterodyne beat with the light immediately after the SHG. This beat signal contains the noise introduced by the light transfer system, and using the AOM mentioned above, the phase of the clock laser at the lattice cavity end mirror can be actively stabilized.

2.7.2 Vacuum chamber and Magnetic fields setup

The heart of the experiment is the vacuum chamber where atoms are trapped. This is schematically shown in Fig. 2.12. This chamber is connected directly to the source chamber where solid magnesium is heated to 450 °C, at which point, they sublime and eject through a small aperture of 5 mm diameter into the science chamber. The small aperture helps maintain a differential vacuum pressure between the two chambers, where the vapor pressure in source chamber is relatively high while the science chamber vacuum pressure is reduced to $1 - 2 \times 10^{-9}$ mbar. In between the source and science chamber, there is a shutter, which can be closed during the spectroscopy to shield cold atoms from the thermal atoms emanating from the source chamber. The science chamber is pumped by a combination of turbo pump and ion pump. Different CF flanges allow optical access to the center of the chamber. On the top and bottom of the chamber, there are two CF200 pot flanges, which allow a closer access to the chamber for the MOT coils.

Quadrupole magnetic field coils

Current carrying coils responsible for generating the quadrupole magnetic field for operating the MOTs are wound on the CF200 pot flanges(Fig. 2.12). The coils are water cooled to reduce the temperature inhomogeneity of the chamber, and are connected to a power supply, which can deliver up to 200 A current. The current is regulated using an insulated gate bipolar transistor (IGBT), which has a time constant of 30 μ s. However the decay time of magnetic field is around 2 ms due to the eddy currents generated in the steel chamber. For the 200 A current used for the MOT operation, magnetic field gradients of 1.3 T/m and 0.65 T/m are generated along the strong and weak axes respectively.

These MOT coils can also be used to generate homogeneous magnetic field where the current is switched from anti-Helmholtz to Helmholtz configuration by flipping the current direction in lower coil using additional IGBTs. This magnetic field was typically used for performing the lattice sideband spectroscopy, or to probe the carrier for low lattice depths where the Rabi frequency becomes much too small. This coil can generate around 2.49 G/A magnetic field, which was determined by measuring the $^1S_0 - ^3P_1$ Zeeman splitting as a function of coil current.

Homogeneous magnetic field coils

While the magnetic field generated from MOT coils in Helmholtz configuration is homogeneous in the central region of the chamber, the magnetic field shows inhomogeneities within a few mm from the trap center. This is not ideal for the lattice clock where atom cloud is distributed over several millimeters in the lattice [78]. This magnetic field inhomogeneity results from the relatively small diameter of MOT coils and a small distance from the center of the chamber. Therefore, to probe atoms with a more homogeneous magnetic field, an additional pair of coils with larger diameter is installed around the vacuum chamber. Due to heating in the coils, a maximum current of 15 A is possible in these coils. To stabilize the current in these coils, it is measured using a precise current sensor¹, where the primary current is converted to a secondary current with a ratio of 1 : 1750. To improve the sensitivity factor, the primary current carrying wire is implemented with 20 winding across this sensor. The secondary current thus generated is measured as a voltage drop across a passively cooled high precision resistor², which is then amplified and used to generate an error signal to stabilize the current using a MOSFET.

¹IT 700-S Ultrastab from LEM

²VCS332Z from Vishay

Stray field compensation coils

Besides the applied fields, there are additional magnetic fields affecting the atoms. These fields can result from the earth's magnetic field or from the surrounding magnetic materials, or more generally through a combination of both. Since a high degree of magnetic field control is required to operate a lattice clock, these stray magnetic fields are compensated. For this purpose, three orthogonal pairs of current carrying coils are implemented, which are calibrated using Zeeman spectroscopy of the $^1\text{S}_0 - ^3\text{P}_1$ transition to compensate the external fields.

Characterizing line-broadening in an optical lattice

Optical lattices are invaluable for performing spectroscopy of neutral atoms in the Lamb-Dicke regime. As discussed in the previous chapter, with a deep enough optical lattice, atomic motion can be very well approximated as in a strongly confining harmonic oscillator potential with negligible Doppler and recoil frequency shifts. However, precise optical spectroscopy also allows for studying interesting physics of atomic motion in an optical lattice in different regimes. While the deep lattice regime leads to harmonic oscillator like motion, the shallow lattice regime has a more complex behavior, which can be best understood using the formalism of Bloch bands. In addition to being of interest to fundamental Physics, a detailed characterization of optical lattice also allows us to better understand associated line-broadening and frequency shifts relevant for our optical lattice clock. This chapter will therefore be devoted towards a detailed characterization of clock spectroscopy with respect to variation in lattice depths, lattice frequency and atomic temperature.

3.1 Not so deep in the Lamb-Dicke regime

The Lamb-Dicke regime has no sharp barrier. Instead, it is reached, when the trap frequency becomes much larger than the photon recoil frequency. It is therefore interesting to understand what happens as the system gradually moves deeper

into the Lamb-Dicke regime. A transition to the Lamb-Dicke regime is in many ways similar to the transition across the classical to quantum regime boundary. Moving deeper into the Lamb-Dicke regime can also be seen as moving deeper into the quantum regime. Therefore, the transition to the Lamb-Dicke regime is also interesting from the view of fundamental physics.

In the analysis of the Lamb-Dicke regime, it is also important to understand the role of spontaneous emission. The Lamb-Dicke regime was studied initially to deal with the Doppler and recoil frequency shifts associated with the spontaneous emission. Since optical clock states have a low spontaneous emission rate, one can argue that the constraints of the Lamb-Dicke regime do not need to be strictly followed for Doppler- and recoil-free spectroscopy. In principle, as soon as the trap frequency becomes larger than the recoil frequency, we enter into the resolved sideband regime, where the influence of photon recoil can be avoided, if the spectroscopy laser is precise enough to resolve the sidebands. Indeed, the relative strength of the carrier with respect to the sidebands would be lower, but as long as these sidebands can be resolved (which is relatively easy since there is no spontaneous emission induced line-broadening), the photon recoil shift should not directly affect the measurement.

However, the influence of atomic motion and photon recoil is still present in the carrier lineshape, at least for the case of a lattice potential. For atoms trapped in an optical lattice, the energy bands are easily resolved with sideband resolved spectroscopy. However, these individual bands still have a continuous energy dispersion relation. These can show up in the lineshape of the carrier as well. The trapping potential of a typical 1D optical lattice is shown in Fig. 3.1(a). Optical lattice is generated by interference of two counter-propagating monochromatic laser beams, which leads to the formation of a standing wave. In the transverse axes, the Gaussian beam shape gives rise to a shallow trapping potential.

The energy of atomic states is perturbed by the Bloch band spectrum of the optical lattice and the Gaussian transverse potential (Fig. 3.1(c-e)). Since the clock laser is aligned with the optical lattice axis, the transverse energy spectrum does not directly lead to frequency shifts. However, the Bloch bands significantly modify the carrier lineshape. This happens because the photon recoil momentum absorbed during spectroscopy leads to a change in the atomic quasimomentum (following the momentum conservation rule), which leads to a frequency shift according to the dispersion relation for the Bloch band (Fig. 3.1(b)). Since this “recoil” frequency shift depends on the quasimomentum of the atoms, the total lineshape generated by atoms uniformly occupying all the quasimomenta is given by a double-peak lineshape as shown in Fig. 3.2. As the lattice depth is increased, moving deeper into Lamb-Dicke regime, the Bloch bands become flatter, leading to smaller frequency shifts due to the photon recoil. On the other hand, for shallow optical lattice, such

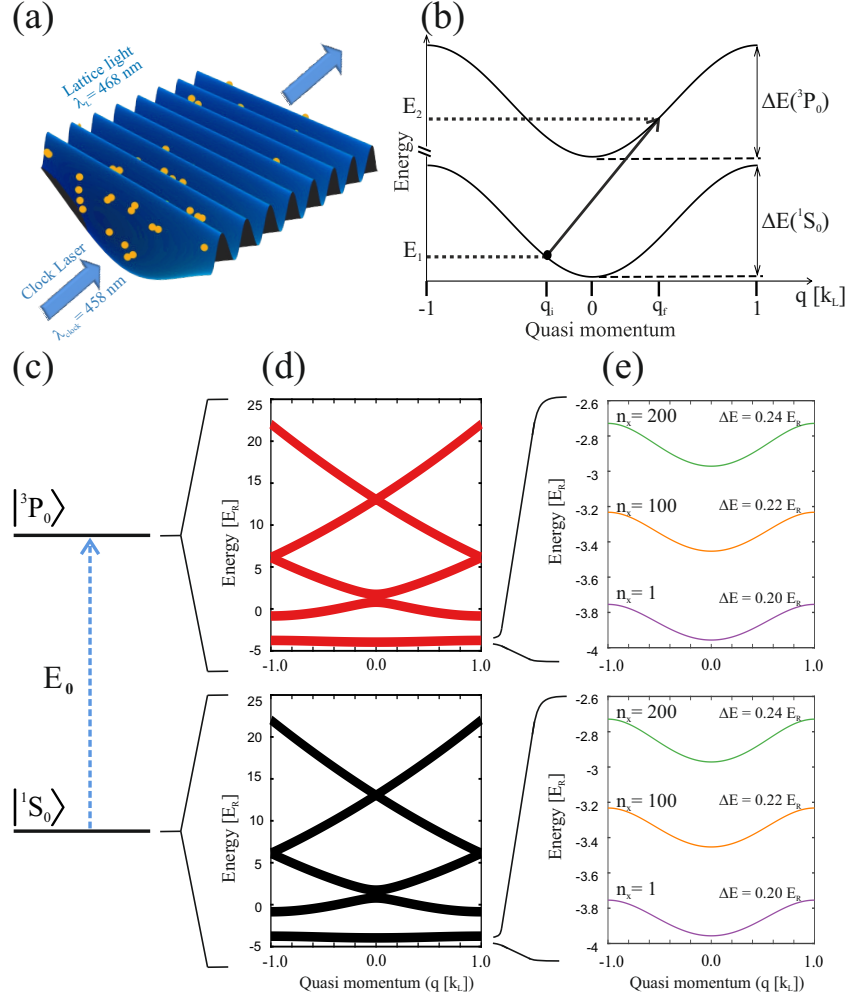


Figure 3.1: (a) Typical one dimensional lattice potential featuring standing wave pattern along the lattice axis with a Gaussian trapping potential in transverse axes. (b) In presence of an optical lattice, optical spectroscopy is modified by the Bloch band spectrum of the lattice. The modified dispersion relation gives rise to a frequency shift akin to photon recoil shift for freely moving atoms when an atom with initial quasimomentum q_i is excited to the 3P_0 state with quasimomentum q_f ($=q_i + k_{\text{clock}}$). The atomic states in (c) are modified by the Bloch band spectrum as shown in (d), with additional transverse states (e) coming from the Gaussian transverse potential for a $6.5 E_R$ deep lattice.

frequency shifts can be significant, leading to a distortion of the carrier lineshape.

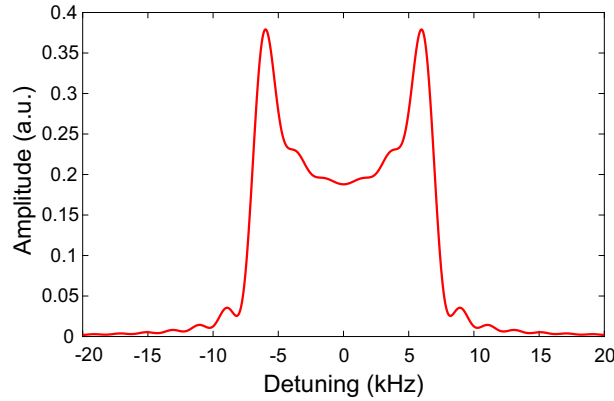


Figure 3.2: Carrier lineshape for a $6.5 E_R$ deep optical lattice. If the Rabi frequency is lower than the Bloch band width, a double peak structure is resolved in the lineshape. This double peak structure comes from the Van-Hove singularity of the density of states in the lowest Bloch band.

The density of states in a Bloch band is determined by the curvature of the band, which leads to the famous Van-Hove singularities at the center and edges of the band. As shown in Fig. 3.2, this leads to a double peaked modification of the carrier lineshape since atoms at the center and edges of Bloch band experience different frequency shifts. This lineshape distortion was proposed for the first time by Lemonde and Wolf [107] and observed for the first time in our group in 2015 [77].

While these lineshape distortions are not ideal for optical clocks and efforts are made to avoid them, it is also incredibly difficult for most optical clocks to precisely study these lineshape distortions. As can be seen in Fig. 3.2, where the lineshape is shown for the $6.5 E_R$ deep lattice potential of Fig. 3.1, the peak separation is approximately twice as large as the Bloch band width. Therefore, for deep lattices where the width of Bloch band is very narrow, it is incredibly hard to resolve the doublet feature. On the other hand, for a shallow lattice, the transverse trap is usually not strong enough to trap the atoms against the gravitational force. Therefore, for heavier lattice clock elements, additional transverse confinement is needed to be able to trap atoms in shallow lattice regime. For magnesium, due to the small atomic mass, trapping in a shallow lattice is still fairly efficient. Therefore, magnesium lattice clock is ideally suited to study the shallow lattice physics using optical spectroscopy.

The clock spectroscopy of Bloch bands has been experimentally [28, 77, 108] and theoretically [107, 109] studied. Since we know from these studies precisely the relationship between the peak separation in the Bloch band spectrum and the lattice depth, measurements of the Bloch band resolved spectrum can help us to characterize the optical lattice. We therefore numerically fit the measurement

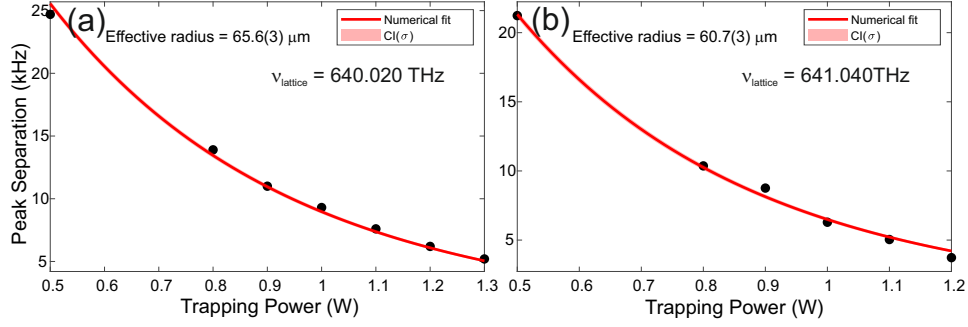


Figure 3.3: Peak separation vs lattice power at magic frequency 640.020 THz (a) and at 641.040 THz (b). The experimental data is fitted in both cases with the theoretical calculated peak separation with the lattice waist as the only free parameter.

data of peak separation in Bloch band doublets for different lattice powers with a numerical model estimating the Bloch bandwidth for a given lattice depth. This allows us to obtain the effective lattice beam radius at the position of atoms. We performed two such measurements, one near the magic frequency at 640.020 THz and another at 641.040 THz. In both cases the theoretical peak separation fits the data very well, as can be seen in Fig. 3.3

The numerical fitting to the peak separation data gives a fairly precise value of the effective beam radius of $65.6(3) \mu\text{m}$ and $60.7(3) \mu\text{m}$ for the two lattice frequencies of 640.020 THz and 641.040 THz respectively. In both cases, the measured lattice waist was smaller at $60.4(2.0) \mu\text{m}$ and $46.7(9) \mu\text{m}$ respectively. This emphasizes that although we have a precise measurement of lattice power and lattice waist, the actual trap depth experienced by the atoms may be different due to a mismatch of the lattice waist position and the atomic cloud position. Using these effective beam radius values, lattice waist position mismatch for the two measurement sets is estimated to be $10.4(1.6) \text{ mm}$ and $12.1(2) \text{ mm}$, with a weighted mean value of $11.9(1.2) \text{ mm}$. Since the lattice geometry was not significantly changed during the rest of the measurements in the thesis, this mismatch will always be used to calculate the effective lattice intensity at the position of atoms.

The large range of trap depth used for these measurements also allows us to show the transition of Bloch band spectrum from shallow lattice to deep lattice regime (Fig. 3.4). While the lineshapes in Fig. 3.4 are very similar to the lineshape shown in Fig. 3.2, it is important to note a slight smearing out of the doublet feature. We understand this deviation from a pure 1D calculation result to come from the radial state contributions. Indeed, the total lineshape can be considered as a sum of contribution from all the occupied radial states. The higher radial states have a lower effective lattice depth and therefore the associated Bloch band width is larger. Therefore higher radial states contribute doublets with larger peak spacing to the total lineshape. The resulting double peaked lineshape obtained from averaging

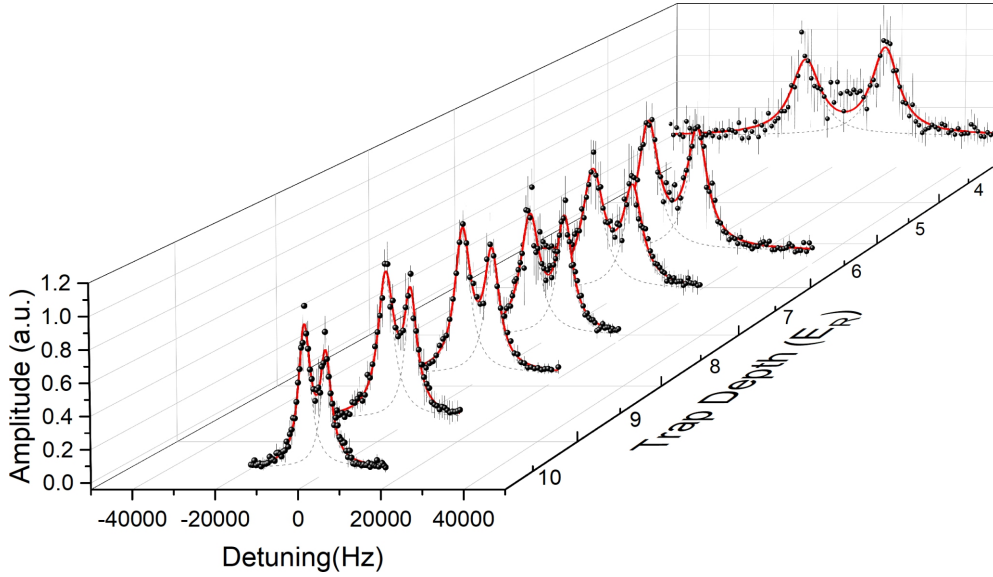


Figure 3.4: Evolution of the spectroscopy lineshape as a function of lattice depth for a magic lattice frequency. With increase in the lattice depth, the two peaks progressively merge with each other. The experimental data is fitted with a double-Lorentzian lineshape shown by red curve.

over all the radial states therefore smears out into a broader feature instead of the sharp peaks expected from the 1D model.

When the lattice frequency is varied, these radial states lead to another interesting feature. The doublet lineshape develops an asymmetry between the two peaks, as the lattice frequency deviates from the magic condition. This was observed first in our group in 2015 [77]. To study this inhomogeneity in detail, we now performed systematic measurements of the Bloch band lineshape at about 1 GHz detuning above magic frequency for different lattice depths. The resulting lineshape variation is shown in Fig. 3.5. The lineshape asymmetry is clearly visible here, which becomes more pronounced as the lattice depth is increased.

With a goal to better understand these lineshape asymmetries, a numerical model has been developed that includes the coupling of radial and axial dimensions. In Eq. 2.11, a complete Hamiltonian for the 1D lattice system is given. While approximating the total potential with a separable radial and axial potential works well in deep lattice regime, for the shallow lattice regime, the complete Hamiltonian needs to be considered. In particular, the terms which couple radial and axial potentials are very important. Since solving the Schrödinger equation for complete 3D potential presents a significant computational challenge, we only solve for a two dimensional model. Though this reduces the total impact of radial states in the calculations, the most important additional aspect of the lattice potential i.e. axial-radial coupling, is still included.

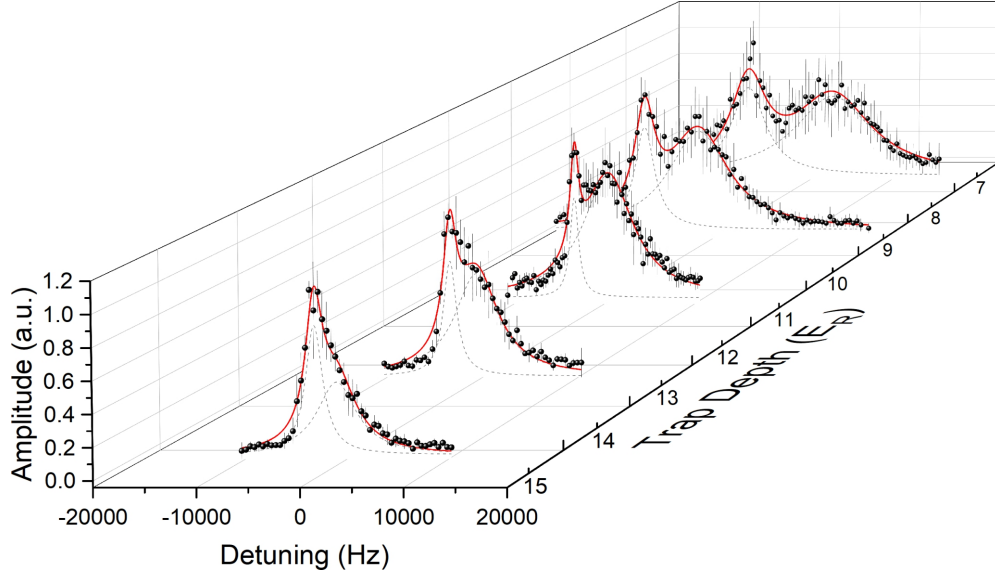


Figure 3.5: Evolution of the spectroscopy lineshape as a function of lattice depth for a lattice wavelength detuning of -0.74 nm from the magic wavelength. With increase in the lattice depth, the two peaks merge with each other. Also, the inhomogeneity of the lineshape increases as the trap depth is increased. The experimental data is fitted with a double-Lorentzian lineshape shown by red curve, where parameters of the two Lorentzian peaks can be used to parameterize the lineshape inhomogeneity.

To calculate the spectroscopy lineshape, first the energy spectrum is calculated by diagonalizing the Hamiltonian matrix generated for 1S_0 at a given initial quasimomentum value, q_i . A similar spectrum is calculated at the final quasimomentum $q_f = q_i + k_{\text{clock}}$ for the 3P_0 state. This provides all the transverse energy levels for the ground and excited atomic states. Therefore, at a given frequency of the spectroscopy laser, the transition probability between different transverse states can be calculated using the optical Bloch equation. The wavefunctions of these states are used to calculate the effective Rabi frequency between different transverse states. This becomes particularly important for the higher transverse states where transitions involving a change in the transverse state become significant. The total spectroscopy lineshape is then estimated by integrating the transition probability for different quasimomenta over the entire Brillouin zone. While calculating the excitation probability between different transverse states, a two-level model is assumed, which is a reasonable approximation for most cases where the spacing between transverse states is larger than Rabi frequency. This approximation may not hold perfectly for very high transverse states where energy spacing between neighboring transverse states becomes progressively smaller.

For efficiently calculating the Hamiltonian matrix, a suitable set of basis functions is needed. Along the axial direction, cosine wave basis (with periodicity being multiples of lattice periodicity) is chosen. For the transverse axis, harmonic oscillator

states are convenient basis states, due to similarity of these trapping potentials.

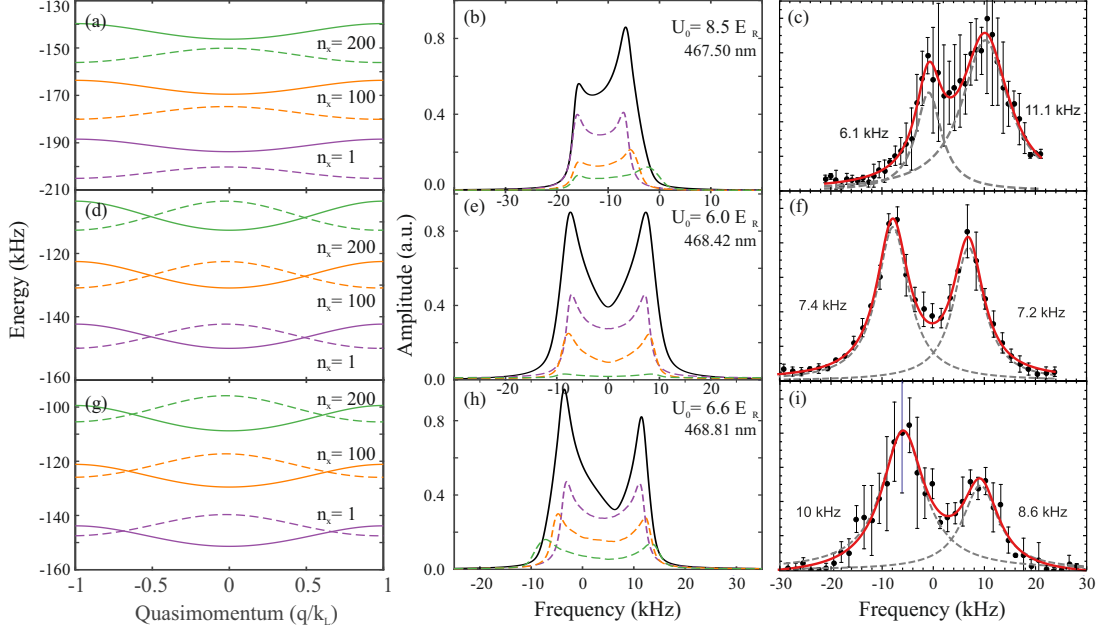


Figure 3.6: Lineshape asymmetry as a function of lattice wavelength is shown here. To understand the influence of transverse states, 1st (purple), 100th (orange) and 200th (green) transverse states are shown in (a), (d) and (g) for the three cases of lattice wavelength below, at, and above the magic wavelengths respectively. The energies for the 1S_0 state are shown by solid lines while the 3P_0 state is represented by dashed lines. The 3P_0 bands are shifted in quasimomentum by the spectroscopy laser wavevector, k_{clock} . The lineshapes calculated for these transverse states are shown in corresponding colors by the dashed lines in (b), (e), and (h), where they once again correspond to the cases of lattice wavelength below, at, and above magic wavelengths respectively. The total lineshape obtained by considering the 200 lowest transverse states are shown by the solid black curves. These numerical calculations are to be compared to the experimental data shown in (c), (f) and (i) for the three different lattice wavelengths, where red line is a double-Lorentzian fit to estimate the linewidth asymmetry.

With the help of these simulations, we can understand how the radial states lead to an asymmetry of the double-peak Bloch band lineshape, as the lattice wavelength moves away from magic condition. Fig. 3.6 (a,d,g) depict for three lattice wavelengths, the Bloch bands for atoms in the ground and excited state (solid and dashed line) occupying the 1st, 100th and 200th transverse state (purple, orange, green color) along with the corresponding theoretical line shapes in Fig. 3.6 (b,e,h) and compare them with the line shapes (Fig. 3.6 (c,f,i)) obtained in our previous measurements from 2015 [77]. The three scenarios consider lattices where the trapping potential for the 3P_0 state is deeper, equal or shallower than for the 1S_0 state, corresponding to a lattice wavelength below (Fig. 3.6 (a,b,c)), equal to (Fig. 3.6 (d,e,f)) or above (Fig. 3.6 (g,h,i)) the magic wavelength respectively.

For the case of the lattice being detuned below the magic wavelength (Fig. 3.6 (a,b,c)), one can see that the energy difference between the 1S_0 and 3P_0 states at the edges of the band (which forms the left peak in the spectroscopy lineshape) does

not vary for different transverse states, whereas the energy difference at the center of the band decreases as one goes to higher radial states. Therefore in the spectrum calculated from only 1st, 100th and 200th transverse state as shown in Fig. 3.6(b) with purple, orange and green curves, the left peak position does not change much while the right peak position shifts towards zero detuning for higher transverse states. The total lineshape thus obtained by considering the excitation from all 200 lowest transverse states leads to a broader right peak compared to the left peak, as shown in Fig. 3.6(b) with black curve. This behavior matches the experiments quite well, as shown in Fig. 3.6(c), where the right peak is almost twice as broad as the left peak. Another interesting feature in both the experimental results as well as theoretical curves is that the narrower peak has a smaller amplitude. This results from driving the transition into saturation with very long spectroscopy pulses such that the area under the two peaks is not equal anymore. When the lattice wavelength is detuned above the magic wavelength, similar arguments lead to asymmetries in the opposite direction as seen in Fig. 3.6(g-i).

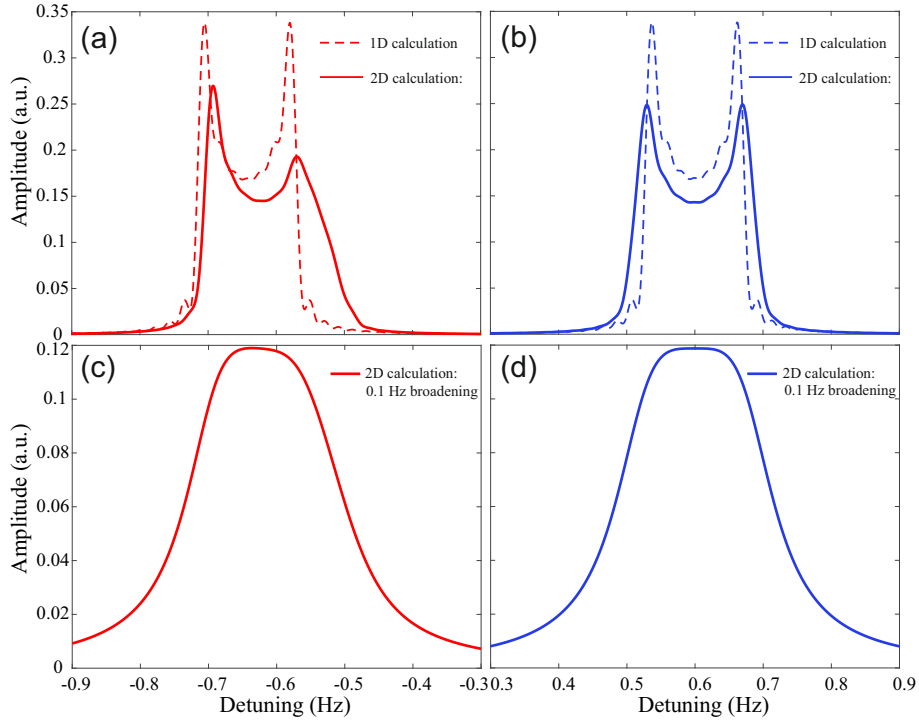


Figure 3.7: (a) The numerically calculated spectroscopy lineshapes for Magnesium atoms in a $88 E_R$ deep lattice is shown here for E1-magic wavelength (a,c) and operational magic wavelength (b,d). These calculations are performed by considering the 200 lowest transverse states. These lineshapes are also compared to the corresponding pure 1D lattice calculations shown by dashed lines in (a,b). The effect of a small 0.1 Hz line-broadening is shown in (c) and (d), corresponding to the lineshapes seen in (a) and (b) respectively.

In addition to the linewidth asymmetry of the carrier lineshape arising from the AC Stark shift inhomogeneity, variation of dipole transition element with quasimo-

momentum and transverse states leads to additional amplitude asymmetry of the two peaks as lattice wavelength is detuned from the magic condition. These linewidth and amplitude asymmetries observed in the experimental data matches well with the numerical calculations as can be seen in Fig. 3.6.

While these lineshape distortions observed as lattice wavelength is varied from magic wavelength, are not ideal for a lattice clock operation, they can be used as a tool to detect deviation from the magic condition as well. Considering the higher order AC Stark shift contributions, this could be useful for future state of the art lattice clocks. Similar lineshape distortions have been used previously to determine the magic wavelength [110, 111]. However, with improving spectroscopy resolution, lineshape distortions of Bloch band spectrum allows for observing much smaller lattice light shift inhomogeneity.

As an example, we look at the lineshape distortions for Magnesium clock spectroscopy as a result of higher order AC Stark shifts. In Fig. 3.7(a), lineshape is shown for ^{24}Mg at the E1 magic wavelength and $88 E_R$ deep lattice, using theoretically calculated atomic parameters [112]. For such a deep optical lattice, the tunneling rate as well as the nonlinear AC Stark shift contribution is in sub-Hz regime, which is ideal for observing a distortion of the Bloch band spectrum. In these calculations, contribution from only the lowest 200 radial states is considered, which already gives rise to significant lineshape asymmetry (solid line) compared to the pure 1D calculation (dashed line). Similar calculation at operational magic frequency (-9.8 MHz detuning from E1-magic frequency) results in a symmetric lineshape (Fig. 3.7(b)). This behavior can be understood much the same way as in Fig. 3.6, where at operational magic condition, the light shift is invariant to first order for different transverse states whereas at E1-magic wavelength, the light shift varies for different transverse states. These calculations show that with sufficient spectroscopy resolution, deviation from operational magic condition can be directly detected using symmetry of the lineshape.

To further demonstrate the advantage of the Bloch band spectroscopy, we look at the same lineshapes as in Fig. 3.7(a-b) with additional line-broadening of 0.1 Hz. These broadened lineshapes are shown in Fig. 3.7(c-d). As can be seen here, the lineshape asymmetry is almost completely washed out and the two lineshapes look almost identical. Therefore, resolving the Bloch band feature offers a more sensitive measurement of any lattice light shift inhomogeneities. Indeed, such a measurement does not allow to directly infer the atomic parameters. However, it can be used as an effective first observation of deviation from operational magic condition.

3.2 Line-broadening mechanisms in a deep optical lattice

As seen in the last section, to reduce the line-broadening due to atomic motion, the lattice depth should be increased such that the Bloch band width decreases below the Rabi frequency. However, for higher radial states, the Bloch band width is also higher, which can still give rise to line broadening. Therefore, the atomic temperature needs to be reduced to a level where higher Bloch bands and radial states are not significantly populated.

As discussed in chapter 1, our state preparation scheme essentially consists of filtering the lowest energy atoms into our optical lattice while the relative occupancy of the trapped states is still determined by the MOT temperature of about 1 mK. Therefore, the measurements are significantly influenced by the higher motional states and their associated line broadening. In this section, we investigate these effects and possibilities of reducing their influence.

The tool most often used for characterizing the atomic temperature in optical lattice is the sideband spectroscopy. This also allows to efficiently estimate the trap frequency. We performed such measurements in our experiments as shown in Fig. 3.8. The experimental data is fitted with the theoretical model from [113]. The atomic temperature obtained from the sideband scan is 42(3) μK and 119(6) μK for the axial and transverse directions respectively. Similar radial and axial temperatures of 46(4) μK and 145(12) μK were also obtained from a semiclassical model where transverse axes are treated classically while the motion along the lattice axis is treated as a quantum harmonic oscillator with additional quartic anharmonic term. The theoretical models are limited due to the high atomic temperature which requires a very large number of radial states, where for higher states, a 4th order approximation of the Gaussian potential does not work well enough. Nevertheless, it allows for extracting an estimate of the atomic temperature.

The sideband measurements show that the atomic temperature is very high despite the filtering process used to remove the most energetic atoms in the trap. Therefore line-broadening due to higher axial as well as radial states needs to be considered. Though the higher Bloch bands can also lead to line-broadening, their contribution is low as long as the bandwidth of higher Bloch bands is significantly larger than the spectroscopy resolution. Radial states on the other hand are more important for line-broadening of the carrier transition as also seen in the last section.

To see the influence of radial states on transition broadening, we performed measurements at relatively shallow lattice depths where the line-broadening is much easier to resolve with our spectroscopy laser. Additionally, the contribution of

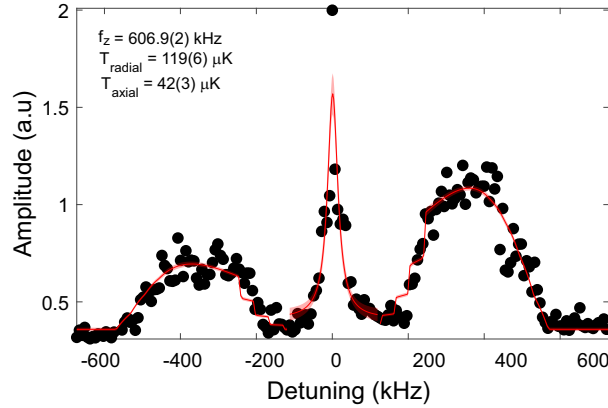


Figure 3.8: Sideband spectrum for the atoms trapped in optical lattice at the magic frequency. The data is fitted with the theoretical model from [113]. The sideband scan helps to characterize the trap depth as well as the atomic temperature.

radial state transitions directly depends on the Rabi frequency and hence on the intensity of spectroscopy laser. To systematically show this effect, we performed line scans at $28.5 E_R$ where the lattice depth was then ramped down to $9 E_R$ and back up to remove some of the higher energy atoms in the lattice. Line scans were performed for different spectroscopy laser powers keeping the homogeneous magnetic field constant at around 75 G.

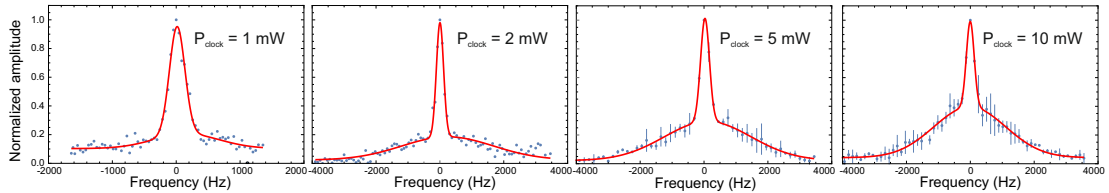


Figure 3.9: Spectroscopy of clock transition showing the contribution of higher order transverse states: The trap depth for all these scans is $28.5 E_R$ with a ramp down depth of $9 E_R$. As the clock laser power is increased, the increase in contribution of radial sidebands is visible. The spectroscopy pulse was 100 ms in all the measurements. The Rabi frequency in these measurements varies between 50 Hz for $P_{\text{clock}} = 1$ mW to 160 Hz for $P_{\text{clock}} = 10$ mW.

The spectroscopy results shown in Fig. 3.9 demonstrate the presence and large contribution of different radial states in the line broadening at high Rabi frequencies. In order to reduce the occupation of higher Bloch bands for our experiments, we ramp down the lattice to lower depths U_{ramp} during the state preparation to filter out high energy atoms, before increasing the depth again to the maximum value for the spectroscopy. The effectiveness of this method is shown in Fig. 3.10. The data shown here is taken at a lattice depth of $61 E_R$ for different U_{ramp} ranging from $6.1 E_R$ to $22.9 E_R$. As U_{ramp} is increased, more higher energy atoms are retained in the lattice. Therefore the effective lattice depth decreases with increase in U_{ramp} , leading to an enhanced line broadening associated with tunneling between lattice sites. For our experiment, these lineshapes were also studied in the PhD thesis of Klaus Zipfel [78] at shallower trap depths available during that time,

showing similar behavior.

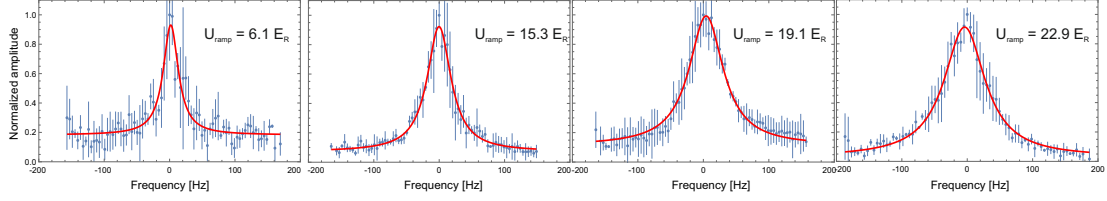


Figure 3.10: Spectroscopy of the clock transition showing the line broadening due to higher atomic temperatures. The trap depth for all these scans is $61 E_R$ with a different U_{ramp} as stated in figure legends. As U_{ramp} is increased, the effective lattice trap depth decreases due to occupation of higher radial states. Since lower effective trap depth leads to a larger Bloch band width, the lineshape becomes broader.

The linewidth extracted from the spectroscopy measurements of Fig. 3.10 show clear trend as a function of U_{ramp} . We model this linewidth dependence on U_{ramp} as a broadening coming from the Bloch bandwidth of the lattice, where the effective lattice depth (U_{eff}) depends linearly on U_{ramp} : $U_{\text{eff}} = U_0 + \alpha U_{\text{ramp}}$. Of course such a model is only an approximation to reality where it is assumed that the ramping down of lattice depth acts as an effective cut-off limit for the higher energy atoms. The numerical fit to the experimental data gives $U_0 = 43(17)E_R$ and $\alpha = 0.4(5)$.

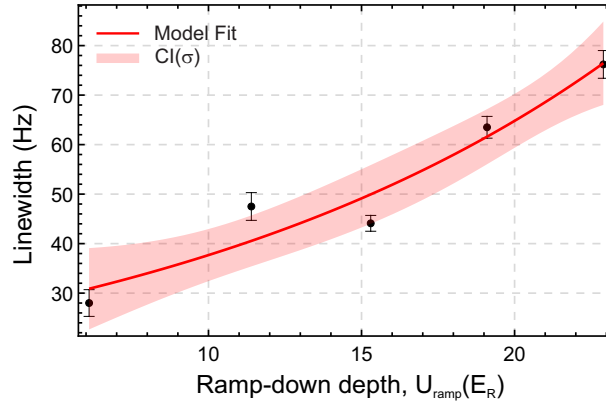


Figure 3.11: Spectroscopy linewidth as a function of U_{ramp} . As U_{ramp} is increased, the effective trap depth decreases leading to a line broadening. This effective trap depth has been modeled with a linear dependence on U_{ramp} giving rise to the shown numerical fit to the experimental data.

Though the value of α has a large error, it still gives a good qualitative understanding of what exactly may be happening as we ramp down the lattice depth to remove high energy atoms. Assuming a uniform distribution of atoms between the lowest energy up to a cut-off energy U_{ramp} , the average trap depth would be $U_0 + U_{\text{ramp}}/2$. Therefore the α value of 0.5 seems reasonable from such an argument.

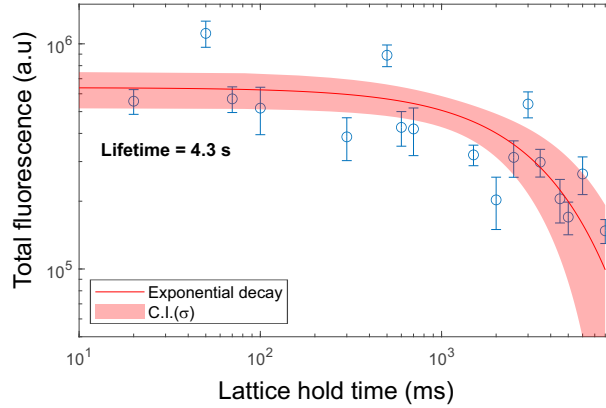


Figure 3.12: Measurement of atom number trapped in the lattice as a function of lattice holding time.

Lifetime in the lattice

Another indicator of heating in optical lattice is the lifetime of atoms in the lattice. We measured this lifetime by detecting the fluorescence of atoms as a function of holding time in a $29 E_R$ deep lattice. The fluorescence signal, which is directly proportional to the atom number in the lattice decays exponentially as a function of holding time, as shown in Fig. 3.12. The exponential decay rate gives a lattice lifetime of $\tau = 4.3$ seconds. This sets a limit to the minimum linewidth of $1/2\pi\tau = 69$ mHz due to the lifetime induced dephasing during spectroscopy. Similar lifetime was also observed for a deeper lattice depth of $46 E_R$ as well as in the far-off resonance 1064 nm optical dipole trap, indicating that dominant contribution to the lifetime is coming from the common background gas collision losses.

With help of the measurements in this section, the optimum state preparation and spectroscopy setting for our system can be determined. To reduce the contribution of higher energy atoms in the lattice, the lattice depth needs to be ramped down to the lowest possible value, while still keeping significant atom numbers. In our case, this corresponds to U_{ramp} of around $10 E_R$. Furthermore, care needs to be taken to optimize the Rabi frequency with respect to the spectroscopy time to not allow for any off-resonance contributions.

Following the discussion in this chapter on line broadening mechanisms in the optical lattice, we can move to a detailed characterization of clock performance in the next chapters.

Magnesium lattice clock instability in 10^{-17} regime

The performance of our magnesium lattice clock in the 2017 measurement campaign [79] was limited by two factors:

- (a) lack of available lattice power, leading to large tunneling induced line broadening, and
- (b) fluctuating probe AC Stark shift affecting the clock instability as well as the uncertainty budget.

As discussed in Sec. 3.1, at low lattice depths, significant tunneling induced line broadening occurs. This had limited the observable clock transition linewidth to 51 Hz, which limited the instability to about 5.1×10^{-16} after 400 seconds [78]. This also impacted the systematic shift measurements, where uncertainties were limited by measurement instability.

In addition to the tunneling induced line-broadening, additional line-broadening was also observed due to inhomogeneous probe laser intensity over the atomic sample [78]. This inhomogeneity of the probe laser intensity occurs due to parasitic reflections of the probe laser light within the lattice enhancement cavity, leading to the formation of a standing wave. While this line-broadening limited the line-Q of the clock transition, the temporal fluctuations of probe intensity inhomogeneity led to further deterioration of the clock instability, due to fluctuations of the associated probe laser AC Stark shift. Since these temporal fluctuations made it difficult to characterize the probe laser AC Stark shift beforehand, an “in-situ”

measurement of the probe AC Stark shift was performed during the frequency measurement campaign. This further impacted the total instability of the frequency measurement due to an extended cycle time of the clock sequence.

As both these effects were closely linked to the lattice enhancement cavity setup, upgrades to the lattice setup were carried out in the context of this thesis to overcome these performance limitations. This led to not only a significant increase in available lattice depth, but also the elimination of any probe laser intensity inhomogeneity. In this chapter, these experimental system details as well as characterization of resulting clock linewidth & instability will be discussed.

4.1 Spectroscopy in Hz regime

The lattice enhancement cavity is at the heart of our magnesium clock experiment. Within this cavity setup, additional mirrors overlap the 1064 nm dipole trap to the lattice, while the probe laser is coupled in via one of the end mirrors of the cavity. A schematic of the setup can be seen in Fig. 4.1, where mirror M_3 is used to out-couple the probe laser light from the enhancement cavity. In addition, it is important to stress that the cavity setup is outside the vacuum chamber, and therefore the light passes through the chamber viewports. The upgrades discussed in this section are focused on improving the performance of this enhancement cavity.

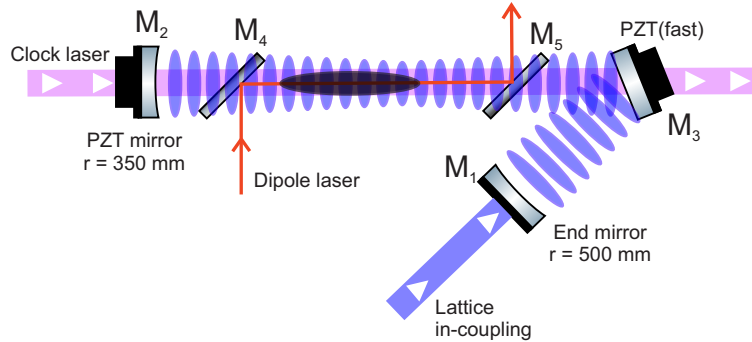


Figure 4.1: A schematic diagram of the lattice enhancement cavity setup. The enhancement cavity is setup in a concentric design. the dipole trap is overlapped with the lattice using mirrors M_4 and M_5 , while the probe laser is coupled out of the cavity by mirror M_3

4.1.1 Lattice power upgrade

The circulating optical lattice power in the enhancement cavity (P_{circ}) is determined by the in-coupling light power (P_{inc}) and the finesse (\mathcal{F}) of the enhancement

cavity.

$$P_{\text{circ}} \approx P_{\text{inc}} \frac{\mathcal{F}}{\pi} \quad (4.1)$$

Therefore, to improve the circulating power in the lattice, we decided to improve both the in-coupling power as well as the cavity finesse. The details of the lattice laser system are described in section 2.7. However, the Ti:Sa laser system was so far pumped by a 15 W laser system, leading to only about 300 mW of in-coupling power (P_{inc}) to the enhancement cavity. Therefore, as a first measure to increase lattice power, the pump laser was upgraded from 15 W to 18 W power. This helped increase the Ti:Sa laser power from about 1.2 W to 1.6 W, increasing the cavity in-coupling power to more than 400 mW.

Since the lattice enhancement cavity mode passes through vacuum chamber windows, the biggest contribution to cavity loss comes from the vacuum window coating. We have observed a slow decay in cavity finesse with time due to degradation of vacuum window coatings from within the vacuum chamber. The most likely cause of this coating degradation is a deposition of magnesium atoms on the anti-reflection coating. Therefore to improve the cavity finesse, these vacuum chamber windows were replaced. In addition, these windows were further customized to be anti-reflective for 1064 nm light as well. This helped to reduce the scattered dipole laser light during fluorescence detection. We observed a loss of less than 0.4% for a single pass through both the vacuum chamber windows. The mode-matching of the lattice light coming from the fiber collimator to the enhancement cavity was also optimized to about 83% mode overlap.

These upgrades helped increase the maximum circulating lattice power from 4 W to 10 W. In terms of trap depth in recoil energy units, this amounted to an increase from $30 E_R$ to $60 E_R$ (depending on the lattice waist). This leads to a reduction in tunneling induced line broadening from more than 20 Hz to the sub-Hz regime.

In Fig. 4.2, the reduction in linewidth as a function of lattice depth is shown. The experimental data is fitted with a model consisting of tunneling induced line-broadening dependent on the effective lattice depth ($U = \zeta \times U_0$) characterized by parameter ζ and an additional line-broadening $\Delta\nu_{\text{bg}}$ from all other sources, both as fit parameters. It is important to consider the effective reduction of lattice depth in the model since not all atoms are trapped at the peak lattice intensity. In some ways, this effect is related to the atomic temperature in the lattice.

$$\Delta\nu = \sqrt{\Delta\nu_{\text{bg}}^2 + \Delta\nu_{\text{tunnel}}^2} \Big|_{U=\zeta U_0}. \quad (4.2)$$

The line-broadening mechanisms are assumed to be inhomogeneous broadening and therefore their linewidths are added as expected from convolution of two Gaussian

functions. The numerical fit gives a background line-broadening $\Delta\nu_{\text{bg}}$ of 16(8) Hz, which is a combination of multiple effects, some of which will be discussed in Sec. 4.1.2. The fit parameter $\zeta = 0.93$ suggests a 93% reduction in effective lattice depth compared to the lattice depth at the center of trap. This is not completely unexpected since the atoms occupy different regions along transverse axis, leading to a lower mean value of the lattice depth.

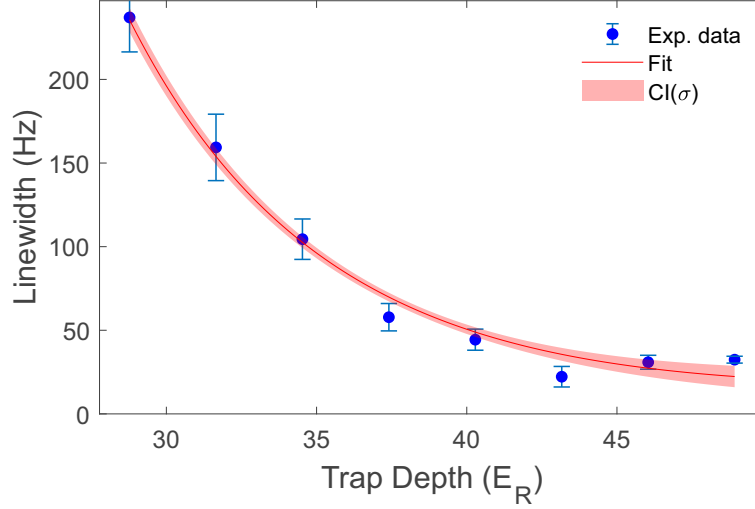


Figure 4.2: Spectroscopy linewidth is shown here as a function of trap depth. The experimental data is fitted with model in Eq. 4.2, showing lattice induced line-broadening.

Since at the trap depth of $50 E_R$, the tunneling induced broadening is below 10 Hz, we expect to resolve the clock transition with similar resolutions as well. To demonstrate the ultimate line-Q of our measurements, we perform Rabi spectroscopy of the clock transition at around $50 E_R$, keeping the probe intensity as low as possible, to suppress the associated line-broadening as discussed in the last section. A 200 ms long spectroscopy pulse was used to perform spectroscopy. Some of the lineshape measurements are shown in Fig. 4.3. As can be seen here, the clock transition linewidth varies for different scans. This occurs due to a drifting probe laser frequency, where scanning the frequency in the direction of laser drift results in larger linewidth and vice versa.

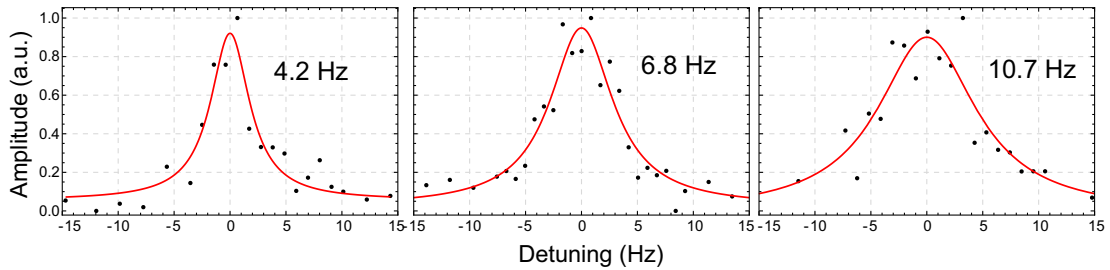


Figure 4.3: Spectroscopy scans of the clock transition showing different linewidths. The variation in linewidth is due to a drifting probe laser frequency which causes the scanned linewidth to be larger or smaller depending on the scan direction.

Therefore to get a good estimate of the transition linewidth, many such line scans were performed and a histogram was generated as shown in Fig. 4.4. The mean linewidth was measured to be $7(3)$ Hz which is about 3 Hz larger than the expected Fourier linewidth limit. This is the first demonstration of suppressing the tunneling line-broadening in Hz regime for magnesium, and the highest line-Q of $9(3) \times 10^{13}$.

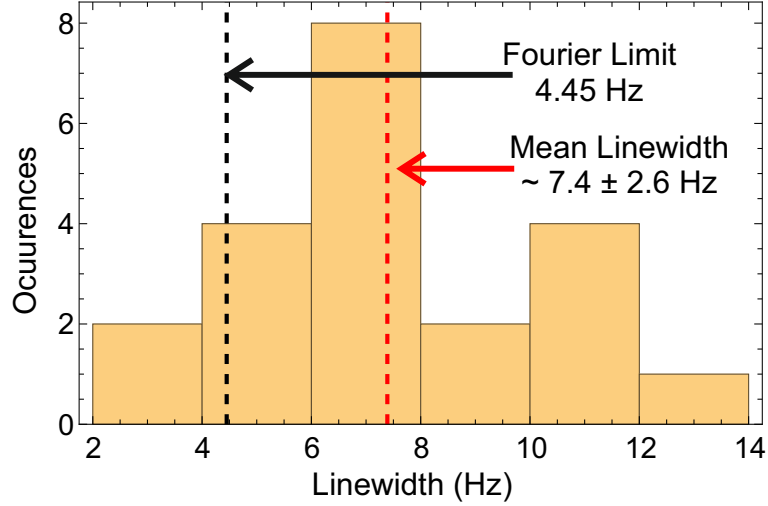


Figure 4.4: Histogram of linewidth measurements generated from multiple line scan measurements. The spread in linewidth values indicates a large influence of the spectroscopy laser drift. The mean linewidth of $7(3)$ Hz is the smallest linewidth resolved for magnesium clock so far.

4.1.2 Suppression of probe laser inhomogeneity

Going to deep trap depths alleviates a major performance bottleneck for magnesium lattice clock. However, there was still the issue of the probe laser intensity inhomogeneity in the lattice setup. This inhomogeneity develops due to unwanted reflections within the enhancement cavity. The enhancement cavity was designed to act as a resonant cavity for the 468 nm lattice light while transmitting the 458 nm clock laser light. Therefore, a folded cavity design was chosen for the enhancement cavity, where the folding mirror M_3 was especially coated for high reflection of 468 nm light and high transmission at 458 nm. However, since the two wavelengths are very close to each other, a mismatch in the lattice design angle led to significant reflections of the probe laser. This leads to formation of a standing wave due to interference of the light traveling in opposite direction.

The probe laser standing wave is seen by the atomic cloud as an inhomogeneous intensity distribution. This inhomogeneity degrades the clock performance in two ways. The first is a line broadening of the clock transition and the second is a fluctuation of the probe laser induced AC Stark shift.

The linewidth measurements of the clock transition as a function of clock laser intensity is shown in Fig. 4.5. An almost linear dependence of the linewidth on the clock laser intensity is clearly visible here. This issue was highlighted first in the PhD thesis of Klaus Zipfel [78] where the line-broadening mechanism was understood to be stemming from the build-up of a standing wave of probe laser within the lattice enhancement cavity. This therefore leads to an inhomogeneity of the Rabi frequency, leading to a power broadening as well as an inhomogeneity of the probe AC Stark shift. Though power broadening appeared to be the stronger contribution to the line broadening in the previous measurements [78], the observations shown here indicate that the line-broadening predominantly occurs due to inhomogeneity of the probe-AC Stark shift experienced by the atomic sample.

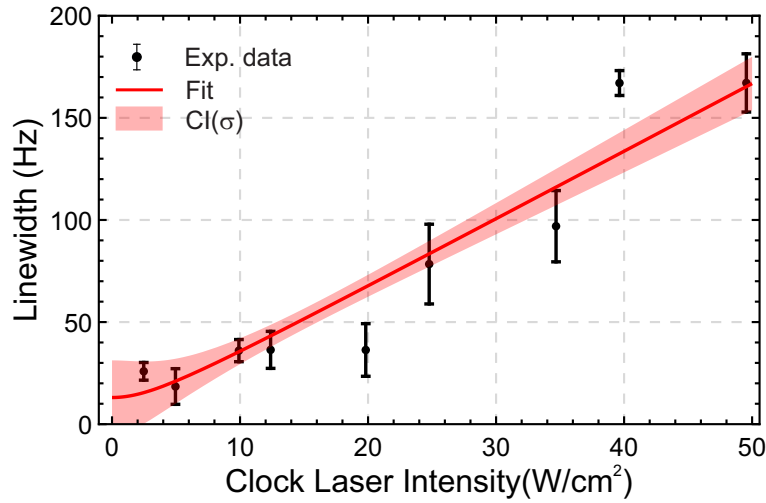


Figure 4.5: Linewidth dependence on probe laser intensity. Due to a formation of probe laser standing wave within the enhancement cavity, large inhomogeneity of probe laser AC Stark shift is introduced. This leads to an increased line-broadening as the laser intensity is increased.

In principle, the total linewidth at any given probe laser intensity will be given by a combination of three contributing factors: (a) a background line broadening $\Delta\nu_{\text{bg}}$ coming from a combination of tunneling broadening and Fourier broadening, (b) power broadening $\Delta\nu_{\text{power}}$ induced by an increase in Rabi frequency as probe laser power is increased, and (c) broadening induced by a variation of probe AC Stark shift over the atomic sample $\Delta\nu_{\text{AC}}$:

$$\Delta\nu = \sqrt{\Delta\nu_{\text{bg}}^2 + \Delta\nu_{\text{power}}^2 + \Delta\nu_{\text{AC}}^2}, \quad (4.3)$$

where $\Delta\nu_{\text{power}} \propto \xi\sqrt{|\Delta_{\text{L}}\Delta_{\text{B}}|}$ [87] and $\Delta\nu_{\text{AC}} \propto \Delta_{\text{L}}$. Here $\Delta_{\text{L}} \propto I_{\text{L}}$ is the probe laser induced AC Stark shift, $\Delta_{\text{B}} \propto B^2$ is the second order Zeeman shift and $\xi = 0.28$ is a theoretically calculated scaling factor [87].

During these linewidth measurements, homogeneous magnetic field was around 3 Gauss, which gives a frequency shift $\Delta_{\text{B}} = 23.2$ Hz. The dependence of probe AC

Stark shift on the probe laser intensity was also measured to be $\Delta_L = 3.1I_L$ Hz, where I_L is the probe laser intensity in units of W/cm^2 . Therefore the associated power broadening will weakly depend on the probe laser intensity,

$$\Delta\nu_{\text{power}} = \frac{1}{\sqrt{2\pi}} 2\pi \times \xi \sqrt{|\Delta_L \Delta_B|} \approx 3.4 \sqrt{I_L} \text{ Hz}, \quad (4.4)$$

Eq. 4.4 shows that the power broadening contribution is really small for the parameter range shown in Fig. 4.5, with the maximum contribution at highest intensity being about 24 Hz. Therefore, we neglect the power broadening contribution in Eq. 4.3 and use the remaining two terms to model the experimental data. This argument is also supported from numerical fit performance, where even using the complete model from Eq. 4.3, the contribution from power broadening is negligible while adding large uncertainty to the total fit. The numerical fit to the experimental data reveals a background line-broadening of 13(17) Hz with a linear dependence on probe laser intensity of 3.3(3) $\text{Hz}/(\text{Wcm}^{-2})$. Assuming a perfect standing wave formed with an incident laser of intensity I_0 , the atoms experience a mean laser intensity of $2I_0$ with a standard deviation of $\sqrt{2}I_0$. This gives rise to a relation between the FWHM linewidth and the probe AC Stark shift, $\Delta\nu_{AC} = \sqrt{4 \ln 2} \Delta_L \approx 1.66 \Delta_L$. Therefore using the measured probe AC Stark shift sensitivity with same setup of 3.1(1) $\text{Hz}/(\text{Wcm}^{-2})$, the line broadening sensitivity is expected to be approximately 5.2 $\text{Hz}/(\text{Wcm}^{-2})$. However, a lower value obtained from data in Fig. 4.5 indicates that the atoms experiencing lower probe laser intensity contribute less to the total lineshape, leading to a deviation from the simple averaging of the standing wave intensity pattern.

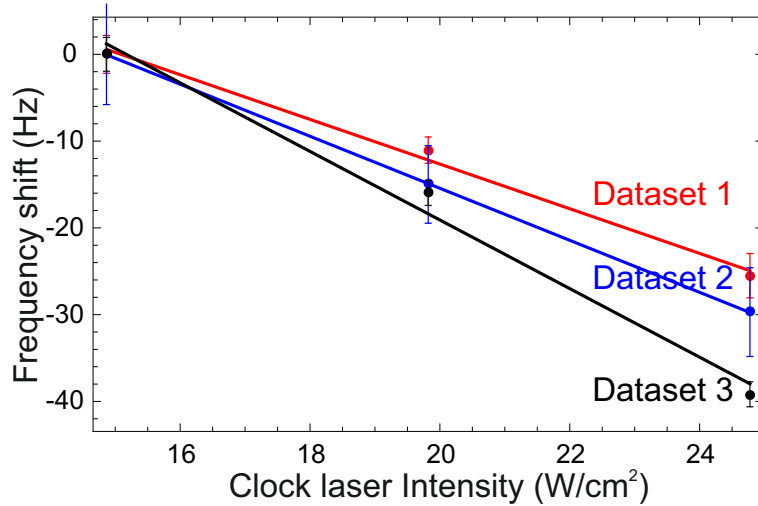


Figure 4.6: A set of measurements for probe AC Stark shift showing a large variation over time in the sensitivity of transition frequency on the probe laser intensity.

In addition to the line-broadening induced by the parasitic reflection of the probe laser, a fluctuation in probe AC Stark shift was also observed. One example of such

variation is shown in Fig. 4.6. The three datasets shown here were recorded within a couple of hours of measurement time. A large variation in the slopes is clearly visible. Due to the parasitic reflection of probe light within the enhancement cavity, the cavity amplifies the probe laser intensity seen by the atoms albeit staying in a bad cavity regime. Therefore the probe laser intensity fluctuates, as the length of the enhancement cavity fluctuates with respect to probe laser wavelength. These fluctuations not only lead to a degradation of the clock stability, but also make it very hard to estimate the probe AC Stark shift.

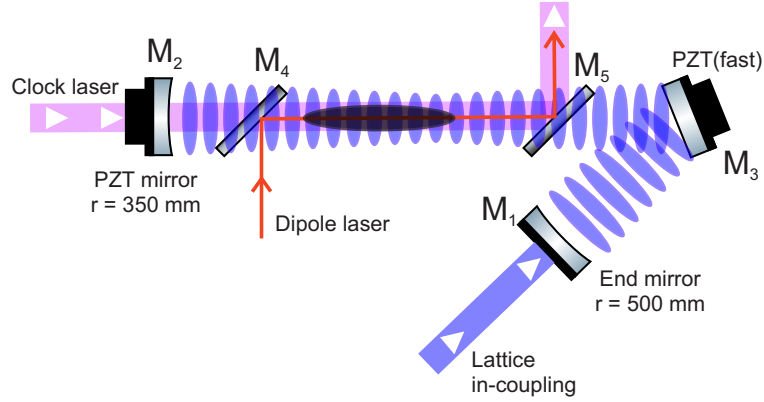


Figure 4.7: A schematic diagram of the new lattice enhancement cavity setup. Now, the dichroic mirror M_5 used as the out-coupler for 1064 nm light is also used as an out-coupler for the probe laser beam.

To reduce the parasitic reflections of the probe laser within the enhancement cavity, the cavity design was further modified. The dichroic mirror M_5 used thus far to out-couple the dipole laser light as shown in Fig. 4.1 is replaced with a mirror that not only reflects the 1064 nm dipole trap, but the 458 nm probe laser as well. This mirror had a transmission better than 99.5 % for the 468 nm lattice laser light, while reflecting more than 99% of the probe laser as well as the 1064 nm laser light. The orthogonal polarization of lattice and probe laser beams helped immensely in such a mirror coating design. The schematic for the modified enhancement cavity is shown in Fig. 4.7.

After this modification of the lattice setup, no back-reflection of the probe laser was observed, while the cavity finesse for the lattice light was also maintained at earlier levels mentioned in the previous subsection. The performance improvement was clearly visible in the new linewidth measurements performed for different probe laser intensities, as can be seen in Fig. 4.8. Fitting these measurements with the line-broadening model in Eq. 4.3, we obtain almost negligible contribution of the AC Stark shift induced broadening, with a small power broadening contribution of $\Delta\nu_{\text{power}}^{\text{fit}} = 1.9(8)\sqrt{I}$ Hz, which is quite close to the expected power broadening of $\Delta\nu_{\text{power}}^{\text{theo}} = 1.7\sqrt{I}$ Hz estimated using Eq. 4.4 with the Zeeman and probe AC Stark shift sensitivities.

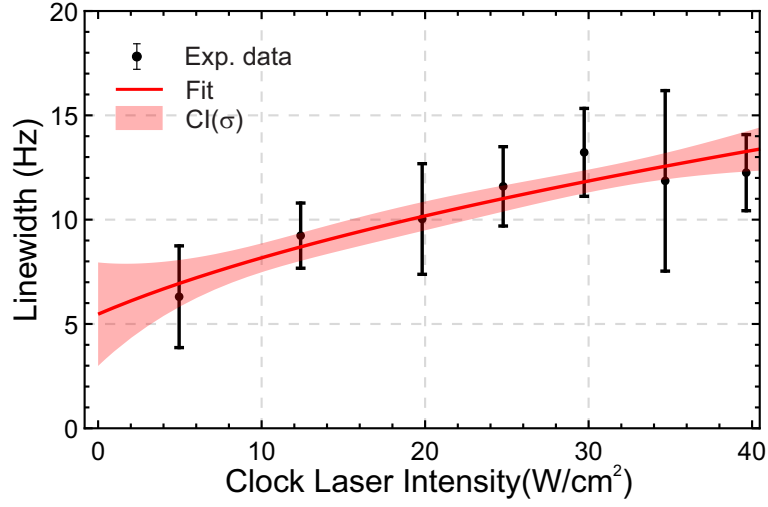


Figure 4.8: Clock transition linewidth measurement as a function of probe laser intensity performed after replacing the mirror M_5 is shown here. A much smaller dependence on intensity is observed.

In addition to the suppression of probe field induced inhomogeneous line-broadening, the fluctuations of probe AC Stark shift were significantly reduced as well (Fig. 4.9). Here AC Stark shift sensitivities for different data sets were again compared and the frequency shift dependence on probe laser intensity was found to be equal for all data sets within the measurement uncertainties.

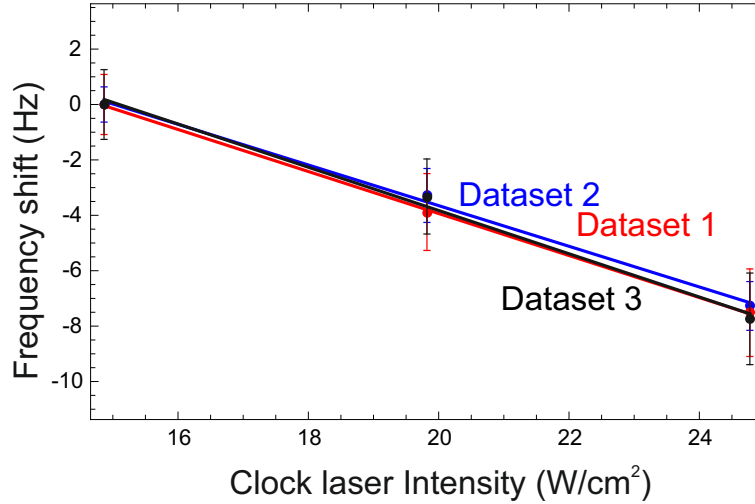


Figure 4.9: Probe laser induced AC Stark shift measurement as a function of the probe laser intensity. The slope of the three data sets are identical within the uncertainties, suggesting elimination of the probe laser intensity fluctuations.

A comparison of the average AC Stark shift sensitivity also points towards the validity of our standing wave hypothesis for the probe laser field. This can be seen in Fig. 4.10, where the probe AC Stark shift sensitivity is almost a factor of 4

larger in the older lattice setup of Fig. 4.1 than the new setup (Fig. 4.7), most likely due to the maximum probe laser intensity at the antinodes in the standing wave being 4 time larger than for a continuous beam.

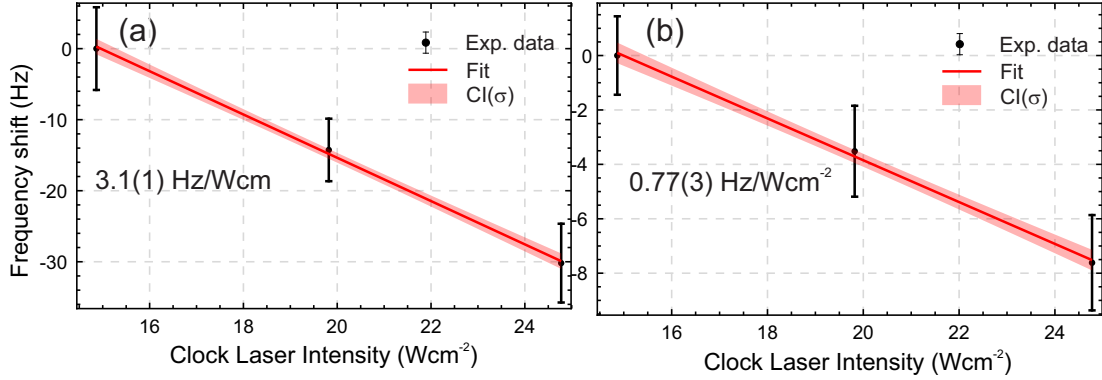


Figure 4.10: Probe laser induced AC Stark shift sensitivity before (a) and after (b) lattice enhancement cavity modification. The AC Stark shift sensitivity was reduced by almost a factor of 4 after suppression of the probe laser parasitic reflections in the cavity.

The probe laser standing wave also degrades the signal to noise ratio of the clock, since the atoms at the nodes of probe laser standing wave are not excited, while the excitation takes place predominantly at the antinodes of the standing wave, leading to a significant reduction in total signal. This was also observed after implementing the new dichroic mirrors, where the observed signal with similar experimental conditions was significantly better.

4.2 Frequency instability characterization

The improved lattice system leads to a suppression of various line-broadening effects which limited the clock performance thus far. Therefore, the magnesium clock transition was resolved for the first time in the Hz regime. In addition, the probe laser intensity fluctuations, the biggest contributor thus far to frequency instability is also suppressed. Therefore the clock instability is also expected to significantly improve.

To characterize the clock instability, a self-comparison measurement was performed, where two setpoints for the probe laser intensity were used to steer the laser frequency using a PI² regulator. The difference of frequency corrections applied to the two setpoints was used to estimate the Allan deviation of the frequency fluctuations. The resulting instability plot of Allan deviation as a function of averaging time is shown in Fig. 4.11.

The first striking result in Fig. 4.11 is that the instability reaches the 10^{-17} regime,

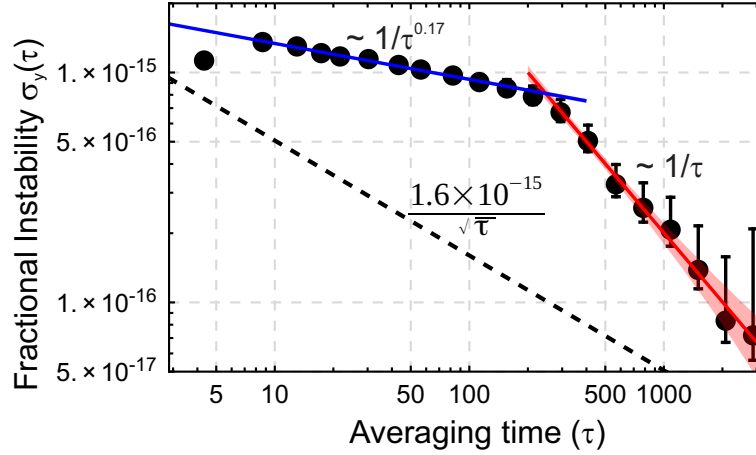


Figure 4.11: Clock instability shown in terms of fractional instability of a self-comparison measurement, where the frequency difference for two different probe laser intensity setpoints was measured. After a slow initial decay in instability, a fast instability averaging behavior is observed. The total instability in these time regimes is still much higher than the expected instability contribution from the atomic spectroscopy, shown by dashed line.

for the first time for a magnesium clock. However, the Allan deviation shown here has an unexpected dependence on averaging time τ , where initially the instability decreases rather slowly with a $1/\tau^{0.17}$ dependence followed by a very fast $1/\tau$ dependence after about 200 s. This is curious since the second of the two integrators used to lock the spectroscopy laser to the atomic signal has a time constant of 200 s as well. The clock instability reduces to $7.2_{-1.8}^{+7.7} \times 10^{-17}$ after an averaging time of 3000 seconds.

The $1/\tau$ dependence of Allan deviation suggests that the instability is neither dominated by quantum projection noise (QPN) nor by the Dick-noise, which both have $1/\sqrt{\tau}$ dependence on averaging time. There are also additional instability contributions arising from photon shot noise of the fluorescence detection as well as the noise of the detection system. However, again all of these introduce a white frequency noise, leading to a $1/\sqrt{\tau}$ behavior of the Allan deviation.

The Allan deviation of an atomic frequency standard can be characterized as [114]

$$\sigma_y^{\text{atom}} = \frac{1}{\pi Q} \sqrt{\frac{T_c}{\tau}} \left(\frac{1}{N} + \frac{1}{N n_{\text{ph}}} + \frac{2\sigma_{\delta N}^2}{N^2} \right)^{1/2}, \quad (4.5)$$

where the first term is the instability arising from QPN, the second term is the photon shot noise contribution in fluorescence imaging and the third term comes from noise in the detection due to a fluctuation of atom number. In this expression, Q is the quality factor of the spectroscopy line, while T_c is the cycle time of the clock. To estimate the instability contribution associated with the QPN and detection noise, we make use of the spectroscopy results, where the relation in Eq.

4.5 can be simplified as

$$\sigma_y^{\text{atom}} = \frac{1}{\pi QS/N} \sqrt{\frac{T_c}{\tau}}, \quad (4.6)$$

where S/N is the signal-to-noise ratio which can be estimated from spectroscopy line scan as the ratio of scan amplitude and the root mean square (rms) noise [94]. From our measurements with similar parameters, we get $S/N \approx 10$, which along with the 20 Hz linewidth used in this instability measurement leads to an estimated atomic instability contribution of $\sigma_y^{\text{atom}} \approx 1.3 \times 10^{-15}/\sqrt{\tau}$.

The expression for Dick noise [115] induced Allan deviation, which comes from the down-conversion of the local oscillator frequency noise at Fourier frequencies close to multiples of $1/T_c$ is given as

$$\sigma_y^{\text{Dick}} = \frac{1}{\sqrt{\tau} g_0} \sqrt{\sum_{n=1}^{\infty} (g_{\text{sn}}^2 + g_{\text{cn}}^2) S_{y_0} \left(\frac{n}{T_c} \right)}. \quad (4.7)$$

In this expression, g_0 , g_{cn} and g_{sn} are the Fourier coefficient of the sensitivity function $g(t)$:

$$g_0 = \frac{2}{T_c} \int_0^{T_c} g(t) dt, \quad (4.8)$$

$$g_{\text{cn}} = \frac{2}{T_c} \int_0^{T_c} g(t) \cos\left(\frac{2\pi n t}{T_c}\right) dt, \quad (4.9)$$

$$g_{\text{sn}} = \frac{2}{T_c} \int_0^{T_c} g(t) \sin\left(\frac{2\pi n t}{T_c}\right) dt. \quad (4.10)$$

The sensitivity function $g(t)$ is defined as the relative change in atomic excitation fraction δP as a function of phase change $\delta\phi$ of the local oscillator used to interrogate the atomic sample:

$$g(t) = 2 \lim_{\delta\phi \rightarrow 0} \frac{\delta P(\delta\phi, t)}{\delta\phi}. \quad (4.11)$$

For the Rabi spectroscopy used in our measurements, the sensitivity function can be expressed as [78]

$$g(t) = \begin{cases} 4\delta \frac{\Omega_0^2}{\Omega^3} \sin\left(\frac{\Omega}{2} \tau_{\text{pulse}}\right) \sin\left(\frac{\Omega}{2} (\tau_{\text{pulse}} - t)\right) \sin\left(\frac{\Omega}{2} t\right) & \text{for } t \in [0, \tau_{\text{pulse}}] \\ 0 & \text{elsewhere,} \end{cases} \quad (4.12)$$

where δ is the detuning of the probe laser from atomic transition, Ω_0 is the Rabi frequency, τ_{pulse} is the interrogation pulse duration, and $\Omega = \sqrt{\Omega_0^2 + \delta^2}$ is the effective Rabi frequency. For our clock laser system, the Dick noise induced instability is expected to be $1 \times 10^{-15}/\sqrt{\tau}$. Therefore the total instability coming from the spectroscopy process is $1.6 \times 10^{-15}/\sqrt{\tau}$.

As can be seen in Eqs. 4.5 and 4.7, the Allan deviation scales as $1/\sqrt{\tau}$, which is not what we observe in our measurements. However, in all these expressions of the Allan deviation based on different noise sources, analysis of the servo lock is missing. In other words, though the Dick noise very well captures the influence of local oscillator noise on the clock instability, it is valid only for a time regime much larger than the time constant of servo feedback loop. Usually, this crucial detail is not relevant, since servo time constants are either much smaller than the time interval of interest or the local oscillator noise is still sufficiently suppressed to achieve a white frequency noise leading to same $1/\sqrt{\tau}$ behavior.

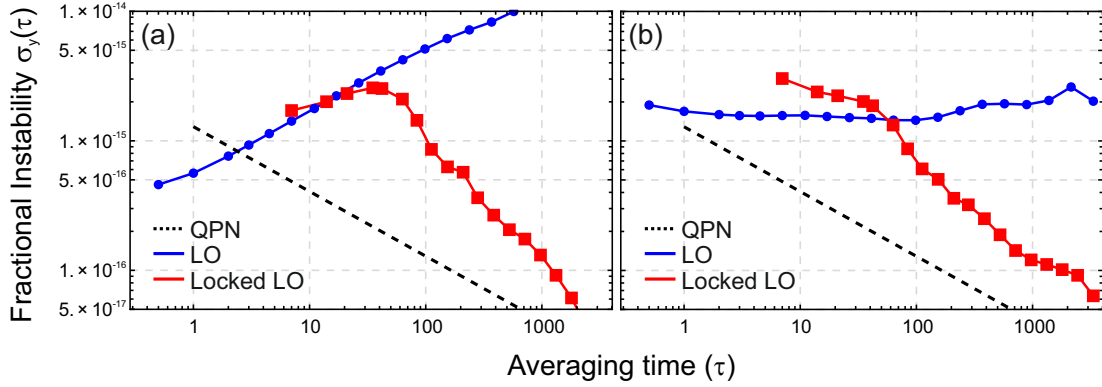


Figure 4.12: The results for numerical simulation of clock instability is shown here for local oscillator noise dominated by random walk (a), and flicker floor noise (b). The blue points denote the instability of free running local oscillator, whereas red points show the instability of the local oscillator locked to the atomic transition. The dashed line is the instability associated with QPN contribution.

To better understand the clock instability in a short to medium time regime, the clock operation was numerically simulated. This further allows to understand the behavior of the clock instability for different noise contributions such as white noise and random walk noise dominating the power spectral density of the local oscillator/probe laser. In Fig. 4.12 (a), the clock instability curve is simulated for a free running local oscillator dominated with random walk frequency noise, with similar servo locking time constants as used in our experiment. The dashed line is the QPN contribution. It can be clearly seen that the fractional instability follows approximately a $1/\tau$ dependence as was seen in our experimental results as well. A similar behavior is also seen for a local oscillator with flicker floor noise (Fig. 4.12(b)). Indeed the Dick noise puts a much more stringent limit on the long term instability behavior. However, in short to medium time scales (time scales comparable to servo integrator time constants), the instability behavior may significantly depart from the Dick noise limit. In particular for noise contributions such as random walk noise or the flicker floor noise, servo integrators help reduce the instability faster than $1/\sqrt{\tau}$ until the instability reaches the level of Dick noise/QPN limit, after which it follows the typical $1/\sqrt{\tau}$ behavior. Such deviation from $1/\sqrt{\tau}$ instability for clock spectroscopy performed with probe lasers domi-

nated by random walk and flicker noise was first shown in [116] using numerical simulations.

We know that our spectroscopy laser noise is strongly dominated by the random walk of frequency noise. Therefore, the clock instability curve seen from experimental measurements is not unexpected. This also highlights the possibility of significantly improving our clock performance by improving the performance of the local oscillator. Nevertheless, reaching an instability in the 10^{-17} regime in 3000 seconds is almost an order of magnitude improvement over our previous results. Indeed, this also makes it possible for the first time to characterize the systematic shift with uncertainties in 10^{-17} regime as well.

Systematic shifts affecting the clock

Clock performances are quantified by their stability and accuracy. While both these quantities are important for a frequency reference, the accuracy of a clock sets a more stringent limit on the clock performance since this cannot be improved by simply measuring for longer times. As in any other measurement, the clock frequency measurement inaccuracy stems from the systematic uncertainties affecting the measurement. For an atomic clock, these systematic shifts come predominantly from the external fields perturbing the clock transition frequency. The most dominant frequency shift contributions of a bosonic optical lattice clock are the AC Stark shifts coming from the lattice and the spectroscopy laser fields, and the Zeeman shift due to the magnetic field present during the measurement. For bosonic clocks, the Zeeman shift and spectroscopy laser induced AC Stark shifts are larger than for fermions, since much stronger magnetic field and spectroscopy laser intensity are needed to perform the clock spectroscopy. There are additional, smaller frequency shifts such as the DC Stark shift, collision shift and the second order Doppler shift.

One of the most important frequency shift contributions for optical clocks comes from the black body radiation. The BBR shift uncertainty is determined from the uncertainty of the temperature measurement and the atomic sensitivity to BBR. Therefore optical clock candidate elements with a low BBR sensitivity hold an edge with respect to the BBR shift uncertainty. This is what makes Magnesium a promising optical lattice clock candidate. The BBR shift sensitivity for Mg is

almost an order of magnitude smaller than for Strontium, and a factor of five smaller than for Ytterbium. More details on an estimation of the black body radiation shift for magnesium with associated uncertainty in 10^{-17} regime will be discussed in PhD thesis of Waldemar Friesen-Piepenbrink. Here, the focus is on the evaluation of other major frequency shift contributions affecting the performance of magnesium lattice clock, namely the probe AC Stark shift, Zeeman shift, collision shift and the lattice AC Stark shift.

5.1 Probe AC Stark shift

Compared to fermionic lattice clocks, bosonic clocks require larger probe laser intensities. Therefore, in our last frequency measurement campaign, the probe AC Stark shift formed a significant portion of the error budget. Additionally, the fluctuations of probe intensities within the enhancement cavity also complicated the analysis of shift uncertainty. With the modified setup discussed in Sec. 4.1.2, the probe laser intensity fluctuations were significantly suppressed. With a lower instability of the self-comparison measurements achieved due to a narrower clock transition, the probe AC-Stark shift uncertainty was also expected to be significantly lower.

To estimate the dependence of the frequency on the probe laser intensity, self-comparison measurements were performed between two probe laser power setpoints. A reference power setpoint of 5 mW was used for all the measurements, while the second setpoints was varied between different measurements. The resulting frequency differences as a function of the probe laser power difference is shown in Fig. 5.1. The linear dependence of the frequency shift on the probe laser power reveals a sensitivity of $-0.632(4)$ Hz/mW. At the expected clock operation setpoint of 5 mW, this leads to a frequency shift of $-3.16(2)$ Hz. In addition to the uncertainty of the shift sensitivity derived from these measurements, additional uncertainty from the beam pointing fluctuations also needs to be included, since the fluctuation of the probe laser beam position with respect to the lattice position leads to a probe laser intensity fluctuation for the atoms trapped in the lattice. Therefore, a long term measurement over multiple days was performed where the beam positions of the probe laser and lattice laser were recorded. The standard deviation of beam positions for both lasers was added to get a total beam overlap uncertainty of 20 μm . To reduce the impact of these beam pointing instabilities, the beam waist of the probe laser was increased before performing the measurements in Fig. 5.1 from 207(2) μm to 355(1) μm . This furthermore allows to operate the clock with a higher probe laser power of 5 mW compared to 3 mW in frequency measurement in 2017, which helps improve the phase stabilization of

the clock laser to the lattice cavity end mirror, due to a better heterodyne beat signal, while still keeping low intensity at the position of atoms. For a Gaussian laser beam, the overlap uncertainty between the lattice and probe beam leads to an uncertainty of the intensity at the position of atoms, giving rise to an additional frequency shift uncertainty of 0.02 Hz. Therefore the total fractional frequency shift uncertainty for the probe AC Stark shift is evaluated to be 6.1×10^{-17} .

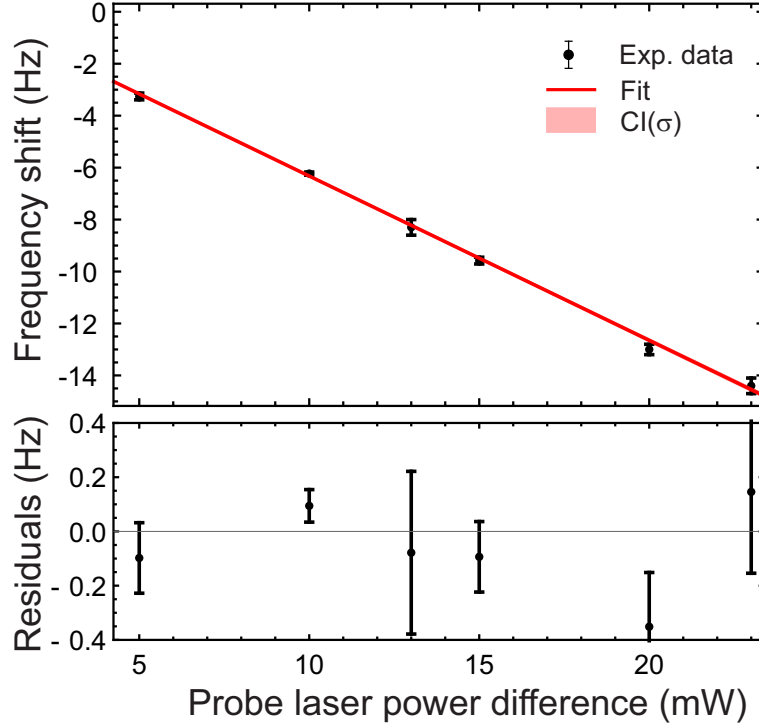


Figure 5.1: Measurement of the probe AC Stark shift: the frequency shift is measured as a function of the power difference between the reference value of 5 mW and the probe laser power of the other setpoints. As expected, a linear dependence on probe laser power is observed with a slope of $-0.632(4)$ Hz/mW.

For estimating the probe AC Stark shift, the calibration is performed with respect to the probe laser power as shown in Fig. 5.1 to avoid the influence of additional uncertainty from the beam waist measurement, which would affect the conversion of the probe power into intensity. Nevertheless, the measured beam waist of $355(1)$ μm gives an estimate for the dependence of AC Stark shift on laser intensity to be $-1.269(14)$ Hz/Wcm $^{-2}$. This value is larger than the theoretical estimates previously reported [87] by almost a factor of 2. This discrepancy could either be due to imprecision of theoretical calculations or due to some systematic discrepancy in beam waist measurement. Although this needs further analysis, this discrepancy does not impact the clock performance.

5.2 Quadratic Zeeman shift

For a bosonic isotope, the nuclear spin is zero. Therefore, there is no additional hyperfine splitting that is usually observed in fermionic lattice clocks. This gives bosons the advantage of having zero linear Zeeman shift. However, the nuclear spin is vital to provide a non-zero transition probability between the clock states that is otherwise forbidden due to selection rules. Therefore, the most commonly used method to perform spectroscopy in bosonic clocks is the magnetic field induced spectroscopy [87] as discussed in Sec. 2.4. However, the magnetic field required to perform spectroscopy also leads to a large magnitude of quadratic Zeeman shift. Since for a probe laser with longer coherence time, lower Rabi frequency is required, the required magnetic field and probe beam intensity can also be lowered, leading to reduced Zeeman and probe AC Stark shifts.

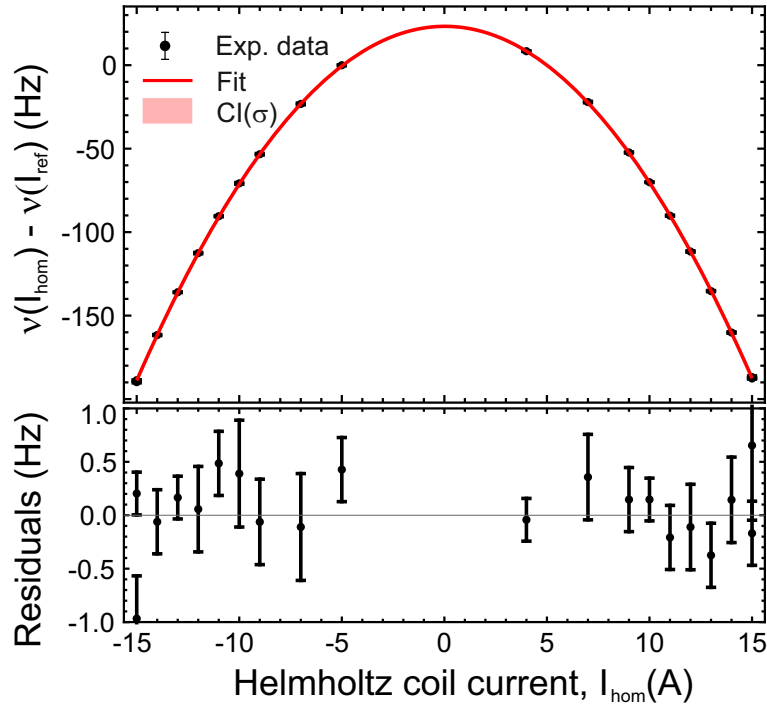


Figure 5.2: Quadratic Zeeman shift measurement: The data points are obtained by measuring the frequency difference between two interleaved clock sequences where the magnitude of the current carrying coil is kept fixed at 5 A for one of the sequences while it is varied for the other sequence between -15 A and 15 A. In this way, the quadratic dependence of the frequency shift on the current flowing through the Helmholtz coils is characterized. In the numerical fit to the data, an additional background fit is included as the fit parameter.

As discussed in Sec. 2.7.2, the magnetic field for spectroscopy is generated using a pair of current carrying coils in Helmholtz configuration. Therefore, the Zeeman shift is also characterized as a function of the current I_{hom} applied to these coils with respect to a reference setpoint of $I_{\text{ref}} = 5$ A. This measurement data is shown

in Fig. 5.2. A nonlinear regression fit is applied on the data with the quadratic shift model including a background field contribution

$$\nu_{I_{\text{ref}}} - \nu_{I_{\text{hom}}} = \beta_{\text{I}} \left[(I_{\text{ref}} - I_{\text{bg}})^2 - (I_{\text{hom}} - I_{\text{bg}})^2 \right], \quad (5.1)$$

where I_{bg} is the current equivalent for any background magnetic field along the axis of the applied magnetic field and β_{I} is the quadratic Zeeman shift coefficient, quantifying the sensitivity of the clock transition frequency on the applied current.

The nonlinear regression model matches the experimental data very well as can be seen in Fig. 5.2. The parameters β_{I} and I_{bg} are extracted from the fit as well:

$$\begin{aligned} \beta_{\text{I}} &= -0.9400(6) \text{ Hz/A}^2 \\ I_{\text{bg}} &= 0.021(3) \text{ A.} \end{aligned} \quad (5.2)$$

A calibration of the homogeneous magnetic field coils was previously performed by a measurement of the linear Zeeman shift on the $^1\text{S}_0 - ^3\text{P}_1$ transition [78]. This sensitivity of generated magnetic field on the applied current was determined from these measurements to be $0.6569(2) \text{ G/A}$. Therefore the quadratic Zeeman shift dependence on magnetic field is $\beta = 2.177(2) \text{ Hz/G}^2$. Though this value is in remarkable agreement with theoretical estimate of 2.17 Hz/G^2 , it does not agree as well with our previously measured value of $2.00(8) \text{ Hz/G}^2$. The cause for this disagreement is not fully clear, and needs further investigation. Nevertheless, this should not impact the uncertainty of the clock, as the calibration with coil current can be used to estimate the frequency shift.

The homogeneous magnetic field coil current stabilization scheme is described in the PhD thesis of Klaus Zipfel [78]. The long term current stability is limited by the detection instability, which for the current sensor¹ is 10 ppm/month with the 20 coil winding used in our setup, along with 100 ppm/2000 h for the low drift resistor² used to measure the secondary current generated by the IT 700-S sensor. These correspond to a current instability of 0.44 mA/month for $I_{\text{hom}} = 5 \text{ A}$. Assuming a much worse performance of 2.5 mA over 1 month and considering the uncertainty of β_{I} , I_{bg} and I_{hom} , the total frequency shift at the current setpoint of $I_{\text{ref}} = 5 \text{ A}$ is $-23.30(4) \text{ Hz}$. The associated fractional frequency uncertainty is 6.3×10^{-17} .

¹IT 700-S Ultrastab from LEM.

²VCS332Z from Vishay

5.3 Collision shift

Optical lattice clocks have an advantage over ion clocks since a large number of atoms can be trapped in an optical lattice, boosting the S/N ratio. However the interaction between atoms now also becomes relevant. In particular, atoms trapped at the same lattice site have a large interaction energy, which leads to a frequency shift for the clock transition. At low atomic temperatures that are typically observed in lattice clocks, s-wave collisions dominate the higher partial wave collision terms[117]. The frequency difference between the 1S_0 (g) and 3P_0 (e) states is modified due to the inter-atomic interaction as [118, 119]

$$\Delta\nu^{\text{coll}} = \frac{2\hbar}{m} \left(G_{\text{ge}}^{(2)} a_{\text{ge}} (\rho_{\text{g}} - \rho_{\text{e}}) + G_{\text{ee}}^{(2)} a_{\text{ee}} \rho_{\text{e}} - G_{\text{gg}}^{(2)} a_{\text{gg}} \rho_{\text{g}} \right) \quad (5.3)$$

where a_{ij} is the scattering length between atoms in state i and j . $G^{(2)}$ is the two-atom correlation function at zero distance, measuring the probability of simultaneously detecting the interacting atoms at the same point[120]. Therefore $G^{(2)}$ depends on the quantum statistical property of the interacting atoms. For a thermal atomic ensemble, there are three possibilities for $G^{(2)}$: (i) for indistinguishable bosons, $G^{(2)} = 2$, (ii) for indistinguishable fermions, $G^{(2)} = 0$ since identical fermions cannot occupy the same lattice site, and (iii) $G^{(2)} = 1$ for distinguishable particles. Therefore for fermionic clocks, Eq. 5.3 has contributions only from collisions of atoms in different states, leading to much lower collision shifts than bosonic clocks.

The important point to note in Eq. 5.3 is a linear dependence of the collision shift on the atomic density. Therefore the collision shift can be characterized by measuring the frequency shift as a function of atom number in the lattice. We perform interleaved frequency comparison measurements between two different sequences where the atom loading time is varied in one of the sequences. During the detection phase, the fluorescence signal from both the ground state as well as excited state atoms is detected, which gives a direct relation to the total atom number in the trap. These measurements are shown in Fig. 5.3, where a linear dependence of the frequency shift on the fluorescence signal is numerically fitted to the experimental data. As can be seen in the figure, the measurement uncertainties are already quite large. This is especially visible for higher atom number difference measurements. The main reason behind this performance degradation is the increase in cycle time due to large loading times necessary to increase the atom numbers in the lattice. This therefore degrades the instability of the clock quite significantly.

With the linear regression to the experimental data, the frequency shift is estimated to be $-0.04(9)$ Hz at operating fluorescence value of 10000 a.u., giving a fractional frequency uncertainty of 1.4×10^{-16} . Though this uncertainty is significantly larger

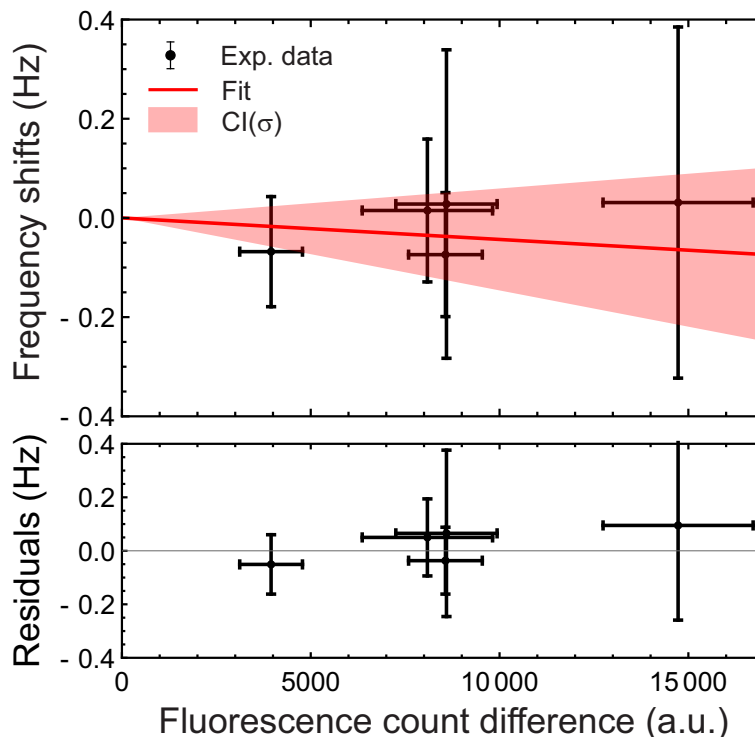


Figure 5.3: Collision shift measurement: the frequency shift is measured for different loading times to the dipole trap and hence for different total atoms trapped in the lattice. A linear dependence is fitted to the experimental data to estimate a total frequency shift of $-0.04(9)$ Hz at our operating setpoint.

than the uncertainties associated with Zeeman and probe AC Stark shifts, it can be improved by more measurement statistics.

5.4 Lattice AC Stark shift

The light fields that generate the strong trapping potential for the atoms also give rise to frequency shifts. Therefore the concept of the magic wavelength holds such an importance for optical lattice clocks. As discussed in Sec. 2.3, at the magic wavelength, the energy shift for the two clock states is identical, leading to effective cancellation of the lattice AC Stark shift of the clock transition frequency. The magic wavelength for ^{24}Mg was measured in our group in 2015 to be $468.46(21)$ nm [74], which was in excellent agreement with the theoretical prediction of $468.45(23)$ nm. These measurements were improved in 2017 [79], providing a more precise value of the magic wavelength of $468.4106(2)$ nm or $640.02071(29)$ THz.

To improve the magic frequency estimate, we performed measurements for lattice

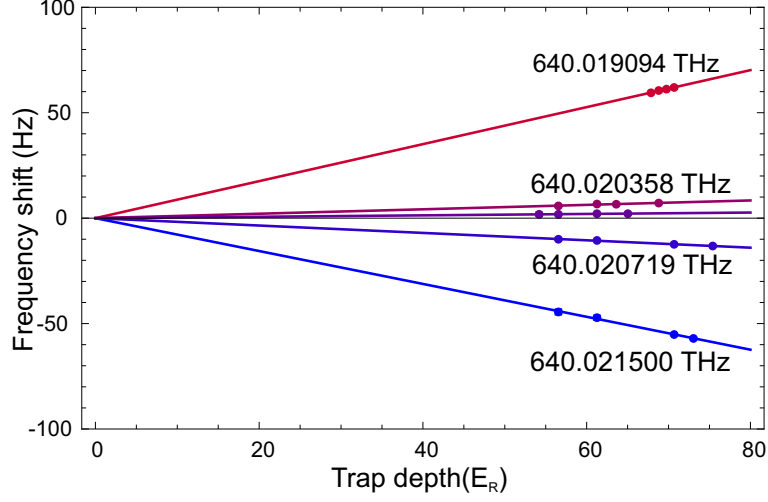


Figure 5.4: Lattice AC Stark shift measurements: the frequency shift dependence on the lattice intensity at a fixed lattice frequency was measured by performing differential frequency measurements between a fixed setpoint of $66 E_R$ and other variable lattice depth setpoints between $55 E_R$ and $75 E_R$. These measurements are repeated at different lattice frequencies which allows to estimate the magic lattice frequency to be $640.020528(28)$ THz.

AC Stark shift at lattice depths of 55 - $75 E_R$, as shown in Fig. 5.4. Within the precision of these measurements and the range of trap depths, the lattice shift follows a linear dependence on the lattice intensity. The magic frequency from these measurements was obtained to be $640.020528(28)$ THz, with an order of magnitude improvement in the uncertainty compared to our previous measurements [79]. It is important to point out that even at these lattice intensities, the AC Stark shift dependence on intensity is linear within the measurement precision. Unfortunately, the measurements cannot be performed for lower lattice intensities, since tunneling induced line-broadening starts to limit the measurement in this regime.

Though our measurements only show a linear lattice shift, recent theoretical results [112, 121] have suggested rather large nonlinear AC Stark shift at high lattice intensities, that are necessary for trapping magnesium atoms in a regime with reduced tunnel-broadening. Characterization of the nonlinear light shift requires measurements over a larger range of lattice intensity.

The theoretical model including higher order contributions are required for description of results of the lattice AC Stark shift. While the electric dipole polarizability has the strongest contribution and leads to a linear dependence on lattice intensity, the influence of magnetic dipole polarizability ($\alpha^{M1}(\omega)$) and electric quadrupole polarizability ($\alpha^{E2}(\omega)$) introduce additional albeit much smaller frequency shifts. This was for the first time highlighted in 2008 [122]. The spatial and temporal behavior of the electric field of a 1D lattice can be written as

$$\mathbf{E}(\mathbf{R}, t) = 2E_0 \mathbf{e} \cos(\mathbf{k} \cdot \mathbf{R}) \cos(\omega t) \quad (5.4)$$

where E_0 is the laser field amplitude for the laser of intensity $I = |E_0|^2$, while \mathbf{k} and \mathbf{e} are the wave vector and polarization vector respectively. Using Maxwell's equation, the associated magnetic field is obtained to be

$$\mathbf{B}(\mathbf{R}, t) = 2E_0(\mathbf{n} \times \mathbf{e}) \sin(\mathbf{k} \cdot \mathbf{R}) \sin(\omega t). \quad (5.5)$$

Therefore, the magnetic-dipole interaction $\hat{V}_{M1} = -\mathbf{m} \cdot \mathbf{B}$ is out of phase with the electric dipole interaction $\hat{V}_{E1} = -\mathbf{d} \cdot \mathbf{E}$ such that at the antinodes of the lattice, electric dipole (E1) interaction is maximum while the magnetic dipole (M1) interaction is exactly zero. Here \mathbf{d} and \mathbf{m} are the electric and magnetic dipole moments respectively. Similarly, the electric quadrupole (E2) interaction depends on the gradient of the electric field and therefore has similar spatial dependence as the magnetic dipole interaction. In addition, the fourth order atom-light coupling gives rise to a I^2 dependent term. The light-atom interaction therefore produces a potential energy for an atom in the ground (excited) state as

$$U_{g(e)} = -\{\alpha_{g(e)}^{E1}(\omega) \cos^2(kX) + \alpha_{g(e)}^{qm}(\omega) \sin^2(kX)\}I - \beta_{g(e)}(\omega) \cos^4(kX)I^2, \quad (5.6)$$

where $\alpha^{qm} = \alpha^{E2} + \alpha^{M1}$ and $\beta_{g(e)}$ is the hyperpolarizability coefficient for the ground (excited) state that comes from the two-photon interactions with the atom. To simplify the analysis, the cosine and sine terms in Eq. 5.6 are expanded in a power series followed by substituting the X^2 and X^4 terms by their expectation values for an atom that occupies a vibrational state n in the harmonic oscillator like potential. This gives the total lattice AC Stark shift in the vicinity of E1 – magic frequency as[23, 123, 124]

$$\begin{aligned} h\Delta\nu_c(I, n, \delta\nu, \xi) &= c_{1/2}I^{1/2} + c_1I + c_{3/2}I^{3/2} + c_2I^2 \\ &\approx \left(\frac{\partial\Delta\alpha^{E1}}{\partial\nu} \delta\nu - \Delta\alpha^{qm} \right) (2n+1) \sqrt{\frac{E_R}{4\alpha^{E1}}} I^{1/2} \\ &\quad - \left[\frac{\partial\Delta\alpha^{E1}}{\partial\nu} \delta\nu + \Delta\beta(\xi) (2n^2 + 2n + 1) \frac{3E_R}{4\alpha^{E1}} \right] I \\ &\quad + \Delta\beta(\xi) (2n+1) \sqrt{\frac{E_R}{\alpha^{E1}}} I^{3/2} - \Delta\beta(\xi) I^2 \end{aligned} \quad (5.7)$$

where $\delta\nu$ is the lattice frequency detuning from E1-magic frequency and ξ is the polarization ellipticity of lattice light. $\Delta\alpha^{E1}$ and $\Delta\alpha^{qm}$ are the differential polarizabilities for the two clock states, while E_R is the lattice photon recoil energy.

As can be seen in Eq. 5.7, even at the E1-magic frequency, there are other frequency shift contributions that have non-zero value. Therefore, operating at the E1-magic frequency is not sufficient for clocks pushing into 10^{-17} uncertainty regimes. To see the influence of these nonlinear shifts, Eq. 5.7 is used to calculate the total AC Stark shift for the ^{24}Mg clock transition at a lattice detuning of -8 MHz

from E1-magic frequency. For these calculations, atomic parameters from [112] are used. The calculated frequency shift as a function of lattice intensity is shown in Fig. 5.5, where different regimes of intensity dependence are visible. At very low intensities, $I^{1/2}$ is the most dominant term while at intermediate intensities, linear and $I^{3/2}$ terms dominate. At the other extreme of high intensities, the frequency shift depends as I^2 on lattice intensity.

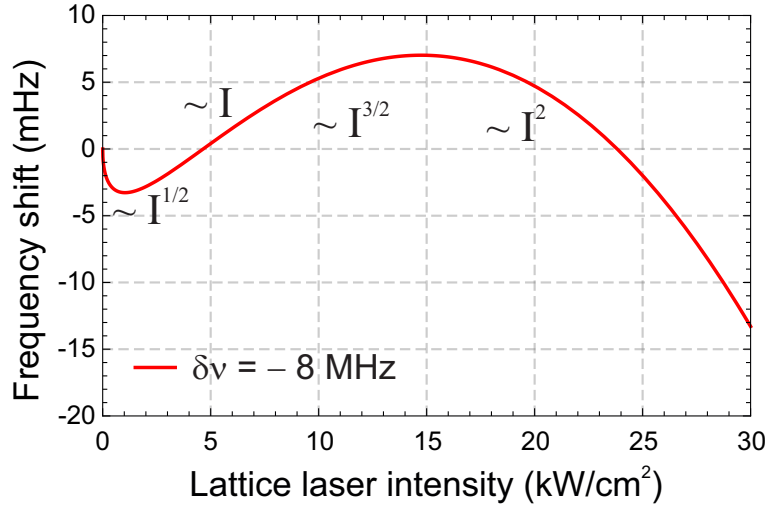


Figure 5.5: Theoretical calculation of lattice AC Stark shift for ^{24}Mg clock transition is shown here for $\delta\nu = -8$ MHz.

Another important feature of the lattice AC Stark shift dependence on intensity is visible in Fig. 5.5, where at lattice intensity of 15 kW/cm^2 , a maxima can be observed. Therefore at this intensity, to first order, there is no variation in lattice shift with a change in intensity. Such a point in lattice intensity-frequency space is what is called “operational magic condition”. In an ideal situation, by tuning the lattice frequency, such an operational magic condition can be coincided with zero frequency shift. There has been recent theoretical prediction of such an operational magic condition for magnesium where the light shift would be suppressed below 10^{-19} levels at a trap depth of $5.33 E_R$ [121]. But at such low trap depths, the tunneling induced line broadening is in the regime of tens of kHz (fractional frequencies of the order of 10^{-10}), making it impossible to ever achieve the 10^{-19} uncertainty/precision. Hence a more practical solution for operational magic condition for magnesium in deeper trap depths is needed, where though the frequency shift would be non-zero, it could still be estimated with a sufficiently high precision. The nonlinear lattice shift has been explored only in a few studies so far for Sr and Yb lattice clocks[125–127], while such studies are still missing for other clock elements.

To characterize the higher order frequency shift contributions, high precision measurements need to be performed over a very large range of lattice intensities. While

our measurement precision has significantly improved as seen in the last chapter, the requirement of varying the lattice intensity over a large intensity range was hitherto not possible since the maximum achievable lattice power was limited by the laser power available and at lower intensities, the tunneling induced line-broadening degrades our measurement precision. Therefore, the lattice laser system was again upgraded to extend the range of available lattice intensity for these measurements. The new Ti:Sa laser system³ has an output power of 3.8 W at 936 nm and therefore gives a substantial boost in the frequency doubled power at 468 nm to more than 1.5 W. However the light power at the lattice enhancement cavity was limited to below 650 mW due to Brillouin losses in the optical fiber used between the laser setup and the enhancement cavity setup. Nevertheless, with 650 mW of input power, up to 17 W of circulating light power is generated in the lattice enhancement cavity. With a lattice waist in the 45 – 65 μm regime, these optical powers correspond to trap depths up to 130 E_R . Therefore, a large range of lattice trap depth becomes available where tunneling induced line-broadening remains below the Fourier line-broadening expected from spectroscopy pulse duration.

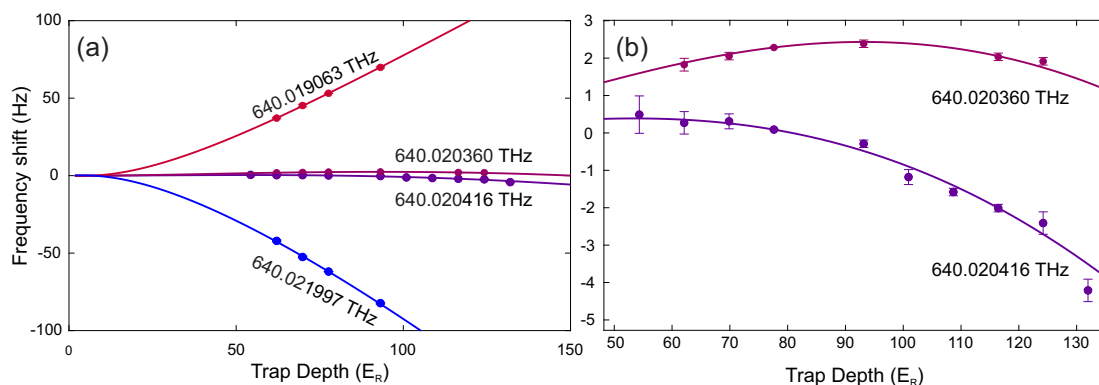


Figure 5.6: (a) Lattice AC Stark shift measurements performed over a large range of trap depth is shown here. A nonlinear regression method is used to fit the model from Eq. 5.7 to the experimental data. The measurements far away from E1-magic frequency helps in better characterization of α^{E1} while the data close to E1-magic frequency gives a more clear view of nonlinear lattice shift contribution. (b) The two measurement sets for the lattice frequencies close to E1-magic frequency clearly show the non-linear behavior of the lattice light shift.

A set of lattice frequency shift measurement data with the upgraded lattice setup is shown in Fig. 5.6, where the measurement close to magic frequency clearly shows a deviation from linear intensity dependence (Fig. 5.6(b)). The complete dataset for different lattice frequencies has been simultaneously fitted with a nonlinear regression model based on Eq. 5.7 where an effective thermal reduction in trap depth (due to distribution of atoms along transverse axes in the lattice) has also been taken into account[127]. In contrast to the dipole- and hyper-polarizability contributions, the multipolar polarizability α^{qm} contribution only has $I^{1/2}$ dependence on lattice intensity. Therefore at large lattice intensities required to trap the atoms

³SOLSTIS from M Squared

deep in Lamb-Dicke regime, the multipolar frequency shift is much smaller than the other polarizability contributions. Therefore the theoretical value of $\Delta\alpha^{\text{qm}}$ from [112] was used in the theoretical model to estimate the other parameters. The values of fit parameters remained well within the uncertainties even for an order of magnitude variation in α^{qm} . The light shift parameters thus obtained from the numerical fitting are as follows:

$$\begin{aligned} \nu_{\text{E1-magic}} &= 640\,020\,484(40)\text{MHz} \\ \frac{\partial\Delta\alpha^{\text{E1}}}{\partial\nu} &= 0.51(8) \times 10^{-9} \text{ Hz/Hz/kWcm}^{-2} \\ \Delta\beta &= 925(375) \mu\text{Hz}/E_{\text{R}}^2 = 197(80) \mu\text{Hz}/(\text{kWcm}^{-2})^2. \end{aligned} \quad (5.8)$$

The large uncertainty in parameter values comes from the statistical uncertainty due to limited measurement data as well as the large atomic temperature uncertainty. The latter effect is in particular hard to estimate due to high atomic temperature itself, which makes the analysis of sideband scans imprecise. The high temperatures also indicate significant occupation of higher Bloch bands with much larger bandwidths. This further increases the uncertainty of their contribution to the carrier lineshape. Therefore as a conservative approach, a larger uncertainty of the parameters is taken assuming an average state occupation of $n_z = 1$ and radial temperature $T_r = 100 \mu\text{K}$ with an uncertainty $\Delta n_z = 1$ and $\Delta T_r = 50 \mu\text{K}$.

To characterize multipolar polarizability α^{qm} , measurement of frequency shift for different Bloch band occupation can be used [127]. However, the high atomic temperatures in our experiment currently make it hard to selectively populate the individual Bloch bands. It would be interesting to perform these measurements with a more stable probe laser system such that higher Bloch bands are resolved due to larger line broadening. This could enable an estimation of lattice shift parameters, opening the possibility of resolving multipolar polarizability effects.

The measurement data shown in Fig. 5.6 can be used as a calibration of the lattice light shift dependence on the circulating lattice power, and therefore to estimate the lattice shift for given lattice parameters. For such a calibration method, the frequency shift obtained from the data fitting at trap depth of $56 E_{\text{R}}$ is $0.5(4) \text{ Hz}$ for $\nu_{\text{lattice}} = 640\,020\,416 \text{ MHz}$. We again assume here that the mean vibrational state occupancy is $n_z = 1$, with an uncertainty $\Delta n_z = 1$ and the radial temperature is $T_r = 100(50)\mu\text{K}$. These large thermal uncertainties lead to the 0.4 Hz shift uncertainty. This corresponds to a fractional frequency uncertainty of 6.1×10^{-16} . Assuming the multipolar polarizability value to be uncertain by a factor of three around the theoretically predicted value, an additional uncertainty of 0.09 Hz is introduced. For this method to work, repeatability of the lattice frequency measurement has to be ensured. In our current setup, we stabilize the lattice laser

frequency by locking the Ti:Sa laser frequency to the clock laser frequency via a transfer cavity. While this does not provide an accurate measurement of lattice frequency, it is possible to ensure repeatability by locking the laser frequencies to the same resonator modes. For such a frequency stabilization scheme, the long term frequency shifts are dominated by the residual amplitude modulation (RAM). Assuming a worse case RAM of 10^6 ppm, such a transfer lock scheme ensures long term frequency fluctuations below 1 MHz. This frequency instability would contribute an additional uncertainty of 0.06 Hz. Therefore combining these three frequency shift contributions, the total uncertainty of the lattice light shift would be 6.5×10^{-16} .

5.5 Summary

In this chapter, details of clock systematic shift measurements were discussed. The frequency shifts and associated uncertainties are summarized in Table 5.1. It is encouraging to note that the shift uncertainty for the probe AC Stark shift as well as the Zeeman shift has been lowered to the 10^{-17} regime, while the density shift is in low 10^{-16} regime. Perhaps a trade-off for the density shift can be performed where the atom loading time can be reduced, leading to lower atom numbers in the lattice and a lower shift. Indeed this would negatively impact the clock instability, but the reduction in cycle time and increase of duty cycle could compensate for this increased instability to some extent. On the other hand, with the recent upgrade of our triplet MOT laser system, we should be able to significantly enhance atom loading rate to the lattice as well as the fluorescence signal during detection. This would increase the precision of density shift measurement while also allowing operating the clock at lower atom numbers, leading to significant improvement in density shift uncertainty.

	Correction (10^{-17})	Uncertainty (10^{-17})
Probe AC Stark shift	482.4	6.1
Quadratic Zeeman shift	3556.9	6.3
Density shift	6.1	13.7
Lattice AC Stark shift	76.3	64.8

Table 5.1: Summary of the dominant frequency shifts and their uncertainties influencing our magnesium lattice clock.

The uncertainty of the probe AC Stark shift and Zeeman shift can be significantly improved by upgrading our probe laser setup. Currently the probe laser frequency instability limits the maximum spectroscopy pulse time and hence requires much larger probe light and magnetic fields to generate correspondingly large Rabi frequency. This leads to large frequency shifts as well. Even if the spectroscopy

pulse duration can be improved from currently used value of 200 ms to 400 ms, the frequency shifts can be reduced by a factor half and hence a reduction in shift uncertainties by a factor half as well. This was also the technique used recently to improve performance of a bosonic Sr lattice clock [22]. In fact, with lower probe laser instability, even higher line-Q can be achieved, leading to further improvement of clock instability and the accuracy.

The only frequency shift contribution that still remains large and difficult to measure is the lattice AC Stark shift. Though a detailed characterization of lattice shift was performed for our magnesium lattice clock, the requirements of large lattice intensities leads to high uncertainty of associated AC Stark shift, further exacerbated by large atomic temperatures as well as uncertainty in lattice frequency measurement. However, these issues can be significantly improved upon to reduce uncertainty to 10^{-16} regime, as discussed in previous section. Therefore in the short term, the magnesium clock transition frequency can be measured with an uncertainty in 10^{-16} regime, while further work towards lattice frequency measurement and characterization of higher order shifts would be required to reduce the uncertainty to 10^{-17} regime.

Outlook

In the framework of this thesis, detailed modeling of Bloch band spectroscopy was performed to better understand the line-broadening and asymmetry features for spectroscopy in shallow lattice at and around the magic wavelength. To improve the clock performance, the optical lattice system was upgraded to alleviate some of the issues affecting the previous frequency measurement campaign. This reduced the magnesium clock transition linewidth to Hz regime for the first time, opening the possibility of reaching clock uncertainty in the 10^{-17} regime. The magnesium clock instability was for the first time reduced to 10^{-17} regime within a few thousand seconds of averaging. To enable an improved frequency measurement, most of the dominant systematic shifts were characterized with an uncertainty in mid- 10^{-17} to low- 10^{-16} regime. For better estimation of the lattice AC Stark shift, higher order shift contributions were also studied for the first time for magnesium, providing the first experimental estimate of the differential hyperpolarizability shift coefficient. These developments place our experiment in a good position to perform a significantly improved frequency measurement campaign in near future. In this chapter, a discussion on current system limitations and possible methods to improve on them will also be discussed.

6.1 Cooling on the intercombination transition

Cooling magnesium to μK regime has not been possible so far. This is in stark contrast to the other major lattice clock candidates such as Sr and Yb, where

direct Doppler cooling to a few μK temperature has been possible since many years. While the ultra-violet laser wavelengths needed for Doppler cooling has also been a challenge for magnesium, the bigger difference lies in the transition linewidths of the cooling transitions. While $^1\text{S}_0 - ^1\text{P}_1$ and $^3\text{P}_2 - ^3\text{D}_3$ transitions have very large linewidths which limit Doppler cooling to the mK regime, the $^1\text{S}_0 - ^3\text{P}_1$ intercombination transition has a linewidth of only 36 Hz, which makes it inefficient for Doppler cooling as well. So far, we work around this problem by generating a large flux of mK cold atoms in a two-stage MOT followed by energy filtering in the far detuned dipole trap. To achieve a narrow thermal distribution in the lattice, perhaps other cooling schemes need to be utilized. One such scheme of quenched sideband cooling can be useful to reduce the temperature in the lattice. The other promising cooling method for magnesium is the sawtooth wave adiabatic passage (SWAP) cooling recently proposed and demonstrated for Sr [128].

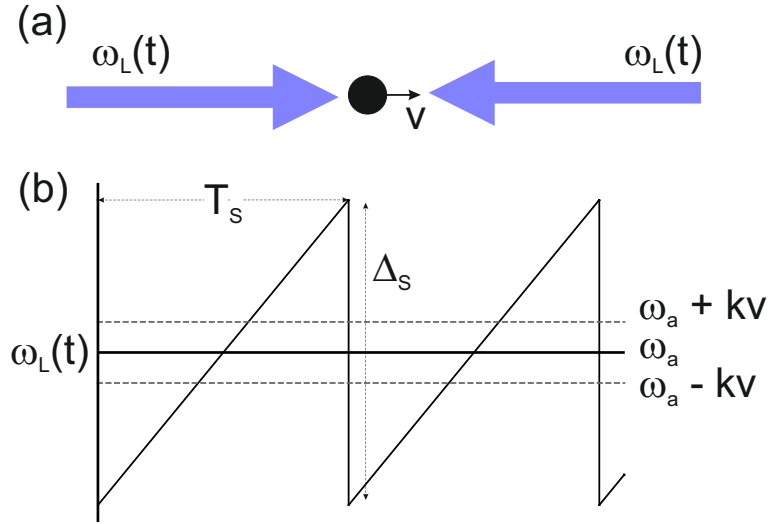


Figure 6.1: SWAP cooling scheme: (a) The atom moving with velocity v interacts with two counter-propagating laser beams with instantaneous frequency $\omega_L(t)$, where (b) the laser frequency is linearly ramped up from far negative detuning to a large positive detuning with a total sweep range of Δ_s in time T_s and then reset back to negative detuning. The moving atom in ground state absorbs a photon from the laser beam counter-propagating to its motion and then emits a photon in the co-propagating laser beam via stimulated emission process. Therefore the kinetic energy of moving atom is reduced by twice the photon recoil energy.

The 36 Hz intercombination transition is well suited for implementing the SWAP cooling, where stimulated absorption and emission processes play a stronger role in velocity reduction compared to Doppler cooling technique. The spontaneous emission events are only needed to randomize the atomic velocities and therefore to reduce entropy. The SWAP cooling scheme as shown in Fig. 6.1 works by sweeping the frequency ω_L of counter-propagating lasers from large negative detuning to large positive detuning around the atomic resonance frequency ω_a , followed by a sharp jump back to the initial frequency as in a sawtooth wave pattern. An atom

moving with velocity v first absorbs a photon from the counter propagating laser beam at a red detuned frequency of $\omega_a - kv$, where k is the photon recoil. This is followed by a photon emission stimulated by the co-propagating laser beam at frequency $\omega_a + kv$. Both these absorption and emission events lead to photon recoils against atomic velocity, hence reducing the kinetic energy by two photon recoil energy. This is in contrast to Doppler cooling where the photon emission is a spontaneous process. In addition, the velocity range where cooling occurs is tunable by tuning the frequency sweep range Δ_s . This gives SWAP cooling the dual advantage of giving larger photon recoil against the atomic velocity per absorption cycle as well as a more efficient and faster cooling on otherwise narrow atomic transitions. Due to a heavy reliance on stimulated emission, this technique works better for narrow atomic transitions.

It is interesting to compare the SWAP cooling technique with the Raman cooling technique [129], where frequency detuning between two counter-propagating Raman pulses is varied (depending on the Doppler shift of the targeted velocity class) to excite specific velocity classes from ground state $|g\rangle$ to the excited hyperfine state $|e\rangle$. Afterwards a single laser pulse excites the atoms from $|e\rangle$ to a higher lying state from where atoms spontaneously decay to the ground state $|g\rangle$ and complete the cooling process by randomizing the velocities and resetting the atom to the ground state. In SWAP cooling, the spontaneous event is not needed in every cycle since it is only needed to thermalize the atoms, which requires far fewer spontaneous events.

For SWAP cooling to work effectively, three conditions need to be satisfied:

$$\begin{aligned}\Omega &\gg \gamma \\ \alpha &\lesssim \Omega^2 \\ \alpha/2kv &\gtrsim \gamma\end{aligned}\tag{6.1}$$

where γ is the spontaneous decay rate from 3P_1 to 1S_0 state, Ω is the Rabi frequency and α is the frequency sweep rate for the sawtooth frequency ramp. The first two conditions ensure the requirement to be in an Adiabatic state transfer regime. The third condition constraints the sweep rate such that there are no spontaneous emission events between the two adiabatic interaction processes during one frequency sweep.

With a spontaneous decay rate of $2\pi \times 36$ Hz for the magnesium intercombination transition, these conditions are easily satisfied for an initial temperature of 50 μ K. Though this technique relies much less on spontaneous emission, it still requires the spontaneous emissions to initiate the atoms in ground state at the beginning of every sweep. Since the 3P_1 state has a very large lifetime of 4.4 ms, this could still limit the cooling time and therefore lead to atom loss during the cooling process.

These losses can be avoided by performing SWAP cooling in an optical dipole trap, though the physics of cooling changes in a dipole trap due to a dependence of atomic velocity on the atom's position in the trap. However, this technique offers the possibility to cool the atomic temperature to below 10 μK , which would significantly improve the fraction of atoms in the lowest Bloch band.

6.2 Suppressing tunneling induced broadening

Tunneling induced line broadening can most straightforwardly be decreased by increasing the lattice intensity. But that leads to an increase in lattice light shift uncertainty, particularly from the higher order light shifts. Therefore, new methods to suppress tunneling [130, 131], and new spectroscopy techniques to suppress tunneling induced line broadening need to be explored. One such technique increases the effective lattice spacing [132] with respect to spectroscopy laser wavelength. We focus here on this technique and outline the experimental design suitable for our experiment.

For a lattice generated by light beams of wavelength λ_{magic} interfering at an angle θ , the effective lattice spacing a is given as

$$a = \lambda_{\text{magic}} / |2 \sin(\theta/2)|. \quad (6.2)$$

For a typical optical lattice generated by interfering a laser beam with its retro-reflected copy or in a linear cavity, $\theta = 180^\circ$, and therefore $a_0 = \lambda_{\text{magic}}/2$. However, by selecting smaller θ values, the lattice spacing can be increased significantly [133, 134].

The tunneling rate dependence on the lattice spacing a is given as

$$\frac{t(a)}{t(a_0)} = \sqrt{\frac{a_0}{a}} \exp \left[\sqrt{\frac{U_0}{E_R}} \left(1 - \frac{a}{a_0} \right) \right]. \quad (6.3)$$

Such an exponential dependence on lattice spacing allows for a strong control on tunneling rate by changing θ . This can be seen in the Fig. 6.2, where tunneling induced line-broadening is shown as a function of θ for a lattice depth of $10 E_R$. While the linewidth for a lattice with $\theta = 180^\circ$ is in kHz regime, it reduces to sub-Hz regime as θ is lowered below 60° with an exponential dependence as predicted in Eq. 6.3.

The sharp resonant features in Fig 6.2 appear when $a/\lambda_{\text{clock}} \bmod 1 = 0$. At these conditions, the lattice spacing exactly matches multiples of probe laser wavelength. Therefore, the photon recoil momentum absorbed during excitation is an integer

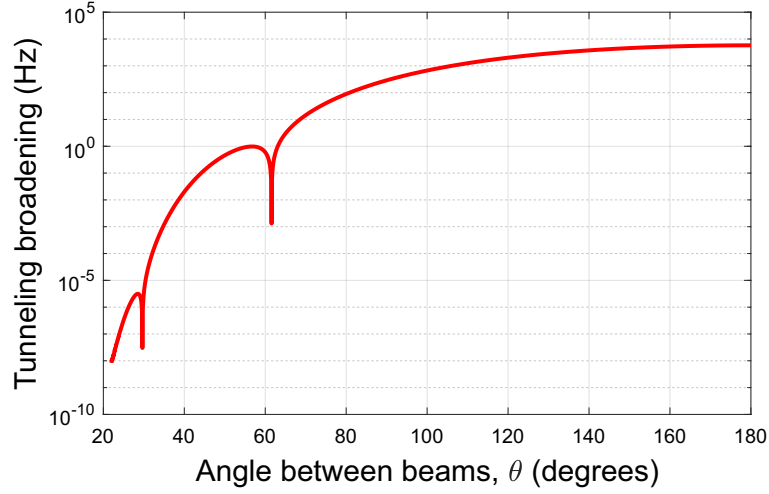


Figure 6.2: Tunneling induced line broadening as a function of the angle between lattice beams θ for a trap depth of $U_0 = 10 E_R$

multiple of the Brillouin zone width, leading to zero frequency shift. While operating at these conditions may be tempting, the required tolerance on the angle deviations makes it much more complicated.

Along with a change in effective lattice spacing, varying θ also leads to change in trap radius along and perpendicular to lattice axis. The radii along the lattice axis \tilde{w}_{0z} and in transverse axis \tilde{w}_{0x} of the overlapping region between the two beams:

$$\begin{aligned}\tilde{w}_{0x} &= \sqrt{\frac{1}{\frac{\cos^2(\theta/2)}{w_{0x}^2} + \frac{\sin^2(\theta/2)}{2z_R^2}}} \\ \tilde{w}_{0z} &= \sqrt{\frac{1}{\frac{\sin^2(\theta/2)}{w_{0x}^2} + \frac{\cos^2(\theta/2)}{2z_R^2}}},\end{aligned}\tag{6.4}$$

where w_{0x} is the waist of interfering beams and z_R is the associated Rayleigh range. As expected, the radius along the lattice axis reduces to the incident beam waist when the angle between the beams is zero, while it is equal to z_R for counter-propagating beams.

In Fig. 6.3, \tilde{w}_{0z} and \tilde{w}_{0x} are shown as a function of the angle between the two incident laser beams. For trapping large number of atoms in the lattice at low densities, a large \tilde{w}_{0z} and a small \tilde{w}_{0x} is desired, which occurs optimally at $\theta = 180^\circ$. However, a trade-off between reduction in tunneling induced line broadening and optimal overlap region dimensions is required. The most interesting regime for operating the clock from this trade-off is at $\theta = 60^\circ$, where the tunneling induced line-broadening is reduced to sub-Hz regime even for $10 E_R$ deep lattice, while

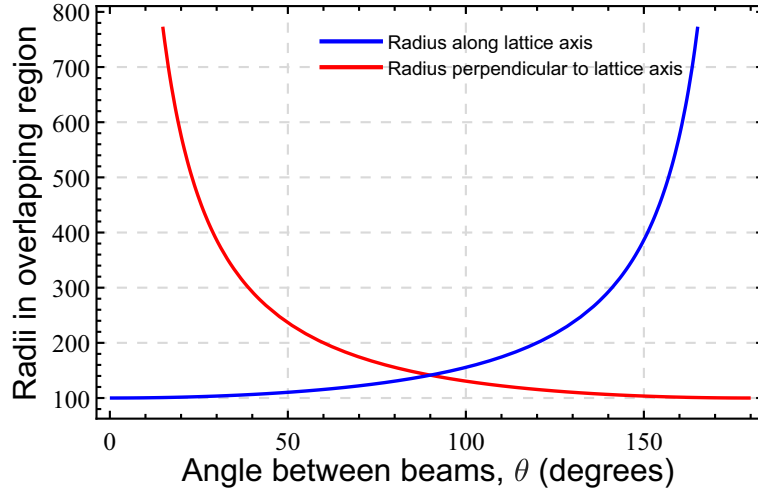


Figure 6.3: The radius along the lattice axis and transverse axis is shown here for two incident beams with $100\mu\text{m}$ waists interfering at angle θ . At the design angle of 60° , the radius along the lattice axis is $115\mu\text{m}$ and $200\mu\text{m}$ in the transverse axis.

still allowing for a large capture area. As can be seen in Fig. 6.4, at $\theta = 60^\circ$, the tunneling induced line-broadening for the lowest vibrational state is reduced to sub-Hz regime even for $U_0 = 10 E_R$, while for $\theta = 180^\circ$, the line-broadening is more than 4 orders of magnitude larger.

To operate the lattice at $10 E_R$ with $100\mu\text{m}$ beam waist, only 3 W optical power is required in each interfering laser beam. As already shown in this thesis, more than five times as large optical powers can be achieved in an enhancement cavity. However, given the required angle between the two beams, a bow-tie cavity design as shown in Fig. 6.5 would be much more appropriate compared to the linear design used so far in our experiment.

The complete cavity system can be placed inside the vacuum to avoid any loss of cavity finesse from the vacuum chamber viewports. In addition, the cavity center region can easily be overlapped with a crossed 1064 nm optical dipole trap to transfer the atoms from the MOT to the lattice. This design can significantly reduce the system complexity compared to our existing lattice cavity, where intra-cavity mirrors are required to overlap the spectroscopy laser and the 1064 nm dipole laser with the optical lattice.

As already stated, a big motivation for operating in shallow lattice is to reduce the higher order lattice Stark shift contribution. At the trap depth of $10 E_R$ with $100\mu\text{m}$ waist, the hyperpolarizability induced light shift is only $0.8(3)\text{ Hz}$ according to our measured hyperpolarizability shift coefficient. Due to low tunneling rates even at such low lattice intensities, lattice shift calibration can be performed over a large lattice intensity range. For example, comparing the frequency shift between

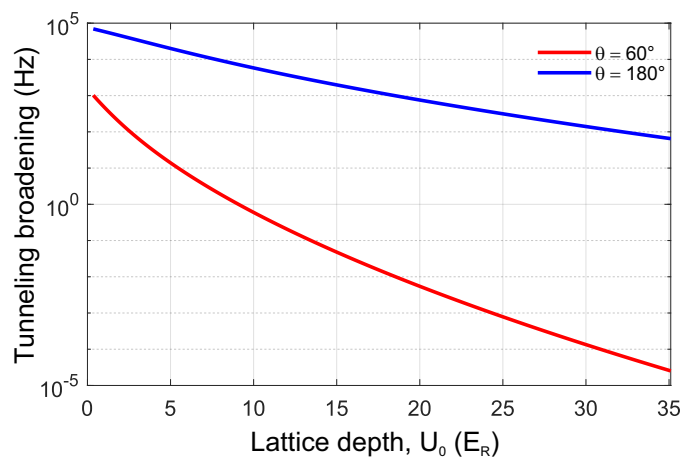


Figure 6.4: Tunneling induced line-broadening is shown here for the lowest vibrational state in a lattice generated by overlapping the two beams at an angle of $\theta = 60^\circ$ (red) and $\theta = 180^\circ$ (blue) as a function of trap depth.

lattice of $10 E_R$ and $50 E_R$ (which is feasible given that intra-cavity power up to 15 W can be realized) with an uncertainty of 10^{-16} would allow for an estimation of hyperpolarizability induced quadratic shift with an uncertainty $\frac{1 \times 10^{-16}}{24}$, well in the 10^{-18} regime. In fact, possibility of operating the lattice system at such low trap depths could also make it possible to reach the operational magic condition with zero lattice light shift [121].

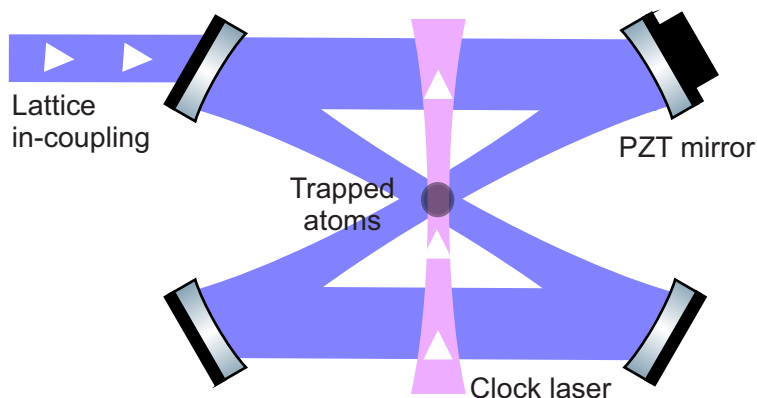


Figure 6.5: Bow-tie cavity design with $\theta = 60^\circ$ to generate magic wavelength lattice. The laser polarization needs to be s-polarized to generate interference in the overlap region.

6.3 Enhancing the clock duty cycle

One of the difficulties in significantly improving the magnesium clock instability is associated with the requirement of relatively large cooling and state preparation time, which makes the clock cycle time T_c very large. Though this issue can be somewhat alleviated by using a more stable spectroscopy laser which would allow longer interrogation time T_s and thereby increasing the duty cycle $D = T_s/T_c$, a better strategy is needed for the future where additional sideband cooling steps may further increase the state-preparation time.

One approach to increase clock duty cycle that has already been studied in other lattice clock experiments is to use non-destructive state detection, whereby recycling the atoms trapped in the lattice. It is important to note that the clock spectroscopy does not lead to any heating, since there is no spontaneous emission process taking place during clock spectroscopy. There are atom losses due to background gas collisions and heating from lattice intensity fluctuations, but these can be reduced by technical improvements to the experiment. Hence, atoms once loaded into the lattice can be repeatedly used to perform spectroscopy as long as the state detection does not lead to any additional heating. This is exactly where non-destructive detection process can be useful. The essential idea behind non-destructive detection process is to read out the atom number signal by coupling their population in an atomic state to the dispersion induced phase shifts for a off-resonant laser beam [135]. This is most efficiently achieved using cavity modes [136, 137]. For magnesium, the $^1S_0 - ^1P_1$ transition with a large decay rate of $\Gamma = 2\pi \times 78$ MHz would be suited for this detection technique. However, making high finesse cavities for light frequency around this 285 nm transition would be incredibly challenging, considering the degradation of mirror coatings with time for such low laser wavelengths.

A more pragmatic approach for magnesium would be to operate the lattice in a quasi-continuous loading scheme, where the atoms would be cooled and trapped in the 1064 nm trap elsewhere and after each spectroscopy and detection cycle, transferred to the lattice. This approach becomes especially appealing once spectroscopy pulse time is increased to more than 1 second, providing sufficient time to load a large number of atoms in the 1064 nm trap. Such a design would in fact allow for implementing the bow-tie cavity lattice as an add-on component to one of the CF Flanges of our existing science chamber. The idea would be to trap the atoms in our already existing dipole trap, and transport them by moving the focus position to overlap with the lattice region. During the spectroscopy cycle, the 1064 nm light can be blocked by a combination of motorized beam deflector for diverting the laser to a beam dump and optical shutter for blocking any remaining stray light. Such a continuous clock operation scheme would provide considerable

gains over the current system. Improving the duty cycle by a factor 5 would allow the clock instability to reach 10^{-18} regime in a few thousand seconds of averaging time.

Bibliography

- [1] L. Essen and J. V. L. Parry.
An atomic standard of frequency and time interval.
Nature, 176, 1955.
4
- [2] J Terrien.
News from the international bureau of weights and measures.
Metrologia, 4(1):41–45, jan 1968.
doi: 10.1088/0026-1394/4/1/006.
4
- [3] The Event Horizon Telescope Collaboration.
First m87 event horizon telescope results. i. the shadow of the supermassive
black hole.
The Astrophysical Journal Letters, 875(1):L1, April 2019.
doi: 10.3847/2041-8213/ab0ec7.
4
- [4] H. Schnatz, B. Lipphardt, J. Helmcke, F. Riehle, and G. Zinner.
First phase-coherent frequency measurement of visible radiation.
Phys. Rev. Lett., 76:18–21, Jan 1996.
doi: 10.1103/PhysRevLett.76.18.
4
- [5] Scott A. Diddams, David J. Jones, Jun Ye, Steven T. Cundiff, John L. Hall,
Jinendra K. Ranka, Robert S. Windeler, Ronald Holzwarth, Thomas
Udem, and T. W. Hänsch.
Direct link between microwave and optical frequencies with a 300 thz fem-
tosecond laser comb.
Phys. Rev. Lett., 84:5102–5105, May 2000.
doi: 10.1103/PhysRevLett.84.5102.
4, 36

-
- [6] R. Holzwarth, Th. Udem, T. W. Hänsch, J. C. Knight, W. J. Wadsworth, and P. St. J. Russell.
Optical frequency synthesizer for precision spectroscopy.
Phys. Rev. Lett., 85:2264–2267, Sep 2000.
doi: 10.1103/PhysRevLett.85.2264.
4, 36
- [7] Theodor W. Hänsch.
Nobel lecture: Passion for precision.
Rev. Mod. Phys., 78:1297–1309, Nov 2006.
doi: 10.1103/RevModPhys.78.1297.
4
- [8] John L. Hall.
Nobel lecture: Defining and measuring optical frequencies.
Rev. Mod. Phys., 78:1279–1295, Nov 2006.
doi: 10.1103/RevModPhys.78.1279.
4
- [9] J. L. Hall, T. Baer, L. Hollberg, and H. G. Robinson.
Precision spectroscopy and laser frequency control using fm sideband optical heterodyne techniques.
In A. Robert W. McKellar, Takeshi Oka, and Boris P. Stoicheff, editors,
Laser Spectroscopy V, pages 15–24, Berlin, Heidelberg, 1981. Springer
Berlin Heidelberg.
5
- [10] P. W. Smith and R. Hänsch.
Cross-relaxation effects in the saturation of the 6328-Å neon-laser line.
Phys. Rev. Lett., 26:740–743, Mar 1971.
doi: 10.1103/PhysRevLett.26.740.
5
- [11] R. H. Dicke.
The effect of collisions upon the doppler width of spectral lines.
Phys. Rev., 89:472–473, Jan 1953.
doi: 10.1103/PhysRev.89.472.
5, 15
- [12] T. Rosenband, D. B. Hume, P. O. Schmidt, C. W. Chou, A. Brusch, L. Lorini, W. H. Oskay, R. E. Drullinger, T. M. Fortier, J. E. Stalnaker, S. A. Diddams, W. C. Swann, N. R. Newbury, W. M. Itano, D. J. Wineland, and J. C. Bergquist.

- Frequency ratio of al^+ and hg^+ single-ion optical clocks; metrology at the 17th decimal place.
Science, 319(5871):1808–1812, 2008.
doi: 10.1126/science.1154622.
5, 9, 10
- [13] J. Keller, T. Burgermeister, D. Kalincev, A. Didier, A. P. Kulosa, T. Nordmann, J. Kiethe, and T. E. Mehlstäubler.
Controlling systematic frequency uncertainties at the 10^{-19} level in linear coulomb crystals.
Phys. Rev. A, 99:013405, Jan 2019.
doi: 10.1103/PhysRevA.99.013405.
5
- [14] Kyle Arnold, Elnur Hajiyev, Eduardo Paez, Chern Hui Lee, M. D. Barrett, and John Bollinger.
Prospects for atomic clocks based on large ion crystals.
Phys. Rev. A, 92:032108, Sep 2015.
doi: 10.1103/PhysRevA.92.032108.
5
- [15] W. M. Itano, J. C. Bergquist, J. J. Bollinger, J. M. Gilligan, D. J. Heinzen, F. L. Moore, M. G. Raizen, and D. J. Wineland.
Quantum projection noise: Population fluctuations in two-level systems.
Phys. Rev. A, 47:3554–3570, May 1993.
doi: 10.1103/PhysRevA.47.3554.
6
- [16] Hidetoshi Katori, Tetsuya Ido, and Makoto Kuwata-Gonokami.
Optimal design of dipole potentials for efficient loading of sr atoms.
Journal of the Physical Society of Japan, 68(8):2479–2482, 1999.
doi: 10.1143/JPSJ.68.2479.
6, 24
- [17] U. Sterr, T. Legero, T. Kessler, H. Schnatz, G. Grosche, O. Terra, and F. Riehle.
Ultrastable lasers: new developments and applications.
In Tetsuya Ido and Derryck T. Reid, editors, *Time and Frequency Metrology II*, volume 7431, pages 33 – 46. International Society for Optics and Photonics, SPIE, 2009.
6
- [18] Garrett D. Cole, Wei Zhang, Michael J. Martin, Jun Ye, and Markus Aspelmeyer.

- Tenfold reduction of brownian noise in high-reflectivity optical coatings.
Nature Photonics, 7(8):644–650, Aug 2013.
doi: 10.1038/nphoton.2013.174.
6, 33
- [19] W. Zhang, M. J. Martin, C. Benko, J. L. Hall, J. Ye, C. Hagemann, T. Legero, U. Sterr, F. Riehle, G. D. Cole, and M. Aspelmeyer.
Reduction of residual amplitude modulation to 1×10^{-6} for frequency modulation and laser stabilization.
Opt. Lett., 39(7):1980–1983, Apr 2014.
doi: 10.1364/OL.39.001980.
6
- [20] D. G. Matei, T. Legero, S. Häfner, C. Grebing, R. Weyrich, W. Zhang, L. Sonderhouse, J. M. Robinson, J. Ye, F. Riehle, and U. Sterr.
1.5 μm lasers with sub-10 mhz linewidth.
Phys. Rev. Lett., 118:263202, Jun 2017.
doi: 10.1103/PhysRevLett.118.263202.
6
- [21] William R. Milner, John M. Robinson, Colin J. Kennedy, Tobias Bothwell, Dhruv Kedar, Dan G. Matei, Thomas Legero, Uwe Sterr, Fritz Riehle, Holly Leopardi, Tara M. Fortier, Jeffrey A. Sherman, Judah Levine, Jian Yao, Jun Ye, and Eric Oelker.
Demonstration of a timescale based on a stable optical carrier.
Phys. Rev. Lett., 123:173201, Oct 2019.
doi: 10.1103/PhysRevLett.123.173201.
6
- [22] S. Origlia, M. S. Pramod, S. Schiller, Y. Singh, K. Bongs, R. Schwarz, A. Al-Masoudi, S. Dörscher, S. Herbers, S. Häfner, U. Sterr, and Ch. Lisdat.
Towards an optical clock for space: Compact, high-performance optical lattice clock based on bosonic atoms.
Phys. Rev. A, 98:053443, Nov 2018.
doi: 10.1103/PhysRevA.98.053443.
6, 28, 86
- [23] Hidetoshi Katori, V. D. Ovsiannikov, S. I. Marmo, and V. G. Palchikov.
Strategies for reducing the light shift in atomic clocks.
Phys. Rev. A, 91:052503, May 2015.
doi: 10.1103/PhysRevA.91.052503.
6, 81
- [24] Tobias Bothwell, Dhruv Kedar, Eric Oelker, John M Robinson, Sarah L Bromley, Weston L Tew, Jun Ye, and Colin J Kennedy.

- JILA SrI optical lattice clock with uncertainty of 2.0×10^{-18} .
Metrologia, 56(6):065004, oct 2019.
doi: 10.1088/1681-7575/ab4089.
7, 9
- [25] K. Beloy, N. Hinkley, N. B. Phillips, J. A. Sherman, M. Schioppo, J. Lehman, A. Feldman, L. M. Hanssen, C. W. Oates, and A. D. Ludlow.
Atomic clock with 1×10^{-18} room-temperature blackbody stark uncertainty.
Phys. Rev. Lett., 113:260801, Dec 2014.
doi: 10.1103/PhysRevLett.113.260801.
7
- [26] Ichiro Ushijima, Masao Takamoto, Manoj Das, Takuya Ohkubo, and Hidetoshi Katori.
Cryogenic optical lattice clocks.
Nature Photonics, 9(3):185–189, Mar 2015.
doi: 10.1038/nphoton.2015.5.
7
- [27] Jacopo Grotti, Silvio Koller, Stefan Vogt, Sebastian Häfner, Uwe Sterr, Christian Lisdat, Heiner Denker, Christian Voigt, Ludger Timmen, Antoine Rolland, Fred N. Baynes, Helen S. Margolis, Michel Zampaolo, Pierre Thoumany, Marco Pizzocaro, Benjamin Rauf, Filippo Bregolin, Anna Tampellini, Piero Barbieri, Massimo Zucco, Giovanni A. Costanzo, Cecilia Clivati, Filippo Levi, and Davide Calonico.
Geodesy and metrology with a transportable optical clock.
Nature Physics, 14(5):437–441, May 2018.
doi: 10.1038/s41567-017-0042-3.
7
- [28] S. Kolkowitz, S. L. Bromley, T. Bothwell, M. L. Wall, G. E. Marti, A. P. Koller, X. Zhang, A. M. Rey, and J. Ye.
Spin-orbit-coupled fermions in an optical lattice clock.
Nature, 542(7639):66–70, Feb 2017.
doi: 10.1038/nature20811.
7, 48
- [29] N. Huntemann, B. Lipphardt, Chr. Tamm, V. Gerginov, S. Weyers, and E. Peik.
Improved limit on a temporal variation of m_p/m_e from comparisons of yb^+ and cs atomic clocks.
Phys. Rev. Lett., 113:210802, Nov 2014.
doi: 10.1103/PhysRevLett.113.210802.
7

- [30] Marianna S. Safronova.
The search for variation of fundamental constants with clocks.
Annalen der Physik, 531(5):1800364, 2019.
doi: <https://doi.org/10.1002/andp.201800364>.
7
- [31] Colin J. Kennedy, Eric Oelker, John M. Robinson, Tobias Bothwell, Dhruv Kedar, William R. Milner, G. Edward Marti, Andrei Derevianko, and Jun Ye.
Precision metrology meets cosmology: Improved constraints on ultralight dark matter from atom-cavity frequency comparisons.
Phys. Rev. Lett., 125:201302, Nov 2020.
doi: [10.1103/PhysRevLett.125.201302](https://doi.org/10.1103/PhysRevLett.125.201302).
7
- [32] S. Kolkowitz, I. Pikovski, N. Langellier, M. D. Lukin, R. L. Walsworth, and J. Ye.
Gravitational wave detection with optical lattice atomic clocks.
Phys. Rev. D, 94:124043, Dec 2016.
doi: [10.1103/PhysRevD.94.124043](https://doi.org/10.1103/PhysRevD.94.124043).
7
- [33] V. I. Yudin, A. V. Taichenachev, C. W. Oates, Z. W. Barber, N. D. Lemke, A. D. Ludlow, U. Sterr, Ch. Lisdat, and F. Riehle.
Hyper-ramsey spectroscopy of optical clock transitions.
Phys. Rev. A, 82:011804, Jul 2010.
doi: [10.1103/PhysRevA.82.011804](https://doi.org/10.1103/PhysRevA.82.011804).
7
- [34] N. Huntemann, B. Lipphardt, M. Okhapkin, Chr. Tamm, E. Peik, A. V. Taichenachev, and V. I. Yudin.
Generalized ramsey excitation scheme with suppressed light shift.
Phys. Rev. Lett., 109:213002, Nov 2012.
doi: [10.1103/PhysRevLett.109.213002](https://doi.org/10.1103/PhysRevLett.109.213002).
- [35] T. Zanon-Willette, V. I. Yudin, and A. V. Taichenachev.
Generalized hyper-ramsey resonance with separated oscillating fields.
Phys. Rev. A, 92:023416, Aug 2015.
doi: [10.1103/PhysRevA.92.023416](https://doi.org/10.1103/PhysRevA.92.023416).
- [36] R. Hobson, W. Bowden, S. A. King, P. E. G. Baird, I. R. Hill, and P. Gill.
Modified hyper-ramsey methods for the elimination of probe shifts in optical clocks.
Phys. Rev. A, 93:010501, Jan 2016.
doi: [10.1103/PhysRevA.93.010501](https://doi.org/10.1103/PhysRevA.93.010501).

-
- [37] Christian Sanner, Nils Huntemann, Richard Lange, Christian Tamm, and Ekkehard Peik.
Autobalanced ramsey spectroscopy.
Phys. Rev. Lett., 120:053602, Jan 2018.
doi: 10.1103/PhysRevLett.120.053602.
- [38] M. Shuker, J. W. Pollock, R. Boudot, V. I. Yudin, A. V. Taichenachev, J. Kitching, and E. A. Donley.
Ramsey spectroscopy with displaced frequency jumps.
Phys. Rev. Lett., 122:113601, Mar 2019.
doi: 10.1103/PhysRevLett.122.113601.
- [39] V.I. Yudin, M. Yu. Basalaev, A.V. Taichenachev, J.W. Pollock, Z.L. Newman, M. Shuker, A. Hansen, M.T. Hummon, R. Boudot, E.A. Donley, and J. Kitching.
General methods for suppressing the light shift in atomic clocks using power modulation.
Phys. Rev. Applied, 14:024001, Aug 2020.
doi: 10.1103/PhysRevApplied.14.024001.
7
- [40] S. L. Campbell, R. B. Hutson, G. E. Marti, A. Goban, N. Darkwah Oppong, R. L. McNally, L. Sonderhouse, J. M. Robinson, W. Zhang, B. J. Bloom, and J. Ye.
A fermi-degenerate three-dimensional optical lattice clock.
Science, 358(6359):90–94, 2017.
doi: 10.1126/science.aam5538.
7
- [41] G. Edward Marti, Ross B. Hutson, Akihisa Goban, Sara L. Campbell, Nicola Poli, and Jun Ye.
Imaging optical frequencies with 100 μHz precision and 1.1 μm resolution.
Phys. Rev. Lett., 120:103201, Mar 2018.
doi: 10.1103/PhysRevLett.120.103201.
7
- [42] JingBiao Chen.
Active optical clock.
Chinese Science Bulletin, 54(3):348–352, Feb 2009.
doi: 10.1007/s11434-009-0073-y.
8
- [43] D. Meiser, Jun Ye, D. R. Carlson, and M. J. Holland.
Prospects for a millihertz-linewidth laser.

- Phys. Rev. Lett.*, 102:163601, Apr 2009.
doi: 10.1103/PhysRevLett.102.163601.
- [44] Matthew A. Norcia, Matthew N. Winchester, Julia R. K. Cline, and James K. Thompson.
Superradiance on the millihertz linewidth strontium clock transition.
Science Advances, 2(10), 2016.
doi: 10.1126/sciadv.1601231.
8
- [45] Matthew A. Norcia, Julia R. K. Cline, Juan A. Muniz, John M. Robinson, Ross B. Hutson, Akihisa Goban, G. Edward Marti, Jun Ye, and James K. Thompson.
Frequency measurements of superradiance from the strontium clock transition.
Phys. Rev. X, 8:021036, May 2018.
doi: 10.1103/PhysRevX.8.021036.
8
- [46] M. A. Norcia, A. W. Young, and A. M. Kaufman.
Microscopic control and detection of ultracold strontium in optical-tweezer arrays.
Phys. Rev. X, 8:041054, Dec 2018.
doi: 10.1103/PhysRevX.8.041054.
8
- [47] Alexandre Cooper, Jacob P. Covey, Ivaylo S. Madjarov, Sergey G. Porsev, Marianna S. Safronova, and Manuel Endres.
Alkaline-earth atoms in optical tweezers.
Phys. Rev. X, 8:041055, Dec 2018.
doi: 10.1103/PhysRevX.8.041055.
- [48] Ivaylo S. Madjarov, Alexandre Cooper, Adam L. Shaw, Jacob P. Covey, Vladimir Schkolnik, Tai Hyun Yoon, Jason R. Williams, and Manuel Endres.
An atomic-array optical clock with single-atom readout.
Phys. Rev. X, 9:041052, Dec 2019.
doi: 10.1103/PhysRevX.9.041052.
- [49] Matthew A. Norcia, Aaron W. Young, William J. Eckner, Eric Oelker, Jun Ye, and Adam M. Kaufman.
Seconds-scale coherence on an optical clock transition in a tweezer array.
Science, 366(6461):93–97, 2019.
doi: 10.1126/science.aay0644.
8

- [50] O. Terra, G. Grosche, K. Predehl, R. Holzwarth, T. Legero, U. Sterr, B. Lipphardt, and H. Schnatz.
Phase-coherent comparison of two optical frequency standards over 146 km using a telecommunication fiber link.
Applied Physics B, 97(3):541, Jul 2009.
doi: 10.1007/s00340-009-3653-2.
8
- [51] O. Terra, G. Grosche, and H. Schnatz.
Brillouin amplification in phase coherent transfer of optical frequencies over 480 km fiber.
Opt. Express, 18(15):16102–16111, Jul 2010.
doi: 10.1364/OE.18.016102.
8
- [52] K. Predehl, G. Grosche, S. M. F. Raupach, S. Droste, O. Terra, J. Alnis, Th. Legero, T. W. Hänsch, Th. Udem, R. Holzwarth, and H. Schnatz.
A 920-kilometer optical fiber link for frequency metrology at the 19th decimal place.
Science, 336(6080):441–444, 2012.
doi: 10.1126/science.1218442.
- [53] S. Droste, F. Ozimek, Th. Udem, K. Predehl, T. W. Hänsch, H. Schnatz, G. Grosche, and R. Holzwarth.
Optical-frequency transfer over a single-span 1840 km fiber link.
Phys. Rev. Lett., 111:110801, Sep 2013.
doi: 10.1103/PhysRevLett.111.110801.
8
- [54] C. Lisdat, G. Grosche, N. Quintin, C. Shi, S. M. F. Raupach, C. Grebing, D. Nicolodi, F. Stefani, A. Al-Masoudi, S. Dörscher, S. Häfner, J.-L. Robyr, N. Chiodo, S. Bilicki, E. Bookjans, A. Koczwara, S. Koke, A. Kuhl, F. Wiotte, F. Meynadier, E. Camisard, M. Abgrall, M. Lours, T. Legero, H. Schnatz, U. Sterr, H. Denker, C. Chardonnet, Y. Le Coq, G. Santarelli, A. Amy-Klein, R. Le Targat, J. Lodewyck, O. Lopez, and P.-E. Pottie.
A clock network for geodesy and fundamental science.
Nature Communications, 7(1):12443, Aug 2016.
doi: 10.1038/ncomms12443.
8, 9
- [55] P. Delva, J. Lodewyck, S. Bilicki, E. Bookjans, G. Vallet, R. Le Targat, P.-E. Pottie, C. Guerlin, F. Meynadier, C. Le Poncin-Lafitte, O. Lopez, A. Amy-Klein, W.-K. Lee, N. Quintin, C. Lisdat, A. Al-Masoudi,

- S. Dörscher, C. Grebing, G. Grosche, A. Kuhl, S. Raupach, U. Sterr, I. R. Hill, R. Hobson, W. Bowden, J. Kronjäger, G. Marra, A. Rolland, F. N. Baynes, H. S. Margolis, and P. Gill.
Test of special relativity using a fiber network of optical clocks.
Phys. Rev. Lett., 118:221102, Jun 2017.
doi: 10.1103/PhysRevLett.118.221102.
8
- [56] Felicitas Arias Fritz Riehle, Patrick Gill and Lennart Robertsson.
The cipm list of recommended frequency standard values: guidelines and procedures.
Metrologia, 55:188, Feb 2018.
doi: 10.1088/1681-7575/aaa302.
8
- [57] R Schwarz R Lange E Benkler B Lipphardt U Sterr E Peik S Dörscher, N Huntemann and C Lisdat.
Optical frequency ratio of a $^{171}\text{Yb}^+$ single-ion clock and a 87Sr lattice clock.
Metrologia, 58:015005, Jan 2021.
doi: 10.1088/1681-7575/abc86f.
9
- [58] Piero Barbieri Benjamin Rauf Filippo Levi Marco Pizzocaro, Filippo Bregolin and Davide Calonico.
Absolute frequency measurement of the $^1s_0 - ^3p_0$ transition of ^{171}Yb with a link to international atomic time.
Metrologia, 57:035007, May 2019.
doi: 10.1088/1681-7575/ab50e8.
9
- [59] S Bilicki E Bookjans R Le Targat J Lodewyck D Nicolodi Y Le Coq M Abgrall J Guéna L De Sarlo R Tyumenev, M Favier and S Bize.
Comparing a mercury optical lattice clock with microwave and optical frequency standards.
New Journal of Physics, 18:113002, Nov 2016.
doi: 10.1088/1367-2630/18/11/113002.
9
- [60] Alvise Vianello Alissa Silva Charles F A Baynham Helen S Margolis Patrick E G Baird Patrick Gill1 Richard Hobson, William Bowden and Ian R Hill.
A strontium optical lattice clock with 1×10^{-17} uncertainty and measurement of its absolute frequency.
Metrologia, 57:065026, Oct 2020.

- doi: 10.1088/1681-7575/abb530.
9
- [61] R. M. Godun, P. B. R. Nisbet-Jones, J. M. Jones, S. A. King, L. A. M. Johnson, H. S. Margolis, K. Szymaniec, S. N. Lea, K. Bongs, and P. Gill. Frequency ratio of two optical clock transitions in $^{171}\text{yb}^+$ and constraints on the time variation of fundamental constants. *Phys. Rev. Lett.*, 113:210801, Nov 2014.
doi: 10.1103/PhysRevLett.113.210801.
9
- [62] G. P. Barwood, G. Huang, H. A. Klein, L. A. M. Johnson, S. A. King, H. S. Margolis, K. Szymaniec, and P. Gill. Agreement between two $^{88}\text{sr}^+$ optical clocks to 4 parts in 10^{17} . *Phys. Rev. A*, 89:050501, May 2014.
doi: 10.1103/PhysRevA.89.050501.
9
- [63] W. F. McGrew, X. Zhang, R. J. Fasano, S. A. Schäffer, K. Beloy, D. Nicolodi, R. C. Brown, N. Hinkley, G. Milani, M. Schioppo, T. H. Yoon, and A. D. Ludlow. Atomic clock performance enabling geodesy below the centimetre level. *Nature*, 564(7734):87–90, Dec 2018.
doi: 10.1038/s41586-018-0738-2.
9
- [64] S. M. Brewer, J.-S. Chen, A. M. Hankin, E. R. Clements, C. W. Chou, D. J. Wineland, D. B. Hume, and D. R. Leibbrandt. $^{27}\text{al}^+$ quantum-logic clock with a systematic uncertainty below 10^{-18} . *Phys. Rev. Lett.*, 123:033201, Jul 2019.
doi: 10.1103/PhysRevLett.123.033201.
9
- [65] T. Kobayashi, D. Akamatsu, Y. Hisai, T. Tanabe, H. Inaba, T. Suzuyama, F. L. Hong, K. Hosaka, and M. Yasuda. Uncertainty evaluation of an ^{171}yb optical lattice clock at nmij. *IEEE Transactions on Ultrasonics, Ferroelectrics, and Frequency Control*, 65(12):2449–2458, 2018.
doi: 10.1109/TUFFC.2018.2870937.
9
- [66] Nils Nemitz, Takuya Ohkubo, Masao Takamoto, Ichiro Ushijima, Manoj Das, Noriaki Ohmae, and Hidetoshi Katori.

- Frequency ratio of yb and sr clocks with 5×10^{-17} uncertainty at 150 seconds averaging time.
Nature Photonics, 10(4):258–261, Apr 2016.
doi: 10.1038/nphoton.2016.20.
9
- [67] Kazuhiro Yamanaka, Noriaki Ohmae, Ichiro Ushijima, Masao Takamoto, and Hidetoshi Katori.
Frequency ratio of ^{199}Hg and ^{87}Sr optical lattice clocks beyond the si limit.
Phys. Rev. Lett., 114:230801, Jun 2015.
doi: 10.1103/PhysRevLett.114.230801.
9
- [68] John E Bernard Pierre Dubé and Marina Gertsvolf.
Absolute frequency measurement of the $^{88}\text{Sr}^+$ clock transition using a gps link to the si second.
Metrologia, 54:290, Mar 2017.
doi: 10.1088/1681-7575/aa5e60.
9
- [69] A. Yamaguchi, M. S. Safronova, K. Gibble, and H. Katori.
Narrow-line cooling and determination of the magic wavelength of cd.
Phys. Rev. Lett., 123:113201, Sep 2019.
doi: 10.1103/PhysRevLett.123.113201.
9
- [70] H. Hachisu, K. Miyagishi, S. G. Porsev, A. Derevianko, V. D. Ovsiannikov, V. G. Pal’chikov, M. Takamoto, and H. Katori.
Trapping of neutral mercury atoms and prospects for optical lattice clocks.
Phys. Rev. Lett., 100:053001, Feb 2008.
doi: 10.1103/PhysRevLett.100.053001.
9
- [71] Jan Friebe, André Pape, Matthias Riedmann, Karsten Moldenhauer, Tanja Mehlstäubler, Nils Rehbein, Christian Lisdat, Ernst M. Rasel, Wolfgang Ertmer, Harald Schnatz, Burghard Lipphardt, and Gesine Grosche.
Absolute frequency measurement of the magnesium intercombination transition $^1s_0 \rightarrow ^3p_1$.
Phys. Rev. A, 78:033830, Sep 2008.
doi: 10.1103/PhysRevA.78.033830.
9, 14
- [72] T Wübbena A Pape H Kelkar W Ertmer O Terra U Sterr S Weyers G Grosche J Friebe, M Riedmann.

- Remote frequency measurement of the $1s0 \rightarrow 3p1$ transition in laser-cooled ^{24}Mg .
New Journal of Physics, 13:125010, Dec 2011.
doi: 10.1088/1367-2630/13/12/125010.
9
- [73] Sergey G. Porsev and Andrei Derevianko.
Multipolar theory of blackbody radiation shift of atomic energy levels and its implications for optical lattice clocks.
Phys. Rev. A, 74:020502, Aug 2006.
doi: 10.1103/PhysRevA.74.020502.
9
- [74] A. P. Kulosa, D. Fim, K. H. Zipfel, S. Rühmann, S. Sauer, N. Jha, K. Gibble, W. Ertmer, E. M. Rasel, M. S. Safronova, U. I. Safronova, and S. G. Porsev.
Towards a mg lattice clock: Observation of the $^1S_0 - ^3P_0$ transition and determination of the magic wavelength.
Phys. Rev. Lett., 115:240801, Dec 2015.
doi: 10.1103/PhysRevLett.115.240801.
9, 25, 28, 79
- [75] Thomas Middelmann, Stephan Falke, Christian Lisdat, and Uwe Sterr.
High accuracy correction of blackbody radiation shift in an optical lattice clock.
Phys. Rev. Lett., 109:263004, Dec 2012.
doi: 10.1103/PhysRevLett.109.263004.
9
- [76] John D. Prestage, Robert L. Tjoelker, and Lute Maleki.
Atomic clocks and variations of the fine structure constant.
Phys. Rev. Lett., 74:3511–3514, May 1995.
doi: 10.1103/PhysRevLett.74.3511.
10
- [77] André Philipp Kulosa.
Lamb-Dicke spectroscopy of the $^1S_0 \rightarrow ^3P_0$ transition in ^{24}Mg and precise determination of the magic wavelength.
PhD thesis, Gottfried Wilhelm Leibniz Universität Hannover, 2015.
10, 48, 50, 52
- [78] Klaus Hendrik Zipfel.
Hochauflösende Spektroskopie und Stabilitätsanalyse eines Magnesium-Frequenzstandards.

- PhD thesis, Gottfried Wilhelm Leibniz Universität Hannover, 2019.
10, 37, 42, 56, 59, 64, 70, 77
- [79] Dominika Fim.
First optical lattice frequency standard based on ^{24}Mg atoms.
PhD thesis, Gottfried Wilhelm Leibniz Universität Hannover, 2021.
10, 25, 59, 79, 80
- [80] Andrew D. Ludlow, Martin M. Boyd, Jun Ye, E. Peik, and P. O. Schmidt.
Optical atomic clocks.
Rev. Mod. Phys., 87:637–701, Jun 2015.
doi: 10.1103/RevModPhys.87.637.
13
- [81] Immanuel Bloch.
Ultracold quantum gases in optical lattices.
Nature Physics, 1(1):23–30, Oct 2005.
doi: 10.1038/nphys138.
15
- [82] R. Taïeb, R. Dum, J. I. Cirac, P. Marte, and P. Zoller.
Cooling and localization of atoms in laser-induced potential wells.
Phys. Rev. A, 49:4876–4887, Jun 1994.
doi: 10.1103/PhysRevA.49.4876.
15
- [83] I. Bouchoule, H. Perrin, A. Kuhn and C. Salomon.
Sideband cooling of neutral atoms in a far-detuned optical lattice.
Europhysics Letters, 42:395, Apr 1998.
doi: 10.1209/epl/i1998-00261-y.
- [84] Vladan Vuletić, Cheng Chin, Andrew J. Kerman, and Steven Chu.
Degenerate raman sideband cooling of trapped cesium atoms at very high
atomic densities.
Phys. Rev. Lett., 81:5768–5771, Dec 1998.
doi: 10.1103/PhysRevLett.81.5768.
15
- [85] Tetsuya Ido and Hidetoshi Katori.
Recoil-free spectroscopy of neutral sr atoms in the lamb-dicke regime.
Phys. Rev. Lett., 91:053001, Jul 2003.
doi: 10.1103/PhysRevLett.91.053001.
25

- [86] Christopher J Foot.
Atomic physics.
Oxford master series in atomic, optical, and laser physics. Oxford University Press, Oxford, 2007.
26
- [87] A. V. Taichenachev, V. I. Yudin, C. W. Oates, C. W. Hoyt, Z. W. Barber, and L. Hollberg.
Magnetic field-induced spectroscopy of forbidden optical transitions with application to lattice-based optical atomic clocks.
Phys. Rev. Lett., 96:083001, Mar 2006.
doi: 10.1103/PhysRevLett.96.083001.
27, 28, 64, 75, 76
- [88] Xavier Baillard, Mathilde Fouché, Rodolphe Le Targat, Philip G. Westergaard, Arnaud Lecallier, Yann Le Coq, Giovanni D. Rovera, Sebastien Bize, and Pierre Lemonde.
Accuracy evaluation of an optical lattice clock with bosonic atoms.
Opt. Lett., 32(13):1812–1814, Jul 2007.
doi: 10.1364/OL.32.001812.
28
- [89] N. Poli, M. G. Tarallo, M. Schioppo, D. Sutyryn, N. Beverini, C. W. Oates, and G. M. Tino.
Optical lattice clock on bosonic strontium atoms.
In *CLEO Europe and QECC 2009 Conference Digest*, pages EE1–3. Optical Society of America, 2009.
- [90] Tomoya Akatsuka, Masao Takamoto, and Hidetoshi Katori.
Optical lattice clocks with non-interacting bosons and fermions.
Nature Physics, 4(12):954–959, Dec 2008.
doi: 10.1038/nphys1108.
- [91] Piotr Morzyński, Marcin Bober, Dobrosława Bartoszek-Bober, Jerzy Nawrocki, Przemysław Krehlik, Łukasz Śliwczyński, Marcin Lipiński, Piotr Masłowski, Agata Cygan, Piotr Dunst, Michał Garus, Daniel Lisak, Jerzy Zachorowski, Wojciech Gawlik, Czesław Radzewicz, Roman Ciuryło, and Michał Zawada.
Absolute measurement of the $1s_0$ - $3p_0$ clock transition in neutral 88Sr over the 330 km-long stabilized fibre optic link.
Scientific Reports, 5(1):17495, Dec 2015.
doi: 10.1038/srep17495.
28

- [92] Michael J. Thorpe, Lars Rippe, Tara M. Fortier, Matthew S. Kirchner, and Till Rosenband.
Frequency stabilization to 6×10^{-16} via spectral-hole burning.
Nature Photonics, 5(11):688–693, Nov 2011.
doi: 10.1038/nphoton.2011.215.
29
- [93] Ying T. Chen.
Use of single-mode optical fiber in the stabilization of laser frequency.
Appl. Opt., 28(11):2017–2021, Jun 1989.
doi: 10.1364/AO.28.002017.
29
- [94] F. Riehle.
Frequency Standards: Basics and Applications.
Wiley, 2003.
30, 70
- [95] Christian Koch.
Vierwellen-mischung in laserdioden.
Technical report, Physikalisch-Technische Bundesanstalt / Abteilung Optik,
1994.
31
- [96] R. W. P. Drever, J. L. Hall, F. V. Kowalski, J. Hough, G. M. Ford, A. J. Munley, and H. Ward.
Laser phase and frequency stabilization using an optical resonator.
Applied Physics B, 31(2):97–105, Jun 1983.
doi: 10.1007/BF00702605.
31
- [97] Andre Pape.
Hochstabiler Lokaloszillator für einen optischen Magnesium-Frequenzstandard.
PhD thesis, Gottfried Wilhelm Leibniz Universität Hannover, 2012.
32, 33
- [98] Sebastian Häfner, Stephan Falke, Christian Grebing, Stefan Vogt, Thomas Legero, Mikko Merimaa, Christian Lisdat, and Uwe Sterr.
 8×10^{-17} fractional laser frequency instability with a long room-temperature cavity.
Opt. Lett., 40(9):2112–2115, May 2015.
doi: 10.1364/OL.40.002112.
33

- [99] Steffen Rühmann.
Frequenzstabilisierung eines hochstabilen Lasersystems bis zum Thermischen-Rausch-Limit und Berechnungen eines Laser-Synergie-Konzeptes.
PhD thesis, Gottfried Wilhelm Leibniz Universität Hannover, 2018.
33, 34
- [100] Tara Fortier and Esther Baumann.
20 years of developments in optical frequency comb technology and applications.
Communications Physics, 2(1):153, Dec 2019.
doi: 10.1038/s42005-019-0249-y.
36
- [101] F. W. Helbing, G. Steinmeyer, and U. Keller.
Carrier-envelope offset phase-locking with attosecond timing jitter.
IEEE Journal of Selected Topics in Quantum Electronics, 9(4):1030–1040, 2003.
doi: 10.1109/JSTQE.2003.819104.
36
- [102] David J. Jones, Scott A. Diddams, Jinendra K. Ranka, Andrew Stentz, Robert S. Windeler, John L. Hall, and Steven T. Cundiff.
Carrier-envelope phase control of femtosecond mode-locked lasers and direct optical frequency synthesis.
Science, 288(5466):635–639, 2000.
doi: 10.1126/science.288.5466.635.
36
- [103] Daniele Nicolodi, Bérengère Argence, Wei Zhang, Rodolphe Le Targat, Giorgio Santarelli, and Yann Le Coq.
Spectral purity transfer between optical wavelengths at the 10-18 level.
Nature Photonics, 8(3):219–223, Mar 2014.
doi: 10.1038/nphoton.2013.361.
36
- [104] Xiaopeng Xie, Romain Bouchand, Daniele Nicolodi, Michele Giunta, Wolfgang Hänsel, Matthias Lezius, Abhay Joshi, Shubhashish Datta, Christophe Alexandre, Michel Lours, Pierre-Alain Tremblin, Giorgio Santarelli, Ronald Holzwarth, and Yann Le Coq.
Photonic microwave signals with zeptosecond-level absolute timing noise.
Nature Photonics, 11(1):44–47, Jan 2017.
doi: 10.1038/nphoton.2016.215.
36

-
- [105] M. Riedmann, H. Kelkar, T. Wübbena, A. Pape, A. Kulosa, K. Zipfel, D. Fim, S. Rühmann, J. Friebe, W. Ertmer, and E. Rasel.
Beating the density limit by continuously loading a dipole trap from millikelvin-hot magnesium atoms.
Phys. Rev. A, 86:043416, Oct 2012.
doi: 10.1103/PhysRevA.86.043416.
37
- [106] Joscha Heinze.
Frequenzstabilisierung basierend auf einem transferresonator, 2015.
40
- [107] Pierre Lemonde and Peter Wolf.
Optical lattice clock with atoms confined in a shallow trap.
Phys. Rev. A, 72:033409, Sep 2005.
doi: 10.1103/PhysRevA.72.033409.
48
- [108] L. F. Livi, G. Cappellini, M. Diem, L. Franchi, C. Clivati, M. Frittelli, F. Levi, D. Calonico, J. Catani, M. Inguscio, and L. Fallani.
Synthetic dimensions and spin-orbit coupling with an optical clock transition.
Phys. Rev. Lett., 117:220401, Nov 2016.
doi: 10.1103/PhysRevLett.117.220401.
48
- [109] Michael L. Wall, Andrew P. Koller, Shuming Li, Xibo Zhang, Nigel R. Cooper, Jun Ye, and Ana Maria Rey.
Synthetic spin-orbit coupling in an optical lattice clock.
Phys. Rev. Lett., 116:035301, Jan 2016.
doi: 10.1103/PhysRevLett.116.035301.
48
- [110] L. Yi, S. Mejri, J. J. McFerran, Y. Le Coq, and S. Bize.
Optical lattice trapping of ^{199}Hg and determination of the magic wavelength for the ultraviolet $^1s_0 \leftrightarrow ^3p_0$ clock transition.
Phys. Rev. Lett., 106:073005, Feb 2011.
doi: 10.1103/PhysRevLett.106.073005.
54
- [111] Masao Takamoto and Hidetoshi Katori.
Spectroscopy of the $^1s_0 - ^3p_0$ clock transition of ^{87}Sr in an optical lattice.
Phys. Rev. Lett., 91:223001, Nov 2003.
doi: 10.1103/PhysRevLett.91.223001.
54

-
- [112] V D Ovsiannikov, S I Marmo, S N Mokhnenko, and V G Palchikov.
Higher-order effects on uncertainties of clocks of mg atoms in an optical lattice.
Journal of Physics: Conference Series, 793:012020, jan 2017.
doi: 10.1088/1742-6596/793/1/012020.
54, 80, 82, 84
- [113] S. Blatt, J. W. Thomsen, G. K. Campbell, A. D. Ludlow, M. D. Swallows, M. J. Martin, M. M. Boyd, and J. Ye.
Rabi spectroscopy and excitation inhomogeneity in a one-dimensional optical lattice clock.
Phys. Rev. A, 80:052703, Nov 2009.
doi: 10.1103/PhysRevA.80.052703.
55, 56
- [114] G. Santarelli, Ph. Laurent, P. Lemonde, A. Clairon, A. G. Mann, S. Chang, A. N. Luiten, and C. Salomon.
Quantum projection noise in an atomic fountain: A high stability cesium frequency standard.
Phys. Rev. Lett., 82:4619–4622, Jun 1999.
doi: 10.1103/PhysRevLett.82.4619.
69
- [115] G. John Dick, John D. Prestage, Charles A. Greenhall, and Lute Maleki.
Local oscillator induced degradation of medium-term stability in passive atomic frequency standards.
In *22nd Annual Precise Time and Time Interval (PTTI) Applications and Planning Meeting*, pages 487–508, May 1990.
70
- [116] Ian D Leroux, Nils Scharnhorst, Stephan Hannig, Johannes Kramer, Lennart Pelzer, Mariia Stepanova, and Piet O Schmidt.
On-line estimation of local oscillator noise and optimisation of servo parameters in atomic clocks.
54(3):307–321, apr 2017.
doi: 10.1088/1681-7575/aa66e9.
72
- [117] B. DeMarco, J. L. Bohn, J. P. Burke, M. Holland, and D. S. Jin.
Measurement of p -wave threshold law using evaporatively cooled fermionic atoms.
Phys. Rev. Lett., 82:4208–4211, May 1999.
doi: 10.1103/PhysRevLett.82.4208.
78

-
- [118] Paul J. Leo, Paul S. Julienne, Fred H. Mies, and Carl J. Williams.
Collisional frequency shifts in ^{133}Cs fountain clocks.
Phys. Rev. Lett., 86:3743–3746, Apr 2001.
doi: 10.1103/PhysRevLett.86.3743.
78
- [119] Martin W. Zwierlein, Zoran Hadzibabic, Subhadeep Gupta, and Wolfgang Ketterle.
Spectroscopic insensitivity to cold collisions in a two-state mixture of fermions.
Phys. Rev. Lett., 91:250404, Dec 2003.
doi: 10.1103/PhysRevLett.91.250404.
78
- [120] Wolfgang Ketterle and Hans-Joachim Miesner.
Coherence properties of bose-einstein condensates and atom lasers.
Phys. Rev. A, 56:3291–3293, Oct 1997.
doi: 10.1103/PhysRevA.56.3291.
78
- [121] Fang-Fei Wu, Yong-Bo Tang, Ting-Yun Shi, and Li-Yan Tang.
Magic-intensity trapping of the mg lattice clock with light shift suppressed below 10^{-19} .
Phys. Rev. A, 101:053414, May 2020.
doi: 10.1103/PhysRevA.101.053414.
80, 82, 93
- [122] A. V. Taichenachev, V. I. Yudin, V. D. Ovsiannikov, V. G. Pal’chikov, and C. W. Oates.
Frequency shifts in an optical lattice clock due to magnetic-dipole and electric-quadrupole transitions.
Phys. Rev. Lett., 101:193601, Nov 2008.
doi: 10.1103/PhysRevLett.101.193601.
80
- [123] V. D. Ovsiannikov, V. G. Pal’chikov, A. V. Taichenachev, V. I. Yudin, and Hidetoshi Katori.
Multipole, nonlinear, and anharmonic uncertainties of clocks of sr atoms in an optical lattice.
Phys. Rev. A, 88:013405, Jul 2013.
doi: 10.1103/PhysRevA.88.013405.
81
- [124] V. D. Ovsiannikov, S. I. Marmo, V. G. Palchikov, and H. Katori.

- Higher-order effects on the precision of clocks of neutral atoms in optical lattices.
Phys. Rev. A, 93:043420, Apr 2016.
doi: 10.1103/PhysRevA.93.043420.
81
- [125] Anders Brusch, Rodolphe Le Targat, Xavier Baillard, Mathilde Fouché, and Pierre Lemonde.
Hyperpolarizability effects in a sr optical lattice clock.
Phys. Rev. Lett., 96:103003, Mar 2006.
doi: 10.1103/PhysRevLett.96.103003.
82
- [126] R. C. Brown, N. B. Phillips, K. Beloy, W. F. McGrew, M. Schioppo, R. J. Fasano, G. Milani, X. Zhang, N. Hinkley, H. Leopardi, T. H. Yoon, D. Nicolodi, T. M. Fortier, and A. D. Ludlow.
Hyperpolarizability and operational magic wavelength in an optical lattice clock.
Phys. Rev. Lett., 119:253001, Dec 2017.
doi: 10.1103/PhysRevLett.119.253001.
- [127] Ichiro Ushijima, Masao Takamoto, and Hidetoshi Katori.
Operational magic intensity for sr optical lattice clocks.
Phys. Rev. Lett., 121:263202, Dec 2018.
doi: 10.1103/PhysRevLett.121.263202.
82, 83, 84
- [128] Matthew A Norcia, Julia R K Cline, John P Bartolotta, Murray J Holland, and James K Thompson.
Narrow-line laser cooling by adiabatic transfer.
New Journal of Physics, 20(2):023021, 2018.
doi: 10.1088/1367-2630/aaa950.
88
- [129] Mark Kasevich and Steven Chu.
Laser cooling below a photon recoil with three-level atoms.
Phys. Rev. Lett., 69:1741–1744, Sep 1992.
doi: 10.1103/PhysRevLett.69.1741.
89
- [130] D. H. Dunlap and V. M. Kenkre.
Dynamic localization of a charged particle moving under the influence of an electric field.
Phys. Rev. B, 34:3625–3633, Sep 1986.

- doi: 10.1103/PhysRevB.34.3625.
90
- [131] K. W. Madison, M. C. Fischer, R. B. Diener, Qian Niu, and M. G. Raizen. Dynamical bloch band suppression in an optical lattice. *Phys. Rev. Lett.*, 81:5093–5096, Dec 1998.
doi: 10.1103/PhysRevLett.81.5093.
90
- [132] Ross B. Hutson, Akihisa Goban, G. Edward Marti, Lindsay Sonderhouse, Christian Sanner, and Jun Ye. Engineering quantum states of matter for atomic clocks in shallow optical lattices. *Phys. Rev. Lett.*, 123:123401, Sep 2019.
doi: 10.1103/PhysRevLett.123.123401.
90
- [133] R. Scheunemann, F. S. Cataliotti, T. W. Hänsch, and M. Weitz. Resolving and addressing atoms in individual sites of a CO_2 -laser optical lattice. *Phys. Rev. A*, 62:051801, Oct 2000.
doi: 10.1103/PhysRevA.62.051801.
90
- [134] Karl D. Nelson, Xiao Li, and David S. Weiss. Imaging single atoms in a three-dimensional array. *Nature Physics*, 3(8):556–560, Aug 2007.
doi: 10.1038/nphys645.
90
- [135] Jérôme Lodewyck, Philip G. Westergaard, and Pierre Lemonde. Nondestructive measurement of the transition probability in a sr optical lattice clock. *Phys. Rev. A*, 79:061401, Jun 2009.
doi: 10.1103/PhysRevA.79.061401.
94
- [136] G Vallet, E Bookjans, U Eismann, S Bilicki, R Le Targat, and J Lodewyck. A noise-immune cavity-assisted non-destructive detection for an optical lattice clock in the quantum regime. *New Journal of Physics*, 19(8):083002, 2017.
doi: 10.1088/1367-2630/aa7c84.
94

-
- [137] Richard Hobson, William Bowden, Alvise Vianello, Ian R. Hill, and Patrick Gill.
Cavity-enhanced non-destructive detection of atoms for an optical lattice clock.
Opt. Express, 27(26):37099–37110, Dec 2019.
doi: 10.1364/OE.27.037099.

LIST OF FIGURES

1.1	Schematic of optical atomic clock	4
1.2	Atomic clock performance history	5
1.3	Ultrastable laser performance history	7
2.1	Magnesium energy level scheme	14
2.2	Excitation probability for particle in a box	16
2.3	Excitation probability while preserving the motional state for a particle in a box	17
2.4	Band structure for a 1D optical lattice	21
2.5	Bloch bandwidth as a function of trap depth	22
2.6	Transition probability between different Bloch bands	23
2.7	Calculated excitation spectrum for atoms trapped in optical lattices of different trap depths	24
2.8	Calculated atomic polarizabilities for 1S_0 and (3P_0) states as a function of wavelength	26
2.9	Ultrastable resonator system used for Magnesium lattice clock	32
2.10	Error signal dependence on step frequency	34
2.11	Influence of noise on error signals with different step frequencies	35
2.12	Schematic of magnesium lattice clock setup	37

3.1	Introduction to spectroscopy of atoms in a shallow lattice	47
3.2	Carrier lineshape calculated for a shallow lattice showing influence of Bloch band	48
3.3	Peak separation of Bloch band doublet lineshape as a function of circulating power in lattice enhancement cavity	49
3.4	Evolution of the spectroscopy lineshape as a function of lattice depth for a magic lattice frequency	50
3.5	Evolution of the spectroscopy lineshape as a function of lattice depth for a lattice wavelength detuning of -0.74 nm from the magic wavelength	51
3.6	Development of lineshape asymmetry as lattice wavelength is detuned from magic condition: Experimental and theoretical results	52
3.7	Influence of nonlinear lattice light shift in calculated Bloch band resolved lineshape for magnesium	53
3.8	Sideband spectrum measurement for magnesium lattice clock	56
3.9	Line broadening due to radial sidebands	56
3.10	Spectroscopy lineshape for different lattice ramp-down depths	57
3.11	Carrier linewidth as a function of lattice ramp-down depth	57
3.12	Lattice lifetime measurement	58
4.1	Lattice enhancement cavity setup used in previous frequency measurement campaign	60
4.2	Measurement of tunneling induced line-broadening	62
4.3	Carrier lineshape measurements showing linewidths in Hz regime	62
4.4	Histogram of linewidth measurements generated from multiple line scan measurements	63
4.5	Measurement of linewidth dependence on probe laser intensity before lattice cavity upgrade	64

4.6	Variation of probe AC Stark shift for different datasets before lattice cavity upgrade	65
4.7	Lattice enhancement cavity setup upgraded to suppress the parasitic probe laser reflections	66
4.8	Measurement of linewidth dependence on probe laser intensity after lattice cavity upgrade	67
4.9	Variation of probe AC Stark shift for different datasets after lattice cavity upgrade	67
4.10	Comparison of probe laser AC Stark shift before and after lattice cavity modifications	68
4.11	Clock instability self-comparison measurement	69
4.12	Numerical simulations showing impact of free running local oscillator noise on the instability of the optical clock	71
5.1	Probe AC Stark shift measurement	75
5.2	Quadratic Zeeman shift measurement	76
5.3	Collision shift measurement	79
5.4	Lattice AC Stark shift measurements	80
5.5	Theoretical lattice AC Stark shift for ^{24}Mg clock transition including the higher order contributions	82
5.6	Nonlinear lattice light shift measurement	83
6.1	SWAP cooling scheme	88
6.2	Tunnel broadening as a function of angle between lattice beams	91
6.3	The effective beam radii for different axes as a function of angle between interfering beams	92
6.4	Tunnel-broadening as a function of lattice depth for different angles between lattice beams	93
6.5	Bow-tie lattice enhancement cavity schematic	93

LIST OF TABLES

1.1	Optical clock performance in labs around the world	9
2.1	Allan deviation for different spectral noise components	31
5.1	Summary of systematic shifts and their uncertainties	85

LIST OF PUBLICATIONS

- *BOOST: A satellite mission to test Lorentz invariance using high-performance optical frequency references*
Norman Gürlebeck, Lisa Wörner, Thilo Schuldt, Klaus Döringshoff, Konstantin Gaul, Domenico Gerardi, Arne Grenzebach, Nandan Jha, Evgeny Kovalchuk, Andreas Resch, Thijs Wendrich, Robert Berger, Sven Herrmann, Ulrich Johann, Markus Krutzik, Achim Peters, Ernst M. Rasel, and Claus Braxmaier
Physical Review D **97**, 124051 (2018)
- *Towards a Mg lattice clock: Observation of the $^1S_0 \rightarrow ^3P_0$ transition and determination of the magic wavelength*
André P. Kulosa, Dominika Fim, Klaus H. Zipfel, Steffen Rühmann, Steffen Sauer, Nandan Jha, Kurt Gibble, Wolfgang Ertmer, Ernst M. Rasel, Marianna S. Safronova, Ulyana I. Safronova, and Sergey G. Porsev
Physical Review Letters, **115**, 240801 (2015)
- *Spectral ensemble ghost imaging*
Nandan Jha
Journal of Physics B, **48**, 135401 (2015)
- *Temporal contrast improvement in chirped pulse amplification systems by a four-grating compressor and by spectral modifications*
Nandan Jha and Paramita Deb
Optik, **125**, 2261 (2014)
- *The steady state of a particle in a vibrating box and possible application in short pulse generation of charged particles*
Nandan Jha and Sudhir R. Jain
Pramana-Journal of Physics, **81**, 485 (2013)

ACKNOWLEDGMENTS

This thesis would not have been possible without the help and support of all the people around me. I would like to express my sincerest gratitude towards them.

First of all, I would like to thank Prof. Ernst Rasel for giving me a chance to do my PhD under his supervision. I will never forget all your help and support during this time. The trust you had shown on me in our first interview will stay with me forever.

I would like to thanks Prof. Wolfgang Ertmer for taking time out of his busy schedule to review my thesis. Our experiment had started under your supervision, and I thank you for laying the foundations for such an excellent research and academic environment in the institute.

I thank Prof. Kurt Gible for also agreeing to review my thesis. I am also thankful to you for all our scientific discussions. I learned a lot from you in a short time. I am also thankful to Prof. Klemens Hammerer for chairing the evaluation committee.

I would like to thank the past and present members of Magnesium team for their help during my time here in Hannover. Dominika's help in all the administrative processes when I first arrived in Hannover made things a lot easier for me. The fun discussions I had with André Kulosa were a great learning experience for me. I am thankful to Steffen Rühmann, Klaus Zipfel, Steffen Sauer, Waldemar Friesen-Piepenbrink and Nishad Wesavkar for all the fun memories over these years. In particular, I am thankful to you Waldemar for all your help in the lab, those lunch and coffee (cinnamon coffee before Christmas) discussions and especially for your friendship. I could always count on you. I want to thank all the students who worked on our experiment and made the atmosphere even more lively. In particular, thank you Philipp Gehrke for taking care of Waffle Wednesdays.

I am thankful to all the colleagues in the institute for a nice working atmosphere. I

want to thank Dr. Kai-Martin Knaak for his support in various electronics projects. Likewise, I am also thankful for all the support from our mechanical workshop. The secretaries in the institute, Frau Göldner-Pauer, Frau Faber, Frau Hünitzsch, Frau Pfennig, Frau Kaisik, Frau Rückert, Frau Thiele-Bode have all helped me at one time or the another. I thank you all for that.

I also want to thank all the collaborators outside Hannover. In particular, I thank Dr. Uwe Sterr, Dr. Thomas Legero and Dr. Sebastian Häfner from PTB for their help during my work on crystalline coating mirrors there.

Saving the best for last, I am thankful to my family for all their support over the long years. I can't thank my parents Kumar Kant Jha and Anita Devi enough, for making all the sacrifices that they made to provide for my education. I am thankful to my brother Jai Prakash for always showing me the path to follow in academics. My wife Neetika has been a pillar of strength for me. Thank you for always being there, for supporting me and my career, even though it sometimes made things difficult for you.

CURRICULUM VITAE

Personal Details

Name	Nandan Jha
Date and Place of Birth	25.03.1987, New Delhi, India
Marital Status	Married
Nationality	Indian

Studies

2004	Central Board of Secondary Education Secondary School
2004 - 2007	University of Delhi Bachelor of Science (Hons.) Physics
2008 - 2010	Indian Institute of Technology Delhi Master of Science, Physics
2010 - 2011	Bhabha Atomic Research Center, Mumbai One Year Orientation Course in Nuclear Science & Engineering
2014 - Today	Leibniz Universität Hannover PhD in Physics

Work Experience

2011 - 2014	Scientific Officer C, Bhabha Atomic Research Center, Mumbai
2014 - Today	Research Assistant, Institute of Quantum Optics, Leibniz Universität Hannover